Electron confinement and quantum-well states in two-dimensional magnetic systems

Volker Renken

2007

Experimentelle Physik

Electron confinement and quantum-well states in two-dimensional magnetic systems

Inaugural-Dissertation
zur Erlangung des Doktorgrades
der Naturwissenschaften im Fachbereich Physik
der Mathematisch-Naturwissenschaftlichen Fakultät
der Westfälischen Wilhelms-Universität Münster

vorgelegt von
Volker Renken
aus Salzkotten

- 2007 -

Dekan:	Prof. Dr. J. P. Wessels
Erster Gutachter:	Prof. Dr. M. Donath
Zweiter Gutachter:	Prof. Dr. H. Kohl
Tag der mündlichen Prüfung:	20.06.2007
Tag der Promotion:	20.06.2007

To My Family

Abstract

In the present study, electron confinement in two-dimensional magnetic systems is investigated by measuring discrete unoccupied quantum-well states. By means of spin- and angle-resolved inverse photoemission, the electronic structure above the Fermi level is probed. As samples, Ni films on Cu(001) and Cu films on Ni / Cu(001) as well as on Co / Cu(001) are chosen.

Concerning Ni / Cu(001), the different spectral features are introduced and the spectra are compared with the corresponding ones of Co / Cu(001). The spin asymmetry of transitions into the Ni d bands is discussed. As expected from the Ni and Cu bulk band structures, discrete spin-polarized quantum-well states in the Ni film show up owing to electron confinement. The spin character of the quantum-well states is investigated. Furthermore, the dependence of the spectral features on the Ni film thickness and the transition from discrete two-dimensional quantum-well states to the continuous three-dimensional bulk band structure is analyzed. The spectral features are further investigated as a function of the electron wave vector parallel to the surface along the [110] direction showing a transition from quantum-well states to crystal-induced surface resonances.

For thin Cu films on Ni / Cu(001) as well as on Co / Cu(001), the dependence of the spectral features on the Cu film thickness and the formation of the bulk band structure are introduced. Moreover, for Cu on Ni / Cu(001) the energy dispersion along the [110] direction is discussed. For Cu on Co / Cu(001), the crystal-induced surface states are analyzed.

Kurzfassung

In der vorliegenden Arbeit wird der Einschluss von Elektronen in zweidimensionalen magnetischen Systemen durch die Messung diskreter unbesetzter Quantentrogzustände untersucht. Mittels spin- und winkelaufgelöster Inverser Photoemission wird die elektronische Struktur oberhalb der Fermi-Energie bestimmt. Als Proben werden Ni-Filme auf Cu(001) und Cu-Filme sowohl auf Ni / Cu(001) als auch auf Co / Cu(001) verwendet.

Bezüglich Ni / Cu(001) werden die verschiedenen Strukturen in den Spektren vorgestellt, und die Spektren werden mit entsprechenden Spektren von Co / Cu(001) verglichen. Die Spin-Asymmetrie von Übergängen in die d-Bänder von Ni wird diskutiert. Aufgrund von Elektroneneinschluss treten diskrete spinpolarisierte Quantentrogzustände in den Ni-Filmen auf, wie dies aufgrund der Volumenbandstrukturen von Ni und Cu zu erwarten ist. Der Spin-Charakter der Quantentrogzustände wird untersucht. Des Weiteren wird die Abhängigkeit der spektralen Strukturen von der Dicke der Ni-Filme sowie der Übergang von diskreten zweidimensionalen Quantentrogzuständen zur kontinuierlichen dreidimensionalen Volumenbandstruktur analysiert. Die spektralen Strukturen werden überdies als Funktion des Elektronenwellenvektors parallel zur Oberfläche entlang der [110]-Richtung untersucht, wo ein Übergang von Quantentrogzuständen zu kristallinduzierten Oberflächenresonanzen auftritt.

Für dünne Cu-Filme sowohl auf Ni / Cu(001) als auch auf Co / Cu(001) wird die Abhängigkeit der spektralen Strukturen von der Dicke des Cu-Films sowie die Bildung der Volumenbandstruktur vorgestellt. Für Cu auf Ni / Cu(001) wird weiterhin die Energiedispersion entlang der [110]-Richtung diskutiert. Für Cu auf Co / Cu(001) werden die kristallinduzierten Oberflächenzustände analysiert.

Contents

1 Introduction **1**

1.1 Motivation 1

1.2 Actual standard of knowledge 2

1.3 Outline 6

2 Electronic structure and quantum-well states **7**

2.1 Electronic bulk and surface states 7

2.2 Quantum-well states in metallic thin films 10

2.2.1 Thin Co and Ni films on Cu(001) 11

2.2.2 The phase-accumulation model 13

2.2.3 Transition from discrete states to bulk bands 17

3 Ni and Co films on Cu(001) **21**

3.1 General aspects of film growth and magnetism 21

3.2 Ni on Cu(001) 26

3.3 Co on Cu(001) 28

3.4 Bilayers 29

3.5 Electronic structure 30

3.5.1 Modifications in thin films 30

3.5.2 Previous measurements of quantum-well states 32

4 Experiment **35**

4.1 Spin-resolved inverse photoemission 35

4.1.1 Theoretical aspects 36

4.1.2 Experimental aspects 39

4.2 Sample preparation and characterization 43

4.2.1 The Cu(001) substrate 43

4.2.2 Preparation of Ni, Co, and Cu films 44

4.3 Experimental set-up 45

5 Ni on Cu(001) **49**

5.1 Electronic states of Ni films on Cu(001) 49

5.1.1 Ni on Cu(001) compared to Co on Cu(001) 49

5.1.2 Exchange splitting of the quantum-well states 52
5.1.3 Summary 54
5.2 Spin-dependence of the Ni-d bulk feature 56
5.2.1 Influence of the Cu(001) substrate 56
5.2.2 Influence of the reduced magnetization 57
5.2.3 Influence of the magnetization direction 60
5.2.4 Summary 62
5.3 Ni on Cu(001): Thickness dependence 64
5.4 Ni on Cu(001): Angular dependence 70

6 Cu on Ni(001) and on Co(001) 75
6.1 Electronic states of Cu films on Ni(001) 75
6.1.1 Cu on Ni / Cu(001): Thickness dependence 75
6.1.2 Cu on Ni / Cu(001): Angular dependence 81
6.2 Electronic states of Cu films on Co(001) 84
6.2.1 Cu on Co / Cu(001): Quantum-well states 84
6.2.2 Cu on Co / Cu(001): Surface states 86

7 Summary / Zusammenfassung 97

Bibliography 105

Danksagung 121

List of Figures

2.1 Quantum-well states in a thin film. 10
2.2 Band structure of $Co_{\downarrow,\uparrow}$ and Cu. 12
2.3 Band structure of $Ni_{\downarrow,\uparrow}$ and Cu. 13
2.4 Schematic potential diagram illustrating the phase accumulation model. 14
2.5 Phase accumulation model for $Co_{\uparrow}$. 16
2.6 Schematic band and discrete states. 18
2.7 Ni *sp* band and discrete states. 19

3.1 Spin-reorientation transition for Ni / Cu(001). 28

4.1 Principle of inverse photoemission. 35
4.2 Schematic energy diagram for inverse photoemission. 37
4.3 Experimental set-up for inverse photoemission. 40
4.4 AES calibration of the Ni evaporator. 45
4.5 AES calibration of the Cu evaporator. 45
4.6 LEED pictures of Ni / Cu(001). 46

5.1 IPE spectra of Cu and of 6 ML, 10 ML, and 100 ML Ni on Cu. 50
5.2 IPE spectra of Cu and of 5 ML, 10 ML, and 15 ML Co on Cu. 53
5.3 IPE spectra of 6 ML Ni on Cu with improved experimental resolution. 54
5.4 Simulated IPE spectra for 6 ML Ni on Cu(001). 57
5.5 Sketch of the magnetization as a function of the temperature for 6 ML Ni on Cu(001). 58
5.6 IPE spectra of Ni-*d* for 6 ML Ni on Cu(001) at room temperature. . . 59
5.7 IPE spectra of Ni-*d* for 6 ML Ni on Cu(001) at $T = 100\,\mathrm{K}$. 60
5.8 IPE spectra of Ni-*d* for 6 ML Ni on Cu(001) at $\theta = 0°$ and $\theta = 45°$. . 61
5.9 IPE spectra of Ni-*d* for 10 ML Ni on Cu(001) at $\theta = 0°$ and $\theta = 50°$. . 62
5.10 IPE spectra of Ni-*d* for 6 ML Ni on Cu(001) and for 6 ML Ni on 12 ML Co / Cu(001). 63
5.11 IPE spectra of Ni-*d* for 10 ML Ni on Cu(001) and for 10 ML Ni on 12 ML Co / Cu(001). 64
5.12 IPE spectra of *n* ML Ni on Cu: Thickness dependence I. 65
5.13 Asymmetry of *n* ML Ni on Cu(001). 67

5.14 PAM calculation of the QWS for Ni films on Cu(001) in comparison with the experiment. 68
5.15 IPE spectra of n ML Ni on Cu: Thickness dependence II. 69
5.16 IPE spectra of 6 ML Ni on Cu as a function of the electron incidence angle. 71
5.17 Energy dispersion of 6 ML Ni on Cu along the [110] direction. 73

6.1 IPE spectra of n ML Cu / 6 ML Ni / Cu(001) at $\theta = 0°$ at 100 K. 76
6.2 IPE spectra of n ML Cu / 6 ML Ni / Cu(001) at $\theta = 0°$. 77
6.3 IPE spectra of n ML Cu / 6 ML Ni / Cu(001) at $\theta = 25°$. 81
6.4 IPE spectra of 2 ML Cu / 6 ML Ni / Cu(001) as a function of the electron incidence angle. 83
6.5 Energy dispersion of 2 ML Cu / 6 ML Ni / Cu(001) along the [110] direction. 84
6.6 IPE spectra of n ML Cu / 5 ML Co / Cu(001) at $\theta = 25°$. 85
6.7 IPE spectra of the Cu, Ni, Fe, and Co surface state. 88
6.8 Calculated spin-resolved (I)PE spectral densities of Co(001) along [110]. 89
6.9 STM picture of 5 ML Co / Cu(001). 89
6.10 IPE spectra of 5 ML Co / Cu(001) at $\theta = 50°$. 90
6.11 Geometrical arrangement of the IPE set-up and dipole radiation. . . . 91
6.12 IPE spectra of 5 ML Co / Cu(001) at $\theta = -45°$. 91
6.13 IPE spectra of 0.5 ML Cu / 5 ML Co / Cu(001) at $\theta = 45°$. 92
6.14 IPE spectra of n ML Cu / 5 ML Co / Cu(001) at $\theta = 40°$. 93
6.15 IPE spectra of n ML Cu / 5 ML Co / Cu(001) at $\theta = 45°$. 95

Chapter 1

Introduction

Controlling materials on the atomic scale makes the production and tailoring of artificial structures with novel material properties possible. Reducing the dimensionality gives rise to novel physical phenomena. In thin films, the influence of the film surface becomes important. Furthermore, also the interface between the film and the substrate influences the properties of the film. The same is true for multilayers and the interfaces between two single films. The reduced dimensionality may lead to a confinement of electrons due to the potential barriers at the interfaces. This results in discrete quantized electronic states, so-called quantum-well states. When magnetic materials are involved, these quantum-well states are spin-polarized. Quantum-well states are experimentally accessible, among other things, with photoemission techniques, whereas spin resolution is necessary to deduce their spin dependence. In the present work, the unoccupied electronic structure of magnetic films and bilayers, consisting of Ni, Co, and Cu, on a Cu(001) substrate is investigated by spin- and angle-resolved inverse photoemission, especially with regard to quantum-well states.

1.1 Motivation

The quantum confinement of electrons in ultrathin films leads to standing electron waves, which are denoted as quantum-well states. Consequently, the corresponding electronic structure consists of discrete energy levels, which are reflected in an oscillating density of states as a function of the film thickness. This is responsible for a variety of quantum-size effects, not only in thin films (Jalochowski 1995). In ultrathin magnetic films and, in particular, in sandwich structures with magnetic materials involved, quantum-well states are important for understanding and engineering magnetic materials at the atomic level and for their applications in electronic and spintronic devices (Himpsel et al. 1998, Chiang 2000, Milun et al. 2002, Qiu and Smith 2002, Shen and Kirschner 2002). For example, magnetic multilayers with non-magnetic spacer layers exhibit oscillatory exchange coupling (Parkin et al. 1990) and giant magnetoresistance (GMR) (Baibich et al. 1988, Binash et al. 1989). These discoveries lead to numerous applications, for example reading heads for hard disk devices (Gurney et al. 2005), direction-sensitive sensors (Clemens 1997), and non-volatile magnetic random access memories (MRAM) (Shi 2005). In these applications, Ni is primarily used in form of permalloy ($Ni_{0.8}Fe_{0.2}$). Moreover, it is an

additional ultrathin Co film that significantly enhances the giant-magnetoresistance effect in a structure with permalloy (Parkin 1993, Hwang and Himpsel 1995).

Furthermore, electron quantization could modify the total energy of a thin film, thus leading to electronic growth and film stabilization (Zhang et al. 1998, Luh et al. 2001, Su et al. 2001, Jiang et al. 2004). Many other physical properties, such as the work function (Paggel et al. 2002), the gas desorption energy (Danese et al. 2004*b*), the electron-phonon interaction (Paggel et al. 2004), and the superconducting transition temperature (Guo et al. 2004), show atomic-layer-by-atomic-layer variations (Chiang 2005) and could be modulated by quantum-well states to exhibit oscillatory behavior. Quantum-well engineering has also been performed on semiconductor heterostructures to control the electron spins for next generation spintronics technology (Salis et al. 2001, Yato et al. 2004).

Quantum-well states are believed to act as mediators for the oscillatory exchange coupling. They are spin-polarized, even in noble metals, due to the spin-dependent band structure of the confining ferromagnet. The quantum-well states result from the reflection of the confined electrons at the interfaces of a film owing to the potential differences. For ferromagnetic materials, the averaged inner potential of majority and minority states differs by the magnetic exchange splitting. Hence, the reflectivity at the interfaces is spin-dependent leading to likewise spin-dependent quantum-well states. How large is the spin splitting of the quantum-well states? What is about their energies when changing the parallel electron momentum? How are the energies of these quantum-well states affected when varying the film thickness or when changing the interfaces due to different ad-layers? What is about quantum-well states in a bilayer structure with three interfaces?

By means of thin films it is possible to create novel and artificial crystal structures of a material by constraining the films to the lattice of a single-crystal substrate. For example, the face-centerd tetragonal (fct) structure of thin Ni films on Cu(001) causes the unusual spin-reorientation transition from in-plane to out-of-plane magnetization with increasing film thickness (see section 3.2). In what way differs the electronic structure of thin fct Ni films from the one of bulk Ni, which has a face-centered cubic (fcc) crystal structure? What is about magnetism and the spin asymmetry in thin fct Ni films?

Only some of the above questions have been answered in the last two decades. The development in the research area of magnetic thin films is outlined in the next section, with the focal point on quantum-well states, which are connected with the above mentioned phenomena like magnetic interlayer coupling and giant magnetoresistance, and on results obtained by photoemission techniques.

1.2 Actual standard of knowledge

In 1986, the antiferromagnetic coupling between two magnetic layers across a non-magnetic intervening layer was first observed in a Fe/Cr sandwich structure (Grünberg et al. 1986). The magnetization in the two outer Fe layers points in opposite directions due to the interlayer coupling across the Cr layer. In 1988 the giant magnetoresistance was discovered in an antiferromagnetically coupled Fe/Cr superlattice (Baibich et al. 1988). By aligning the magnetization of all Fe layers with an

external magnetic field, the electric resistance drops by an order of magnitude. By secondary electron microscopy with polarization analysis (SEMPA), the magnetic coupling in the Fe/Cr superlattice was later found to oscillate between antiferromagnetic and ferromagnetic coupling as a function of the thickness of the intervening layer (Unguris et al. 1991). Many other systems were found to show a similar behavior, for instance Fe/Cu (Bennett et al. 1990), Fe/Mo (Brubaker et al. 1991), Co/Cr, Co/Ru (Parkin et al. 1990) and Co/Cu (Pescia et al. 1990, Parkin et al. 1991). The oscillation period for all systems is in the order of 10 Å.

Two models have been proposed to explain the oscillatory behavior of the magnetic interlayer coupling. First, the Rudermann-Kittel-Kasuya-Yosida (RKKY) approach represents an indirect exchange interaction mediated across the non-magnetic intervening layer by itinerant electrons which are spin-dependently scattered at the interfaces (Wang et al. 1990). The RKKY theory not only explains the long-period oscillations in the order of 10 Å, but also predicts the existence of short-period oscillations in the order of $1-3$ monolayers at different saddle points of the Fermi surface. These short-period oscillations were observed only when the quality of the films could be improved, for instance in Fe/Cr(Unguris et al. 1991, Purcell et al. 1991), Fe/Mn (Purcell et al. 1992), Fe/Au (Fuss et al. 1992), Fe/Mo (Qiu et al. 1992*a*), Fe/Ag (Unguris et al. n.d.), and Co/Cu (Johnson et al. 1992, Segovia et al. 1996).

Second, the quantum-well state approach is used to explain the magnetic interlayer coupling (van Schilfgaarde and Harrison 1993, Jones and Hanna 1993, Bruno 1993*a*). At this, the magnetic information is transferred through the non-magnetic intervening layer via the spin polarization of the quantum-well states. The oscillatory exchange coupling arises because the energy that it takes to fill the electron states up to the Fermi level oscillates as a function of the well width (Stiles 1993). For both spin systems, the period of this oscillation is the same, because it is determined by the Fermi surface of the intervening layer material. But in magnetic structures, each spin system experiences a different potential. Since the potential barriers at the interfaces depend on the magnetization direction in the ferromagnetic layers, the reflection probability and hence the amplitude of the oscillatory energy depends on the magnetic configuration of the ferromagnetic layers, which is a parallel or an antiparallel alignment of the magnetization directions. The difference in these oscillatory energies is the oscillatory exchange coupling. The quantum-well model gives the same oscillation periodicity than the RKKY theory (Bruno 1993*b*, Bruno 1995)

Next, searching for the origin of the interlayer coupling gave rise to investigate the dependence of the interlayer coupling on the thickness of the ferromagnetic layers. It is true that a first experiment on Co/Cu/Co showed that the maxima positions of the antiferromagnetic coupling do not depend on the thickness of the Co layers (Qiu et al. 1992*b*), but more detailed work on Co/Ni/Co/Cu/Co/Ni/Co (de Vries et al. 1996), Fe/Cr (Okuno and Inomata 1994), and Fe/Au (Okuno 1995) revealed that the coupling strength actually depends on the magnetic layer thickness. Furthermore, the coupling oscillates depending on the thickness of a Cu cap layer on Co/Cu/Co (de Vries et al. 1995). Hence, the magnetic coupling does not only depend on the interfaces. Every single layer in a multilayer stack is relevant to the magnetic coupling. These results strongly indicate the quantum-well nature of the magnetic interlayer coupling (Stiles 1993, Bruno 1995, Bruno 1999).

In principle, any experiment involving either an electron beam incident on a film or electron emission from a film is adequate to reveal quantum size effects in thin films, including photoemission and inverse photoemission (see below), reflection high energy reflection (Jalocholwski and Bauer 1988), low energy electron microscopy (M.Tromp et al. 1993), scanning tunneling microscopy (Kubby and Greene 1992, Hormandinger and Pendry 1993), and low energy electron reflection (Egger et al. 1999).

In metallic thin films, quantum-well states were first observed in Ag/Au(111) by photoemission (Miller et al. 1988). In magnetic multilayers, the first evidence of quantum-well states succeeded in Cu/Co/Cu(001) (Ortega and Himpsel 1992). The density of states at the Fermi level in the Cu film oscillates with the same long periodicity as the long-period oscillations in the interlayer coupling. Especially the quantum-well states in the non-magnetic Cu layer are spin-polarized due to the spin-dependent energy gap in the ferromagnetic Co (Carbone et al. 1993, Garrison et al. 1993). Thus, the dependence of the interlayer coupling on the thickness of the ferromagnetic layer is due to a quantum interference effect (Kawakami et al. 1998).

An extra set of quantum-well states has been identified in Cu/Co(001) at the neck of the *dog bone*-like Cu Fermi surface in addition to the quantum-well states at the belly of the Fermi surface (Segovia et al. 1996). Short-period oscillations in the density of states at the neck of the Fermi level were observed (Kläsges et al. 1998). By spin-integrated inverse photoemission, the dispersion of the quantum-well energy with the in-plane momentum was determined (Curti et al. 1998, Danese et al. 2001). However, in this work the differentiation between bulk states and quantum-well states is not made (see below). Quantum-well states in Cu films also show up in Cu on fcc Fe/Cu(001) above the Fermi level (Danese et al. 2001, Danese et al. 2004*b*) and in Cu on Ni below the Fermi level (Danese et al. 2001).

The k-space origin of the long-period oscillation in the interlayer magnetic coupling of Fe/Cr(001) multilayers, investigated by means of angle-resolved photoemission by probing quantum-well states at the Fermi level for epitaxial Cr grown on an Fe(001) substrate, results in a periodicity of the intensity oscillations in the vicinity of the d-derived *lens* feature of the Fermi surface, which amounts to 17 Å (Li et al. 1997).

To transmit magnetic effects, quantum-well states need to be spin-polarized, even in a noble metal film. In thin Cu films on Co(001), the quantum-well states in the non-magnetic Cu film were found to be spin-polarized with minority spin character by spin-resolved photoemission (Garrison et al. 1993). This was also concluded by a first-principles local density calculation (Nordström et al. 1995). Furthermore, magnetic circular dichroism (MCD) confirmed the spin polarization of electronic states in Cu films (Samant et al. 1994, Pizzini et al. 1995). Most of the Cu magnetization is located near the interface (Samant et al. 1994), where the hybridization with the magnetic Co states is strongest (Wu et al. 1996). Hence, the magnetic weakest link in the middle of the intervening layer is expected to determine the strength of the magnetic interlayer coupling. Further spin-resolved photoemission investigations (Carbone et al. 1993, Ortega et al. 1999) confirmed the minority spin character of the quantum-well states in the non-magnetic Cu film.

Apart from single films, investigations also started on more complex bilayers and multilayer structures. For Cu on Co/Cu(001), spin-polarized quantum-well states

above the Fermi level in both the Cu film on top and the underlying Co film were found (Yu and Donath 2003*a*). The quantum-well states in the Cu film, with both majority as well as minority spin components, develop into a surface resonance as a function of the electron momentum. In comparison with Curti et al. (1998) and Danese et al. (2001), the spin-polarization enables an unambiguous differentiation between quantum-well states in contrast to bulk-like and surface-derived states.

For Co films on Cu(001), the electronic structure below the Fermi level, investigated by spin-resolved photoemission, does not show any evidence of quantum-well states (Schneider et al. 1991, Clemens et al. 1992). However, with spin-integrated inverse photoemission, unoccupied quantum-well states above the Fermi level were detected (Ortega et al. 1993), and the dispersion of the bulk-like $3d$ states right above the Fermi level was determined (Mankey et al. 1993). Moreover, an *ab initio* calculation found spin-dependent quantum-well states and resonances with minority as well as majority spin character (van Gelderen et al. 1996). These were proved with spin-resolved inverse photoemission depending on the film thickness (Yu et al. 2003*b*). With increasing Co film thickness, the two-dimensional quantum-well states pass into the three-dimensional *sp* band.

For Ag on Fe(001), spin-polarized quantum-well states below the Fermi level were also found with minority spin character (Smith et al. 1994). For the unoccupied quantum-well states above the Fermi level, the overlap with bulk contributions hindered unambiguous conclusions (Rossi et al. 1996). Besides the above mentioned investigations, there is no more information on the spin character of unoccupied quantum-well states so far.

For Ni films on Cu(001), spin-integrated photoemission studies investigated the dependence of the electronic structure on the Ni film thickness below the Fermi level, but only contributions from the d bands are discussed (Pampuch et al. 2001). Spin-integrated inverse photoemission dealt with Ni films on Cu(001) and Ni/Cu/Ni (Himpsel and Rader 1995, Hwang and Himpsel 1995) and Cu/Ni/Cu (Danese et al. 2004*a*) trilayer structures. It is reported about an *anomalous* thickness dispersion of the unoccupied quantum-well states in Cu films on Ni (Danese et al. 2004*a*). For Ni films on Cu(001), discrete QW states were identified, but no spin resolution was used and no dispersion was measured (Himpsel and Rader 1995). Moreover, spin-integrated photoemission studies on Ni/Cu multilayers observed a resonant interaction between two Cu quantum-well states in this double quantum-well structure (Wu et al. 2006). But there is no data available about the spin character of quantum-well states in thin Ni films.

However, it is the spin-polarization of the electronic states that governs the magnetic properties of the thin-film structures and thus determines the magnetic response of possible devices. The spin polarization of the confined electron states with their oscillating density of states at the Fermi level influences the spin transport and the magnetic scattering in nano-meter devices. In the present study, the spin-resolution of the used inverse photoemission experiment is used to further differentiate between unoccupied quantum-well, bulk-like, and surface-derived features, which appear in the inverse photoemission spectra.

1.3 Outline

The structure of the present study is as follows. In the next chapter, the electronic states, which appear in the inverse photoemission spectra presented in this study, are introduced: Electronic bulk-derived states, surface-derived states, and above all quantum-well states. After shortly outlining general aspects on film growth and magnetism, the properties of the investigated magnetic thin films are described in chapter 3, namely growth, structure, and magnetism of ultrathin Ni and Co films on a Cu(001) substrate, as well as of Cu films on top of the magnetic films. The used experimental methods are illustrated in chapter 4, on the one hand the spin-resolved inverse photoemission experiment, on the other hand the techniques for the preparation and characterization of the thin films. Furthermore, the experimental set-up is described. After this, the main results of the present study are presented: Chapter 5 focuses on thin Ni films on Cu(001). To begin with, the different electronic states that appear in this system are introduced and compared to the Co/Cu(001) system. The spin splitting of the quantum-well states is determined. Moreover, the reduced spin asymmetry of transitions into the Ni d bands is discussed. Finally, it is reported about the behavior of the spectral features depending on the film thickness and on the electron momentum. Chapter 6 deals with Cu films on Ni as well as on Co. For both Cu/Ni/Cu(001) and Cu/Co/Cu(001), the dependence on the Cu overlayer thickness and on the electron momentum is investigated. Furthermore, the surface states are discussed. In the end, the main results are summarized in a conclusion.

Chapter 2

Electronic structure and quantum-well states

In this chapter, electronic states, which appear in the inverse photoemission spectra presented in this work, are introduced. The first section deals with electronic bulk as well as surface states, which may show up for bulk samples as well as for thin films. The second section is about quantum-well states, which are the focal point of the present work. Quantum-well states may appear in thin films and layered structures due to the limitation of a film by its interfaces.

2.1 Electronic bulk and surface states

It is true that, on the one hand, due to the use of low-energy electrons the information depth in IPE is a few atomic layers only (see section 4.1.1), but on the other hand the electronic structure in metals in this range already shows bulk-like character. The surface only influences the electronic structure of the outermost atomic layers. As a consequence, IPE spectra contain mixed information about bulk as well as about surface-related electronic structure.

In a solid, the energy levels of the electrons can be described by band theory (Ashcroft and Mermin 1976). Concerning a free electron, the electron energy E as a function of the electron wave vector $\boldsymbol{k}$, the dispersion, is a simple parabolic function. Because of the periodic crystal potential, this function is multivalued for a bulk crystal. There are certain three-dimensional bands of energy, separated by regions of energy which are forbidden. These are the energy band gaps. Bulk electron wave functions have a periodically varying amplitude throughout the crystal. These states are reflected by the vacuum barrier in the surface region.

In metals, the electronic band structure of the valance bands strongly resembles that one of the simple model of a free electron gas. The bulk bands derived from atomic s and p bands have a nearly parabolic shape. In transition and noble metals, d orbitals of the single atom interact in the crystal to give d bands, which are typically $4-10\,\mathrm{eV}$ wide. Due to their localized nature, the d bands show less dispersion than s, p bands. For ferromagnets, the bands are split into two subsets: one with majority spin, one with minority spin. Most of the spin-polarization in ferromagnets stems from the d bands. Typically, the ferromagnetic exchange splitting (see section 4.1.1)

of d bands is more than twice that of the s, p bands. The bulk band structure for Ni, Co, and Cu is discussed in section 2.2.1.

Radiative transitions between bulk bands are accessible to photoemission techniques (see section 4.1). With angular resolution, the band dispersion can be measured, thus mapping the bulk band structure.

At surfaces, the dimensionality is reduced. The symmetry in the direction perpendicular to the surface is broken, and for a surface atom, there are fewer neighbor atoms. Compared to bulk properties, the electronic structure near the surface is noticeable different (Kevan and Eberhardt 1992). The wave functions of true surface states are confined to the surface region. They exponentially decay into the solid as well as into the vacuum. Therefore, surface states are two-dimensional states, with energies depending on the parallel component of the electron wave vector or reciprocal lattice vector $\boldsymbol{k}_{\parallel}$, but not on the perpendicular one ($\boldsymbol{k}_{\perp}$). The energy levels of true surface states are not degenerated with bulk bands. Thus, they appear inside a gap that is formed when the bulk bands are projected onto the two-dimensional surface Brillouin zone and that shows the same symmetry and spin character.

Surface resonances do not appear inside these gaps of the projected bulk band structure. They have an enhanced amplitude of their wave function at the surface, but they are less confined to the surface region than true surface states. Surface resonances can penetrate into a part of the surface Brillouin zone where propagating bulk states exist. Hence, they can mix with bulk states of same symmetry and spin. Thus, they propagate deep into the bulk, but will nevertheless retain a large amplitude close to the surface. As in the bulk, there exist s, p-like surface states as well as d-like surface states.

Concerning the mathematical approach, one distinguishes between two kinds of surface states. Both strongly depend on the bulk electronic structure and are thus called crystal-induced surface states. In the framework of the nearly-free-electron model, Shockley states (Shockley 1939) are located in energy band gaps caused by the hybridization of crossed bands. In the tight-binding approach, Tamm states (Tamm 1932) are split from fairly localized states, well approximated by surface core levels and surface states split off narrow d bands. In a real material, the situation is neither that of the free electron nor that of the tight binding extremes. Hence, the actual surface states found are neither simple Tamm states nor simple Shockley states, but a mixture of both Tamm and Shockley states.

Another kind of surface states are image-potential-induced surface states (Echenique and Pendry 1978). These states derive from from the symmetry-breaking effect of the surface. Approaching a conductive surface, an electron interacts with its own image potential. The image potential originates from the polarization charge at the surface induced by the electron itself. It exerts an attractive force onto the electron. Inside a gap of the bulk band structure, the electron may be trapped between the bulk crystal barrier and the image-potential surface barrier by reflection. The long-range Coulomb potential causes a Rydberg-like series of bound states. In one dimension, the image potential can be approximated by

$$V(z) = -\frac{e^2}{4\pi\epsilon_0}\frac{1}{4z}. \tag{2.1}$$

Here, z is the direction of the surface normal, e the electron charge, and ϵ_0 the permittivity of free space. With an infinite crystal barrier at $z = 0$, the binding energies of the states with respect to the vacuum level E_V are given by (Echenique and Pendry 1978)

$$E_\mathrm{V} - E(n) = \frac{Ry}{16n^2} = \frac{0.85\,\mathrm{eV}}{n^2}, \qquad n = 1, 2, \ldots \quad . \tag{2.2}$$

The dispersion parallel to the surface is free-electron-like, with effective mass m^*/m close to unity:

$$E(\boldsymbol{k}_\perp) = E(n) + \frac{\hbar^2 \boldsymbol{k}_\perp^2}{2m^*} \tag{2.3}$$

The image-potential states can be described by a multiple-reflection model, combined with a two-band approximation (Smith 1985, Garrett and Smith 1986) (see also section 2.2.2). They are located a few Ångstrøm in front of the surface, thus overlapping only little with the bulk states.

The image states track the work function of the sample, which is the difference between the vacuum level and the spectroscopic reference level, that is the Fermi level. A broad image-state peak energy signifies an inhomogeneous work function and reflects the presence of a rough surface. This characteristic is used as one criterion to check the quality of film growth in the present work (see section 4.2).

The above-mentioned intrinsic surface states are related to the clean and well-ordered surface of a crystal with two-dimensional translational symmetry. They include the states arising from relaxations and reconstructions. In addition, there are extrinsic surface states related to imperfections such as step edges and impurities. The defect-derived states do not exhibit any two-dimensional translational symmetry parallel to the surface. Their wave functions are localized near the defects. Furthermore, adsorbates may produce extrinsic surface states. Forming two-dimensional lattices with translational symmetry along the surface, adsorbates may form two-dimensional band structures such as intrinsic surface states.

In inverse photoemission, a spectral feature can be experimentally identified as surface state if the subsequent three requirements are satisfied: First, surface states do not show any dependence on $\boldsymbol{k}_{vac,\perp}$. Second, surface states are very sensitive to the level of surface contamination by adsorbates. Third, surface states appear in gaps of the bulk band structure as mentioned above.

Conceptually similar to surface states are interface states (Rader et al. 1994). They are of interest concerning the perpendicular anisotropy (Wang et al. 1994). Interfaces also govern spin-dependent electron reflectivity, which results in the confinement of electrons. The corresponding electronic states in thin films are introduced in the subsequent section.

2.2 Quantum-well states in metallic thin films

When electrons are confined to dimensions comparable to their wavelength, the continuum of bulk energy bands becomes quantized into discrete states. The solid-vacuum interface is responsible for the surface states described above. Concerning thin films deposited on a solid, the additional solid-film interface may lead to a further kind of electronic states. The potential barriers, originating from the film-vacuum interface on the one side and from the film-solid interface on the other side of the film, may lead to an electron confinement inside the film. This is shown in the upper part of figure 2.1. The same is true for a film which is limited on both sides by a film-solid interface (lower part of figure 2.1). An electron inside the film may be reflected at the interfaces if the electronic structure of the solid does not provide any matching states. When the thickness of the film is below the coherence length of the electrons, the incident and reflected wave functions interfere. Constructive interference is possible at certain discrete energies. This leads to standing electron waves, which are denoted as quantum-well (QW) states. The discrete electronic structure is reflected in an oscillating density of states (DOS). This is responsible for a variety of quantum-size effects (Jalochowski 1995). If a non-magnetic film is limited by a magnetic film, the quantum-well states inside the non-magnetic film are spin-polarized. With two magnetic films separated by a non-magnetic spacer layer, the spin-polarized quantum-well states of the non-magnetic spacer layer may transfer the magnetic information that is responsible for the magnetic coupling between the two magnetic films.

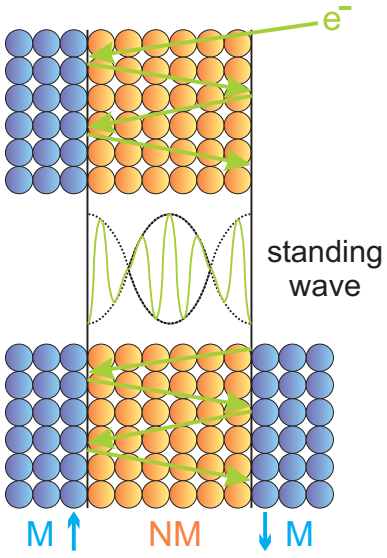

Figure 2.1: A non-magnetic thin layer (NM) is limited by a magnetic solid or layer (M) on one side and by vacuum on the other side (upper part) or by two magnetic layers (lower part). The spin-dependent potential barriers at the interfaces may lead to the formation of spin-polarized standing electron waves or quantum-well states in the non-magnetic layer.

In this section, the formation of discrete quantum-well states in thin Co and Ni films on Cu(001) is demonstrated by means of a comparison between the band structures of the respective materials. Moreover, the modeling of the thickness dependence of

the quantum-well state energies, using the phase-accumulation model, is introduced. Finally, the transition from discrete electronic states to a continuous bulk-like energy band is described.

2.2.1 Thin Co and Ni films on Cu(001)

For a film grown on a solid substrate, electrons can couple across the interface. The electron confinement and discretization of electronic states in the film is limited to special regions of the reciprocal space where the bulk electronic structure of the substrate has a gap of same symmetry and spin.

The bulk band structure for Co(001) and Cu(001) is shown in figure 2.2 (Braun 2005). The graph displays the energy E relative to the Fermi level E_F as a function of the electron momentum $\boldsymbol{k}_\perp$ along the [001] direction from Γ to X. On the left-hand side, the spin-resolved energy bands for Co(001) are shown, for majority electron spin in green and for minority electron spin in red. The majority d bands are entirely below the Fermi level and are therefore completely filled. In contrast, the minority d bands cross the Fermi level. They are only partly below the Fermi level and are therefore only partially filled. That is why Co is a strong ferromagnet. Above the Fermi level there is a Shockley-inverted energy gap, in that one the lower edge of the energy gap is p-like and the upper edge of the gap is s-like. On the right-hand side the band-structure for Cu(001) is shown for comparison. For Cu, the band structure also shows a Shockley-inverted energy gap above the Fermi level, but is shifted downwards in energy compared to Co. Vertical arrows indicate bulk-like direct optical transitions with fixed photon energy $\hbar\omega = 9.4\,\mathrm{eV}$, which are accessible by the inverse photoemission set-up at normal electron incidence on a (001) surface (see section 4.1.2).

Electron confinement in thin films requires a *relative* energy gap between the film and the substrate in a particular direction. The top of the Δ_1 *sp* band at the lower edge of the band gap at the X point, namely the $X_{4'}$ symmetry point, is for Cu $E^{Cu}_{X_{4'}} = 1.80\,\mathrm{eV}$ and for Co $E^{Co\uparrow}_{X_{4'}} = 2.50\,\mathrm{eV}$ for majority spin and $E^{Co\downarrow}_{X_{4'}} = 2.70\,\mathrm{eV}$ for minority spin. The difference between these lower edges of the band gaps in Cu and Co is responsible for the formation of discrete quantum-well states. The $X_{4'}$ point for Co is located 0.70 eV for majority spin and 0.90 eV for minority spin higher in energy than for Cu. In this limited energy range, complete electron confinement in Co is expected. Because of the energy gap in Cu, the electrons cannot couple to electronic states in Cu. Therefore, quantum-well states are expected to be formed in this energy range. As the energy of the $X_{4'}$ point for Co depends on the electron spin, also a spin-dependence of the quantum-well states is expected due to spin-dependent reflection at the interface. The spin-dependent reflection is closely related to the magnetic exchange coupling between magnetic thin films (Mathon et al. 1995, Mathon et al. 1997). In addition to the relative gap, confinement can be accomplished by the so-called symmetry gap or hybridization gap: For electron energies below $E^{Cu}_{X_{4'}} = 1.80\,\mathrm{eV}$, only partial electron confinement is possible due to reasons of symmetry. The reflectivity is lower than in the energy range of the band gap. The states are coupled to bulk states, but still show an enhanced modulation of the amplitude in the film. These partially confined states are referred to as

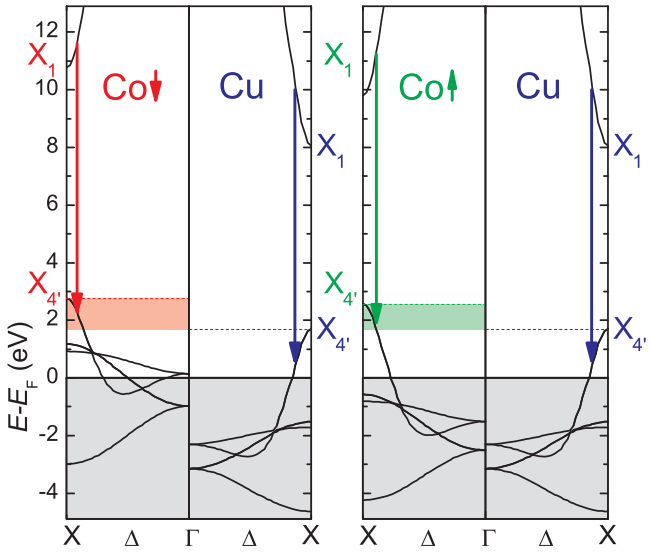

Figure 2.2: The energy bands $E(\boldsymbol{k}_\perp)$ along the [001] direction from Γ to X for $\mathrm{Co}_{\downarrow,\uparrow}$ in comparison with Cu. In the shaded energy ranges between the lower band-gap boundaries $X_{4'}$ of $\mathrm{Co}_{\downarrow,\uparrow}$ and Cu complete electron confinement is possible. Vertical arrows indicate direct optical transitions accessible by inverse photoemission.

quantum-well resonances.

For Ni(001), the bulk band structure is shown in figure 2.3 in comparison with Cu(001) (Braun 2005). The band structure of the ferromagnetic Ni(001) along [001] is similar to the one of Co(001). In particular, only minority d bands exist above the Fermi level. The majority d bands are completely occupied. This may be different for thin films (see section 5.2). In contrast to Co, the difference of $E^{Ni\uparrow}_{X_{4'}} = 2.74\,\mathrm{eV}$ for majority spin and $E^{Ni\downarrow}_{X_{4'}} = 2.78\,\mathrm{eV}$ for minority spin is much smaller. It amounts to 0.04 eV only. Thus, a likewise smaller spin dependence of the quantum-well states and a smaller spin splitting is expected.

Concerning a thin Co film on a Cu(001) substrate, the film is limited by the Co-Cu interface on one side and by the Co-vacuum interface on the other side. As the reflectivity due to the vacuum barrier is always high, quantum-well states are expected in the energy range described above. The same is true with another Cu film on top, so that the Co film is limited by two Co-Cu interfaces. In a thin Cu film on Co, only partial electron confinement is possible, because in the energy range of the Cu bands there is no energy gap for Co. Hence, only quantum-well resonances are expected. If two different thin films are deposited on a substrate, for instance Cu on Co on Cu(001), then there are three interfaces, namely Cu-Co, Co-Cu and Cu-vacuum. This represents a double quantum well. Depending on the thickness of the films, quantum-well states as well as resonances in the two films are expected. In addition, the formation of double quantum-well states due to a confinement in both films is possible. The dependence of quantum-well states on the film thickness is described in the next section.

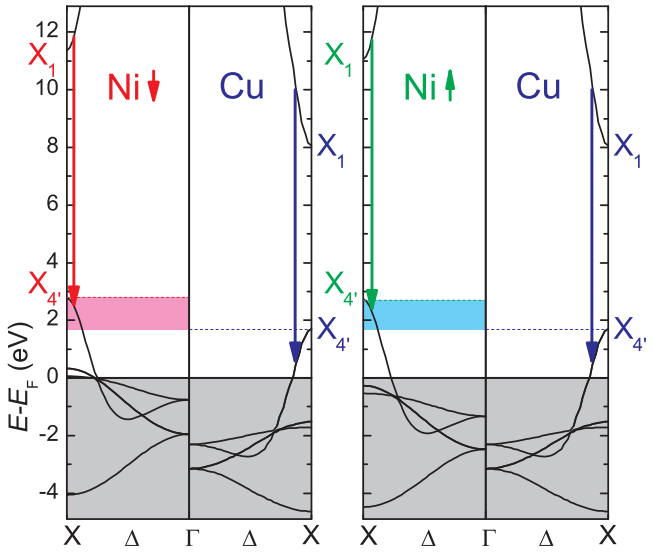

Figure 2.3: The energy bands $E(\boldsymbol{k}_\perp)$ along the [001] direction from Γ to X for $\mathrm{Ni}_{\downarrow,\uparrow}$ in comparison with Cu.

2.2.2 The phase-accumulation model

The discretization of the band in a thin film is described by the phase-accumulation formalism. This was first introduced for surface states (Echenique and Pendry 1978) and later applied to quantum-well states (Smith 1985, Smith et al. 1994). For thin films, the model gives the energy levels of the discrete quantum-well states depending on the film thickness. For a one-dimensional square well, the discrete states shift down in energy with increasing well thickness. By contrast, quantum-well states in thin films typically shift up in energy with increasing film thickness. The latter behavior can be confirmed by the phase-accumulation model.

The phase-accumulation model describes the discrete states as a result of multiple reflections of the electrons at both adjacent interfaces of a quantum well. In figure 2.4, these multiple reflections are illustrated in a schematic potential diagram showing the energy E as a function of the distance from the film-substrate interface z. The electrons are reflected on one side by the relative band gap of the substrate with the reflection coefficient r_C and the phase shift Φ_C. On the other side they are reflected by the image potential of the film surface with the reflection coefficient r_B and the phase shift Φ_B. For zero film thickness, the lowest energy solution is a crystal-induced surface state, and the higher energy solutions are the image-potential induced surface states. For finite film thickness, the energy solutions lead to discrete quantum-well states.

The phase-accumulation model is a direct consequence of the Bohr-Sommerfeld quantization rule. To obtain constructive interference of the wave functions, the phase accumulation in a round trip within the well must be equal to an integer number of 2π. With the phase shift Φ_C at the film-substrate interface and the phase shift Φ_B at the film-vacuum interface, the phase-accumulation condition for a film

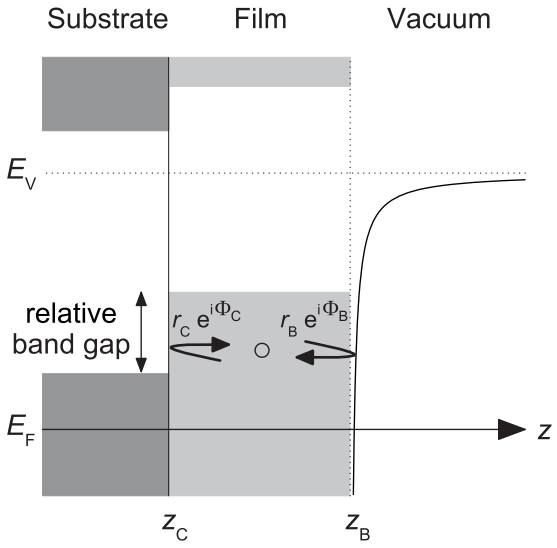

Figure 2.4: Schematic diagram illustrating the multiple reflections of the electrons in a film between the potential barrier of the substrate and the image potential on the vacuum side at an energy corresponding to a relative band gap in the substrate.

with thickness d is

$$2k_\perp d + \Phi_\mathrm{B} + \Phi_\mathrm{C} = n\,2\pi, \qquad n = 1, 2, \ldots \quad . \tag{2.4}$$

Here, $k_\perp = |\boldsymbol{k}_\perp|$ is the electron momentum perpendicular to the surface. The integer quantum number n indicates the number of half-wavelength or antinodes of the corresponding wave function.

The condition 2.4 predicts two properties which are contrary to the experimental observations. First, for fixed n, the quantum-well energies decrease in energy with increasing film thickness. But nearly all experiments report on increasing quantum-well energies when the film thickness is increased (Himpsel et al. 1998, Chiang 2000, Milun et al. 2002, Qiu and Smith 2002) (see also section 5.3). Second, the oscillation periodicity at the Fermi level is π/k_F (k_F Fermi wave vector). Instead, the experimental observation is $\pi/(k_\mathrm{BZ} - k_\mathrm{F})$ ($k_\mathrm{BZ} = \pi/a$ Brillouin zone wave vector). The crux of the problem is the discrete film thickness. Taking the film thickness d as an integer multiple of the interlayer spacing a, $d = ma$, this leads to

$$m\,2k_\perp a = n\,2\pi - \Phi_\mathrm{B} - \Phi_\mathrm{C}. \tag{2.5}$$

Introducing the new quantum number $\nu = m - n$, the phase accumulation condition finally reads

$$m\,2k_\perp^e a = \nu\,2\pi + \Phi_\mathrm{B} + \Phi_\mathrm{C}. \tag{2.6}$$

As $k_\perp^{\mathrm{e}} = k_{\mathrm{BZ}} - k_\perp$ decreases with increasing energy, in this case the energy of the quantum-well states increases with increasing film thickness and the oscillation periodicity of $\pi/(k_{\mathrm{BZ}} - k_{\mathrm{F}})$ at the Fermi level corresponds with the experiments.

The $k_\perp^{\mathrm{e}}$ is characteristic of an envelope function that modulates the quantum-well wave function (Ortega et al. 1993). In the envelope function picture commonly used in semiconductor quantum-well structures (Bastard 1988), the perpendicular component of the wave function is represented by a rapidly oscillating Bloch function modulated by an envelope function (see section 2.2.3). The Bloch function, with momentum $k_\perp^{\mathrm{edge}}$, originates from the bulk states at the nearest band edge. The envelope function, with momentum $k_\perp^{\mathrm{e}}$, satisfies the boundary conditions at the interfaces. The envelope-function picture and the phase-accumulation picture are equivalent (Smith et al. 1994, Qiu and Smith 2002).

For $d = ma$, equations 2.4 and 2.6 are identical. For a non-integer number of layers m' with $m < m' < m + 1$, the quantum-well states consist of two sets of discrete states corresponding to $d = ma$ and $d = (m + 1)a$. When m' increases from m to $m + 1$, the quantum-well states continuously evolve from the set of $d = ma$ to the set of $d = (m + 1)a$. This behavior is given by equation 2.6. Thus, the thickness of the film is given by

$$\frac{d_\nu(E)}{a} = \frac{\frac{1}{2\pi}(\Phi_{\mathrm{B}}(E) + \Phi_{\mathrm{C}}(E)) + \nu}{1 - \frac{k_\perp(E)}{k_{\mathrm{BZ}}}}. \tag{2.7}$$

To determine the energy of the quantum-well states as a function of the film thickness, the energy dependence of the phase shifts $\Phi_{\mathrm{B}}(E)$ and $\Phi_{\mathrm{C}}(E)$ as well as of the electron momentum $k_\perp(E)$ has to be known. The phase shift at the film-vacuum interface for the image potential at a metal surface can be calculated using the Wentzel-Kramer-Brillouin (WKB) approximation, if the energies of the quantum-well states are far from the vacuum level E_{V} and from the band bottom (McRae and Kane 1981):

$$\Phi_{\mathrm{B}}(E) = \pi\sqrt{\frac{3.4\,eV}{E_{\mathrm{V}} - E}} - \pi. \tag{2.8}$$

The phase shift at the film-substrate interface depends on the character of the energy band gap. For reflection due to a band gap, Φ_{C} generally increases by π on traversing the gap (Pendry and Gurman 1975). For a *sp*-band gap, the quantum-well states have to couple to an evanescent wave penetrating into the substrate. As in Shockley-type surface states, the wave function will be *p*-like at the lower edge of the energy gap E_{L}. It shows a node in the atomic position. Thus, the phase shift is $\pm\pi$. At the upper edge E_{U}, the wave function will be *s*-like having a maximum at the atomic position. Hence, the phase shift is zero. The following empirical formula has been found for the behavior of the phase shift inside the gap (Echenique and Pendry 1989):

$$\Phi_{\mathrm{C}}(E) = 2\arcsin\sqrt{\frac{E - E_{\mathrm{L}}}{E_{\mathrm{U}} - E_{\mathrm{L}}}} - \pi. \tag{2.9}$$

Outside the band gap, Φ_C is kept the same as that one at the respective boundary. The dispersion of the electrons inside the film is modeled by a parabolic form, which involves a spin-dependent free parameter G:

$$E(k_\perp) = -G(k_\perp - 1)^2 + E_U. \tag{2.10}$$

The free parameter is used to fit the calculated thickness dependence to the experimental data. To illustrate the above-mentioned findings, the thickness dependence of the energies of the quantum-well states for Co films on Cu(001) (Yu et al. 2003*b*) is shown in figure 2.5 for majority spin. The used values are $a = 1.8$ Å, $E_V = 5.0$ eV, $E_U^{Co\uparrow} = 2.55$ eV and $E_L^{Cu} = 1.80$ eV. The graph displays the energy as a function of the phase over 2π. The blue curves show the phase shift inside the film, $m\ 2k_\perp a$, indicated by the number of layers m. The green curves show the phase shift at the interfaces combined with the phase accumulation condition $n\ 2\pi - \Phi_B - \Phi_C$, indicated by the quantum number n. At the points of intersection of the green and blue curves, the phase accumulation condition is fulfilled for an integer number of layers. Hence, quantum-well states will show up. The red curves show the film thickness $\frac{d_\nu(E)}{a}\frac{k_\perp(E)}{k_{BZ}}$, calculated from equation 2.7, which represent the experimental behavior. The phase-accumulation model is applied for thin Ni films on Cu(001) in section 5.3.

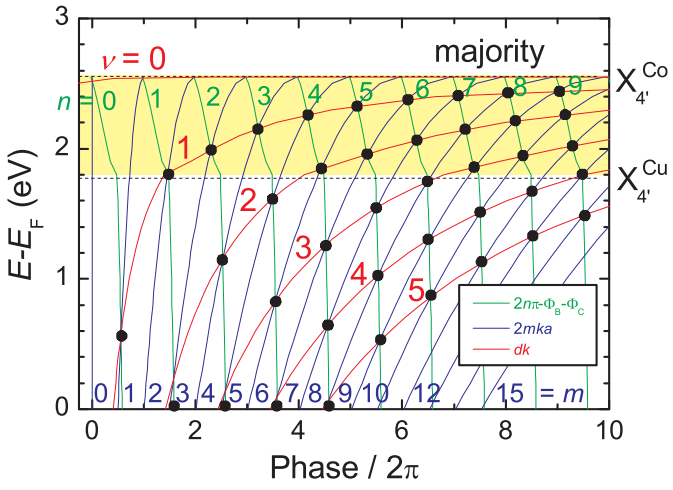

Figure 2.5: The energy of the quantum-well states as a function of the phase over 2π calculated by the phase accumulation model. See text for details.

For very low coverage, the quantum-well model fails, because the two interface potentials of the film are modified by each other. For this low coverage, the behavior of the discrete states can be described by an empirical tight-binding method (Smith et al. 1994). Otherwise, first-principles local density theory can be used to gain information about the interfaces (Crampin 1993, Wu et al. 1996).

2.2.3 Transition from discrete states to bulk bands

Quantum-well states diminish when the film thickness becomes larger than the mean free path of the electrons because of the loss of phase coherence. With increasing film thickness, a transition from two-dimensional discrete quantum-well states to a three-dimensional continuous bulk band occurs.

The quantization of a continuous bulk band can be described in a simple model (Mugarza 2002). For a sufficiently thick film, the phase shift at the interfaces can be neglected in a first approach ($2k_\perp d \gg \Phi_B + \Phi_C$). The phase accumulation condition simplifies to

$$2k_\perp d = n\,2\pi, \qquad n = 1, 2, \ldots, m \quad . \tag{2.11}$$

This condition defines a set of discrete perpendicular electron momenta

$$k_\perp = n\,\frac{\pi}{d} = n\,\frac{\pi}{ma}. \tag{2.12}$$

As a consequence, for a m layer thick film, the bulk band is split into m equidistant discrete states of spacing π/d. This is shown in figure 2.6 for $m = d/a = 10$. The graph displays the energy as a function of the electron momentum along the Δ direction corresponding to ΓX in terms of the Brillouin zone. It shows a schematic energy band as solid black line and discrete quantized states as blue data points. The size of the Brillouin zone is $k_{BZ} = \pi/a$. By increasing the number of layers, the number of discrete quantum-well states also increases, and they shift towards the band edge. In the limit $m \to \infty$, the bulk band continuum is formed.

The discrete energy levels are sharp as long as the electron wave function is truly confined to the film. Considering the phase shifts Φ_B and Φ_C at the interfaces, the number of states will still be m. The energy levels and $k_\perp$ points move, but remain discrete. Strictly speaking, $k_\perp$ is not a well-defined quantum variable owing to the finite size of the corresponding wave train confined to the film. According to the Heisenberg uncertainty relation, the uncertainty in $k_\perp$ is inversely proportional to the film thickness d and therefore of the same order of magnitude as the spacing between adjacent $k_\perp$ points.

Furthermore, for general boundary conditions, a finite penetration of the electron wave function into the substrate is expected owing to a phase shift $\Phi_C \neq \pm\pi$. The decay constant is proportional to the square root of the energy distance to the band edge of the substrate. In order to obtain a sharply confined wave function, a large band gap and a quantum-well energy around the middle of the gap are required. With increasing film thickness, the density of $k_\perp$ points increases and the states move towards the band edge.

The phase accumulation condition defines a unique momentum $k_\perp$ which is broadened due to the finiteness of the electron wave function. Thus, the momentum distribution will be centered at this momentum $k_\perp$, which coincides with the corresponding bulk momentum. The smaller the confining region, the broader the momentum distribution. Figure 2.7 shows the energy dispersion along the Δ direction of the Ni *sp* band as black solid line (see section 2.2.1) and discrete quantized

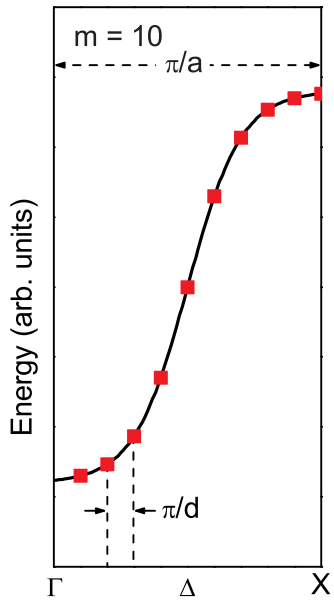

Figure 2.6: Schematic band and discrete quantum-well states. The graph shows the energy as a function of the electron momentum along the [001] direction corresponding to ΓX in terms of the Brillouin zone.

states for $m = 5$ (left-hand side) and $m = 10$ (right-hand side) as red data points. The discrete energy levels of the first five quantum-well states are taken from the Ni phase-accumulation modulation (see section 5.3). The momentum broadening is indicated by red solid lines. Furthermore, the blue curve indicates the final state energies of detectable transitions with fixed photon energy of $\hbar\omega = (9.4 \pm 0.2)\,\mathrm{eV}$ (see section 4.1.1). The error bar, as indicated by the cyan area, comes from the overall resolution of the inverse photoemission experiment. For $m = 5$, three transitions into discrete states are possible as shown by the blue arrows. For $m = 10$, the discrete states have moved towards the band edge, and their distance in $k_\perp$ is decreased. In addition, the momentum broadening will be decreased. Now four transitions into discrete states may be possible. The discrete state at highest energy cannot be detected anymore, because it is shifted up in energy and the momentum broadening is decreased, so that no crossing with the final state energies of detectable transitions is possible. Moreover, neighboring discrete states cannot be distinguished anymore when the energy distance between them is below the overall resolution of the inverse photoemission experiment.

Concerning a more exact description of the behavior of discrete states as a function of the film thickness, a detailed knowledge of the uncertainty in $k_\perp$ is crucial. Concerning this, the determination of the cross sections by using a variable photon energy is necessary. The photon energy dependence of the cross section of Cu films on Co(001) with a thickness ranging from 3 to 6 monolayers has been analyzed by photoemission in order to extract the effective confinement of the different quantum-well state wave function present in each film, but the interpretation suffers from a

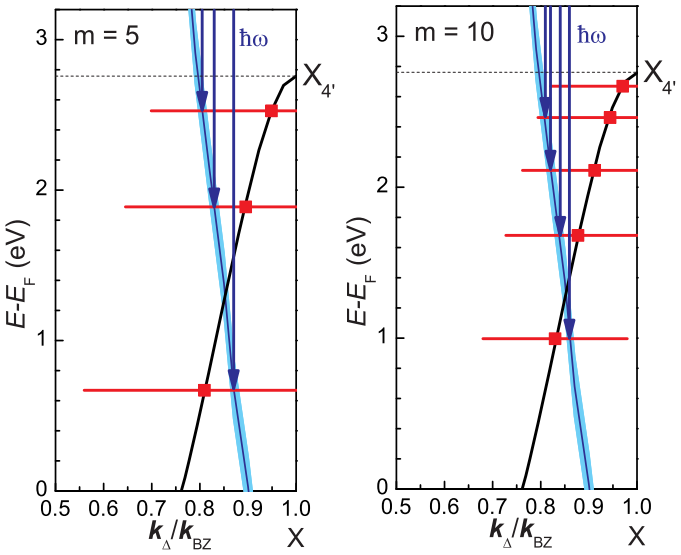

Figure 2.7: Spin-averaged Ni *sp* band and discrete quantum-well states for $m = 5$ (left-hand side) layers and $m = 10$ layers (right-hand side). The graph shows the energy as a function of the electron momentum k_Δ/k_{BZ} along the [001] direction Δ. The discrete energy levels are taken from the Ni phase-accumulation modulation (see section 5.3).

lack of data points (Mugarza et al. 2000).

For the detection of discrete quantum-well states, a particular flat film is required. Otherwise, when the film contains regions with different film thickness, quantum-well features appear at likewise different energies. As a consequence, the spectral features may appear quite broad when containing contributions from different quantum-wells. The next chapter focuses on film growth and further properties of the films investigated in the present study.

Chapter 3

Ni and Co films on Cu(001)

The growth mode of a film is crucial for the analysis of any electronic quantum-interference phenomena. Since the quantum-well energy levels strongly depend on the film thickness, atomically uniform or flat interfaces are required. After shortly outlining general aspects of film growth and magnetism, in this chapter the properties of the investigated thin films are described, namely growth, structure, and magnetism of ultrathin Ni and Co films on a Cu(001) substrate, as well as of bilayers containing Cu.

3.1 General aspects of film growth and magnetism

Film growth

The growth mode of ultrathin epitaxial films on metallic single crystal substrates is determined by a number of parameters like lattice mismatch between the substrate and the film, the substrate temperature during growth, the deposition rate, and the surface free energies of both the substrate and the film (Brune 2001). The term epitaxy describes the oriented growth of one crystal on another crystal. In homoepitaxy film and substrate are of the same material whereas in heteroepitaxy they are of a different material. The latter is of more practical relevance.

Close to thermodynamic equilibrium it is irrelevant how and where the nucleation of particles takes place. Equilibrium growth occurs at a slow (near-equilibrium) deposition rate in the absence of a large temperature gradient or other strong non-equilibrium factors. For equilibrium growth, three different growth modes are possible. These are based on simple thermodynamics driven by the macroscopic surface tensions, which are the surface free energies per unit area, of the substrate (γ_s), the overlayer (γ_o), and the interface (γ_i) (Bauer 1958). Neglecting the strain energy of the overlayer, the two-dimensional layer-by-layer growth (Frank-van der Merwe growth (Frank and van der Merwe 1949)) is favored if the interaction between substrate and layer atoms is stronger than the one between neighboring layer atoms ($\gamma_s \geq \gamma_o + \gamma_i$). In this case, the system gains energy when totally covered by the overlayer (*wetting* of the substrate). The three-dimensional island growth (Volmer-Weber growth (Volmer and Weber 1926)) is favored if the interaction between neighboring overlayer atoms exceeds the interaction between the overlayer and

the substrate ($\gamma_s \leq \gamma_o + \gamma_i$). This results in an only partially covered substrate and in a three-dimensional growth morphology. Now considering the strain energy of the overlayer, the layer growth followed by three-dimensional island growth (Stranski-Krastanov growth (Stranski and Krastanov 1938)) occurs due to the strain in the overlayer if the substrate and the overlayer material are structural mismatched on a microscopic scale. In this case, pseudomorphic growth results in a monotonic increase of volume strain energy in the two-dimensional overlayer with increasing film thickness. This leads to an unstable situation at a certain thickness and the system changes to three-dimensional island growth in order to reduce the strain energy.

These three growth modes phenomenologically describe the behavior of perfectly flat substrates only. But real substrates offer defects like step edges and lattice imperfections. Far from the thermodynamic equilibrium, the growth is strongly influenced by kinetic processes. In non-equilibrium growth, surface steps are starting to play a dominant role (Burton et al. 1951). A high mobility of adatoms owing to high temperature or low deposition rate may result in the capturing of adatoms at the pre-existing step edges instead of the formation of stable nuclei. If the mean distance an adatom can travel before encountering another adatom or an existing nucleus is larger than the terrace width, no islands are formed since all atoms reach the ascending substrate steps to which they attach. This absence of nucleation results in the advancement of steps over the lower terraces. During growth, the surface roughness remains constantly that one of the substrate. This growth mode is called step-flow mode. However, in heteroepitaxy high growth temperatures would lead to interdiffusion and therefore are avoided. When the growth is at low temperature or high deposition rate, kinetic arguments may be the dominant ones. In this case, the diffusion barriers of the lattice and the step edge (Ehrlich-Schwoebel barrier (Ehrlich and Hudda 1966, Schwoebel 1969)) play an important role. The Ehrlich-Schwoebel barrier may suppress the transport between different layers. Thus, the arriving adatoms nucleate on the top of clusters giving rise to the growth of three-dimensional islands. Anisotropic lattice barriers lead to anisotropic clustering, which in turn can be used to grow different nanostructures. Two effects of adatom mobility influence the growth mode. A small adatom mobility is required in the nucleation stage resulting in a large density of nuclei. On the other hand, a high adatom mobility is required in the growth stage allowing the adatoms to effectively move over the steps. In order to achieve layer-by-layer growth, a compromise between these two effects has to be found.

Furthermore, the quality of the interfaces plays an important role. Lateral smoothness and vertical sharpness are needed. The formation of quantized electronic states requires interfaces which are smoother than the wavelength of the confined electrons (0.4 nm for 10 eV electrons). The roughness of an interface is mainly determined by the growth modes, whereas its sharpness depends on interdiffusion and chemical reaction (Weaver 1986).

Magnetism

Magnetic phase transitions

Ferromagnetism reflects the underlying band structure. The magnetic moment is derived from the imbalance of minority and majority spin electrons, which is related

to the ferromagnetic exchange splitting between the minority and majority spin band. The minimization of the total energy over all occupied band states yields the crystal structure as well as the magnetic ordering.

A ferromagnet is spontaneously magnetized below the Curie temperature T_C owing to the exchange interaction. The latter is a consequence of the Pauli exclusion principle and the Coulomb interaction between electrons and is responsible for the alignment of the electron spins. Because of the Pauli principle, two electrons with parallel spin cannot occupy the same orbital state and have a greater average distance than two electrons with antiparallel spin. Thus, the effective Coulomb repulsion between a pair of electrons with parallel spins is weaker than the one between a pair of electrons with antiparallel spins. Therefore, the alignment of spins may decrease the ground state energy of the system. Otherwise, the kinetic energy of the system is increased, because some electrons have to occupy different states. All in all, a spontaneous alignment of the spins is possible if the decrease in Coulomb repulsion energy is greater than the increase in kinetic energy. The aligned spins of a ferromagnet result in a net magnetic dipole moment and create a magnetic field.

To describe the ferromagnetism of solids different models are applied depending on the degree of localization of the valence electrons, which carry the magnetic moments. The Heisenberg model (Heisenberg 1928) is a nearest neighbor spin model and suitably describes the ferromagnetism of mostly localized electrons found in materials such as $3d$ metal oxides, $4f$ metals, and their compounds. The Ising model, a special case of the Heisenberg model, considers the spin alignment along one direction only and thus is suitable to describe ferromagnets with a strong uniaxial anisotropy (Nolting 1986). In systems with delocalized electrons like transition metals the interaction between the electrons in the partially filled d or f shells is very strong and the conduction band is very narrow. In the band-ferromagnets Fe, Co, and Ni, the $3d$ band is overlapped in energy by a much wider $4s$ band. Since bands are filled up to the Fermi level, electrons from both the $3d$ and the $4s$ band contribute to the conduction band. As a consequence, the number of d electrons per atom contributing to the bulk magnetization is not an integral number. For simplification, the collective or itinerant electron ferromagnetism theory assumes a completely delocalized, free-electron gas, but puts a non-integral number of Bohr magnetons at the lattice sides. The simplest model for describing the interplay between localization and band formation in a solid is the one-band Hubbard model (Hubbard 1963, Hubbard 1964*a*, Hubbard 1964*b*), which is based on the tight-binding approximation. The vast set of bound and continuum electron levels of each ion is reduced to a single localized orbital level. The little overlap of the localized orbitals of neighboring ions allows the consideration of the intraatomic Coulomb repulsion between electrons only. The Stoner model (Stoner 1936, Stoner 1939) is a mean- (or molecular-) field approximation (Weiss and Foëx 1926) of the Hubbard model. The mean-field theory assumes that all spins are influenced by an identical average exchange field produced by all their neighbors. For a ferromagnet, this molecular field will act so as to align neighboring magnetic moments. The field is proportional to the magnetization, which is the dipole moment per unit volume. The Stoner model results in a spin-split band structure where the density of states for minority and majority electrons is shifted by the exchange energy creating a spin imbalance that produces the magnetic moment. According to the Stoner criterion,

ferromagnetic order at zero temperature occurs if the intraatomic Coulomb interaction times the nonmagnetic density of states at the Fermi level is greater than unity. The Stoner criterion is only fulfilled for Fe, Co, and Ni.

The exchange splitting, which is the shift between the density of states for minority and majority electron spin, decreases with increasing temperature. Consequently, also the magnetization strongly depends on the temperature. Near the magnetic phase transition at the critical temperature T_C, that is the Curie temperature for ferromagnets, the magnetization $\boldsymbol{M}$ shows a critical behavior, described by the power law

$$|\boldsymbol{M}| \propto \left(1 - \frac{T}{T_\mathrm{C}}\right)^{\beta}, \qquad T \to T_\mathrm{C}. \tag{3.1}$$

The critical exponent β depends on the dimensionality and the number of degrees of freedom for the spin orientation. The three-dimensional values are $\beta = 0.365$ for the Heisenberg model (Ma 1976) and $\beta = 0.326$ for the Ising model (Ferrenberg and Landau 1991). In two dimensions, it is $\beta = 0.125$ for the Ising model (Onsager 1944). There is no long-range order in one- and two-dimensional isotropic Heisenberg models at finite temperature (Mermin and Wagner 1966). At the surface of a semi-infinite solid, the critical exponent is linked to the exchange interaction and amounts to about $\beta = 0.78$ (Binder and Landau 1984).

If the spin orientation is confined in a plane, the xy model can be applied (Ma 1985, Bland and Heinrich 1994). In this model spontaneous magnetization does not appear, but rather infinite magnetic susceptibility. Hence any small external field or anisotropy in the plane of a film will produce a substantial magnetization in the film. The easy direction of magnetization lies in the film plane, yet no direction in that plane is preferred. In this case, it is $\beta = 0.345$ for three dimensions (Harris 1999) and $\beta = 0.23$ for two dimensions (Bramwell and Holdsworth 1993). Concerning phase transitions (Blundell 2001), the order of a phase transition is the order of the lowest differential of the free energy which shows a discontinuity at the transition. There is no long-range order at finite temperature and zero applied field and no continuous second-order phase transition in the xy model. Instead, the system exhibits a Kosterlitz-Thouless phase transition from an disordered state at high temperature, where the spin-spin correlation decays exponentially, into a state with infinite correlation length at low temperature, where the spin-spin correlation decays only algebraically (Kosterlitz and Thouless 1978). The correlation length is the average distance over which fluctuations of the magnetization are correlated. The Kosterlitz-Thouless phase transition is an infinite-order phase transition and is continuous. It is called a topological phase transition, because there is no symmetry breaking. Experimentally, two sets of β values are found: $\beta \approx 0.125$ next to the one of the Ising model and $\beta \approx 0.23$ next to the one of the xy model (Huang et al. 1994).

Furthermore, the Curie temperature in thin films depends on the film thickness (Erickson and Mills 1991). For the second-order phase transition, the spin-spin correlation length ideally diverges at the Curie temperature. If the film thickness is in the same order than the correlation length, the phase transition becomes destabilized. Hence, it occurs at lower temperature. The thickness dependence of the

Curie temperature may be analyzed within the theory of finite-size scaling resulting in a power law for T_C, characterized by a critical exponent λ (Domb 1973, Schmidt and Schneider 1992). Experimental data from two-dimensional films were found to be well fit by two curves according to this power law, one for the two-dimensional Ising model with strong uniaxial magnetic anisotropy and the other for the planar xy model. The Ising-like films show higher T_C values than the xy -like films. For the latter, T_C is reduced to half its bulk value at a film thickness of about 5 monolayers (ML) and to zero at about 1 ML (Huang et al. 1994).

Magnetic Anisotropy

The magnetization in a ferromagnetic material is not isotropic. There are different kinds of magnetic anisotropy like magnetocrystalline anisotropy, shape anisotropy, surface anisotropy, magnetoelastic anisotropy, and induced anisotropy. These are explained in the following.

The magnetocrystalline anisotropy is caused by the spin-orbit interaction. The electron orbits are linked to the crystallographic structure. The orbital momenta interact with the spins and make them prefer to align along well-defined crystallographic axes. As a consequence, there are directions of easy magnetization, in which it is easier to magnetize a given crystal than in other directions.

The shape anisotropy results from the magnetostatic self-energy. The classical interactions among dipoles lead to a self-energy of magnetic dipoles in their own stray field. Depending on the geometry of the magnetic material, the magnetization aligns such that the self-energy is minimized and the stray-field is low. Thus for a thin film, the alignment of spins and of the magnetization direction, respectively, in the film plane is favored compared to the one perpendicular to the film plane (Yafet et al. 1986).

There are several contributions to the surface anisotropy. Most important is the reduced symmetry at the surface of a ferromagnet (Neél 1954). A spin has a lower number of neighbor spins than in the bulk. Therefore, the exchange energy at the surface is different compared to the one in the bulk. The same may be true for an interface. The surface anisotropy is a geometrical feature, which depends only on the shape of the surface (Brown Jr. 1963). The surface anisotropy may also be caused by the reduced symmetry of the spin-orbit interaction at the surface leading to an energy that depends on the angle between the magnetization at the surface and the crystallographic axes of the material (Aharoni 1986). The effect of the symmetry reduction at a surface on the anisotropy energy has also been examined within band theory leading to a large surface contribution due to the narrowed d band (Š. Pick and Dreyssé 1992, Daalderop et al. 1994).

The magnetoelastic anisotropy occurs if there is a lattice mismatch between a magnetic layer and the substrate. The magnetoelastic anisotropy is a strain-induced modification of the magnetocrystalline anisotropy. Strain in ultrathin films is mainly induced by the lattice mismatch between the film and the substrate. The state of strain depends on the film thickness.

An induced anisotropy appears among others in thin magnetic films (Johnson et al. 1995). When the film is deposited at an oblique angle to the substrate(Cohen et al. 1960), or when a large magnetic (Takahashi 1962) or electric field (Hirsch

et al. 1969) is applied during the deposition, an uniaxial anisotropy may develop in the plane of the film.

Two-dimensional magnetism in thin films requires the presence of magnetic anisotropy to enable ferromagnetic order (Bander and Mills 1988). Long-range magnetic ordering occurs only within the uniaxial Ising model, whereas the two-dimensional isotropic Heisenberg model does not allow ferromagnetic order at finite temperature (Mermin and Wagner 1966). Both the uniaxial anisotropy and the dipolar interaction suppress the long-wave length spin fluctuations at finite temperatures, which in turn stabilize the ferromagnetic order.

For analyzing thin films, the above mentioned bulk expression for the magnetocrystalline anisotropy k_{bulk} has to be supplemented by a thickness-dependent term $k_{\mathrm{interface}}/d$, which contains surface, interface, and strain-induced contributions, averaged over the thickness of the film (Heinrich and Cochran 1993). To this approximation, the bulk term is independent of thickness, whereas the surface and interface term decreases in relative weight as the film thickness d is increased. However, also the bulk term may be thickness-dependent, if strain or alloying with the substrate vary with the film thickness. An example is the double spin-reorientation transition in Ni on Cu(001) (see section 3.2).

In thin films, the shape anisotropy, favoring an in-plane magnetization, competes with the crystalline anisotropy (Pappas 1996). The latter often favors an out-of-plane magnetization (Neél 1954, Daalderop et al. 1994, Wang et al. 1994). With decreasing film thickness, the interface anisotropy may eventually dominate, because its energy scales like $1/d$. This explains the frequent switch from in-plane to out-of-plane magnetization with decreasing film thickness at about 5 ML coverage, e.g. in fcc Fe on Cu(001) (Li et al. 1994). The symmetry of the spin arrangement changes from the xy model for in-plane magnetization to the Ising model for out-of-plane magnetization. At the cross-over point, the film breaks up into striped magnetic domains (Allenspach and Bischof 1992, Speckmann et al. 1995). An exception is Ni on Cu(001) showing an unusual spin-reorientation transition (see section 3.2).

The magnetic anisotropy directly depends on the temperature. The reason is that the anisotropy constants depend on the temperature-dependent magnetization. Thus, also spin-reorientation transitions may depend on the temperature.

3.2 Ni on Cu(001)

Regarding the crystal structure, both Ni and Cu have a face-centered cubic (fcc) crystal structure with lattice constants of $a_{Ni} = 3.52\,\text{Å}$ and $a_{Cu} = 3.61\,\text{Å}$. The nearest-neighbor distances on the (001) surfaces are $a_p^{Ni} = 2.49\,\text{Å}$ and $a_p^{Cu} = 2.55\,\text{Å}$, respectively. The lattice mismatch amounts to 2.5 % only. Hence, Ni on Cu(001) is a good epitaxial system. Ultrathin Ni films on Cu(001) result in a distorted face-centered tetragonal Ni structure. Compared to bulk fcc Ni, the fct Ni lattice is expanded by 2.5 % in the lateral direction and compressed by 3.2 % along the surface normal (Müller et al. 1995). There is no difference in structure with changing magnetization from in-plane to out-of-plane owing to varying film thickness and with a change from ferromagnetism to paramagnetism owing to varying temperature (Platow et al. 1999).

The pseudomorphic growth of Ni films on Cu(001) has been investigated in many studies (Schulz and Baberschke 1994, Shen et al. 1995, Müller et al. 1996, Baberschke 2001). It is layer-by-layer growth up to 3.5 ML Ni film thickness. Subsequent multilayer growth becomes dominant above 6 ML Ni. Above 4 ML Ni, the islands are of rectangular shape, with their edges along the [011] and [$0\bar{1}1$] directions. Above 15 ML Ni, the growth is not pseudomorphic any more, and above 20 ML Ni, the system relaxes into its original bulk fcc structure producing misfit dislocations.

Ni on Cu(001) is thermally stable against interdiffusion to temperatures up to 490 K (Chen et al. 1991). Annealing the film at a temperature of 450 K smoothes the film surface without any significant substrate interdiffusion (Shen et al. 1995, Shen et al. 1996). Nevertheless for submonolayer growth, the interface region is affected by limited intermixing, but this does not influence the magnetic moments of thicker layers (Lindner et al. 2000, Noakes et al. 2003).

Concerning magnetism, in Ni 10 electrons are subdivided between the $3d$ and $4s$ shells. In a free atom, there are 8 electrons in the $3d$ shell and 2 in the $4s$ shell. In a solid, where the bands are filled up to the Fermi level, there are 9.4 electrons per atom in $3d$ and 0.6 electrons per atom in $4s$, which can be concluded from experimental data. The spins in the unfilled shells are not balanced owing to the exchange interaction. The difference between the corresponding moments results in a net magnetic moment of 0.6 Bohr magnetons per atom.

The Curie temperature for bulk Ni is 630 K. For thin Ni films on Cu(001), it is strongly reduced (Huang et al. 1994, Tischer et al. 1994, Baberschke 1996, Baberschke 2001). Below 5 ML Ni, it is smaller than room temperature. Even below 2 ML Ni, the films show ferromagnetic behavior. Moreover, at about 7 ML Ni a crossover from three-dimensional Heisenberg ($\beta = 0.37$) to two-dimensional XY behavior ($\beta = 0.24$) occurs as the film thickness is reduced (Huang et al. 1994). For fct Ni / Cu(001), the in-plane directions of easy magnetization are along $\langle 110 \rangle$ (Schulz and Baberschke 1994, Nünthel et al. 2003).

The spin-reorientation transitions (SRT) of thin Ni films on Cu(001) are illustrated in figure 3.1. With increasing Ni film thickness, the magnetization ($\boldsymbol{M}$) changes from in-plane to out-of-plane orientation at about $7-10$ ML and back to in-plane at about 60 ML (Huang et al. 1994, Schulz and Baberschke 1994, O'Brien and Tonner 1994, O'Brien et al. 1996, Farle et al. 1997*a*, Farle et al. 1997*b*, Fukumoto et al. 2002). The spin-reorientation transitions result from the competition between two contributions. The in-plane magnetization for very low Ni film thickness is driven by surface, interface, and shape anisotropy. The contribution of surface anisotropy is inversely proportional to the film thickness. Above $7-10$ ML Ni, the magnetoelastic volume anisotropy, which results from the mismatch-induced strain and favors an out-of-plane magnetization, becomes dominant and turns the magnetization from in-plane to out-of-plane. The out-of-plane magnetization does not originate from the morphology of the Ni film (Shen et al. 1995, Müller et al. 1996). Surface roughness has a minor effect on this first spin-reorientation transition (Poulopoulos et al. 1999). Furthermore, above the critical thickness for the second spin-reorientation transition at about 60 ML, the Ni film is relaxed into the bulk fcc Ni structure. For this thickness, the influence of the shape anisotropy is decisive forcing the magnetization again in the film plane.

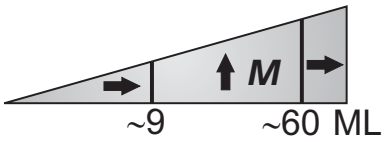

Figure 3.1: Spin-reorientation transition for thin Ni films on Cu(001).

The spin-reorientation transitions are influenced by certain adsorbates. The first spin-reorientation transition shifts to lower thickness by about 3 ML if the film is covered by 0.5 ML CO and by about 4 ML if the film is covered by 0.5 ML H_2 (van Dijken et al. 1999).

A Co overlayer, even below 3 ML thickness, forces the magnetization of Ni films in-plane, because it has a strong in-plane magnetic anisotropy (Kuch et al. 2000). In this case, no spin-reorientation transition occurs. Whereas there is only a rather small influence on the first spin-reorientation transition by a Cu cap layer, the second spin-reorientation transition strongly depends on the thickness of the Cu overlayer (O'Brien et al. 1996, Fukumoto et al. 2002). Both transitions occur at lower Ni thickness with increasing Cu overlayer thickness.

The thickness where the spin-reorientation transition occurs depends on the temperature. By *in situ* ferromagnetic resonance it was shown for 7.6 ML Ni on Cu(001), that the spontaneous magnetization relative to the film normal changes continuously from 90° (in-plane) at 200 K, to 16° at 250 K, to 0° (out-of-plane) above 300 K (Farle et al. 1997*b*, Farle et al. 1997*c*). The continuous reorientation of the magnetization from in-plane at low temperature to out-of-plane at high temperature is caused by the temperature dependence of the volume anisotropy and of the interface anisotropy. On the one hand, both the surface anisotropy as well as the shape anisotropy favor an in-plane magnetization. On the other hand, the magnetoelastic volume anisotropy favors an out-of-plane magnetization. All anisotropy contributions depend on the temperature, but the surface anisotropy decreases faster than the magnetoelastic anisotropy with increasing temperature. Consequently, the magnetization turns to out-of-plane with increasing temperature. The thickness for the reorientation transition shifts to lower temperature if the film thickness is slightly increased, because the surface anisotropy does not depend on the film thickness, but the magnetoelastic anisotropy is proportional to the film thickness.

Furthermore, the thickness of the first spin-reorientation transition depends on the growth temperature. It is about 1 ML smaller for films grown at 170 K than for films grown at room temperature (Zheng et al. 1999). Structure and chemical composition are not changed due to the lower growth temperature, but the morphology differs increasing the island density and decreasing their size. This is believed to change the magnetic behavior.

3.3 Co on Cu(001)

The equilibrium phase of bulk Co is hexagonal close-packed (hcp) at room temperature and face-centered cubic at temperatures above 697 K (Nishizawa and Ishida 1983). The lattice mismatch between Cu and fcc Co is quite small (Hansen 1958).

The lattice constant of the fcc Co phase amounts to $a_{Co} = 3.55\,\text{Å}$ (Cerdá et al. 1993), thus the nearest-neighbor distance on the (001) surface is $a_p^{Co} = 2.51\,\text{Å}$.

On Cu(001), epitaxially grown Co films show pseudomorphic growth and have face-centered cubic crystal structure with a small tetragonal distortion compressed along the surface normal (Clarke et al. 1987, Schneider et al. 1990, Qiu et al. 1992*b*, Cerdá et al. 1993, Heckmann et al. 1994). The lattice mismatch on Cu(001) with $a_p^{Cu} = 2.55\,\text{Å}$ amounts to 1.6 % only. Hence, also Co on Cu(001) is a good epitaxial system. The growth mode is layer-by-layer growth above 2 ML Co (Schmid and Kirschner 1992, Fassbender et al. 1995, Ramsperger et al. 1996) with the initial formation of two-layer-high islands below 2 ML Co (Li and Tonner 1990).

In the literature intermixing of Co and Cu is controversially discussed. For room-temperature growth, it is reported about intermixing of Co and Cu at the very first stages of growth (Pfandzelter et al. 1996, Bernhard et al. 2005). For low coverage, Co-rich regions in the substrate and Cu-rich regions in the topmost layer have been observed (Fassbender et al. 1997). For 5 ML Co grown on Cu(001), the topmost layer contains $15 - 20$ % Cu. The amount of Cu in the Co film surface decreases with increasing Co film thickness. Furthermore, thermally activated Co-Cu exchange processes have important consequences on the film growth (Nouvertné et al. 1999*b*, Pentcheva and Scheffler 2002). At elevated growth temperature (410 K), a two atomic layers thick capping layer containing Co and Cu floats on top of a pure Co film (Bernhard et al. 2005). In contrast, Cu segregation is suppressed at low growth temperature (140 K) (Gruyters et al. 2005, Bernhard et al. 2005). In this case, the Cu(001) surface is covered by a pure Co film. Moreover, at low growth temperature with subsequent annealing, the interfaces are sharper (Ortega et al. 1999, Stamm et al. 1998), especially producing slightly sharper spectral features resulting from quantum-well states in inverse photoemission spectra (Yu et al. 2003*b*).

For coverages of several monolayers, Co-Cu interdiffusion has mainly been reported for films grown at room temperature, which are subsequently annealed (Miguel et al. 1989, Li and Tonner 1990, Miguel et al. 1991, Schmid et al. 1993). Upon annealing, (for films grown at room temperature) microscopic pinholes form serving as channels for the substrate Cu to diffuse to the top of the film via surface diffusion (Schmid et al. 1993). However, upon subsequent annealing the smoothest Cu / Co(001) interfaces are obtained (Segovia et al. 1996, Würsch et al. 1997).

The Curie temperature for bulk Co is 1398 K. For ultrathin Co films on Cu(001), it is strongly reduced (Schneider et al. 1990). At the transition from islands to closed layer growth, it shows a pronounced discontinuity at a critical thickness of 1.8 ML from 200 K to 325 K (Bovensiepen et al. 1999). At the critical thickness the Curie temperature is metastable and varies strongly with time and heat treatment. Below, the sample is ferromagnetic. For Co(001), the in-plane directions of easy magnetization are along $\langle 110 \rangle$ (Schneider et al. 1990).

3.4 Bilayers

When another film is deposited on a Ni or Co film, e.g. Cu, or vice versa, the situation is less favorable. After deposition of the first film, the surface is expected

to be rougher compared to the Cu(001) substrate. However, nearly perfect layer-by-layer epitaxial growth occurs for Cu on fcc Co / Cu(001) (Schmid and Kirschner 1992). Cu grows on top of Co / Cu(001) with the lateral and vertical spacings of bulk Cu(001) (Cerdá et al. 1993).

Likewise, Cu films on Ni / Cu(001) should be unstrained, if the Ni intervening layer is so thin, that the Ni is pseudomorphic with the Cu(001) substrate. This can be confirmed by own LEED measurements. The Cu films are expected to be strained for thick Ni intervening layers, when the Ni regains it equilibrium lattice parameter.

For Ni / Co / Cu(001), the morphology for room-temperature growth without subsequent annealing indicates an incomplete layer-by-layer growth (Dhesi et al. 1999). The average terrace width decreases after Co deposition and increases after Ni deposition, indicating that the Ni films grow by island formation at the step edges of the Co surface.

Furthermore, the existence of quantum-well states indicates the excellent epitaxial growth between Cu, Co, and Ni in the (001) orientation giving rise to atomically flat interfaces of the heterostructures (Wu et al. 2006).

3.5 Electronic structure

3.5.1 Modifications in thin films

In this section, observations of different properties of the electronic structure of thin Ni films on Cu(001) compared to bulk Ni(001) are discussed.

Even if the Ni bulk band structure successfully predicts the energy dependence of two-dimensional quantum-well states in thin Ni films, the electronic structure of thin Ni films was found to be different compared to the one of bulk Ni. Theoretical calculations suggested the $3d$ partial density of states (DOS) of the Ni overlayers to be different from that of bulk Ni (Wang et al. 1982, Tersoff and Falicov 1982, Hjortstam et al. 1996, Yang and Wu 2001, Braun 2005). Hence, there is no indication of an significantly increased density of states at the Fermi level for majority spin in thin Ni films compared to bulk Ni (see section 5.2). For the Co - Cu system, the calculated density of states further shows discrete quantum-well states (van Gelderen et al. 1996).

Changes in lattice and band structure reflect in the density of $3d$ holes. For thin Ni films on Cu(001), it was found by near-edge x-ray-absorption fine-structure (NEXAFS) measurements, that the density of $3d$ holes is reduced compared to bulk Ni (Srivastava et al. 1997). It changes by 20 % from a submonolayer thickness to about 4 ML. The same is true for Co / Cu(001) (Srivastava et al. 1998). The reduction of the density of $3d$ holes is ascribed to a hybridization between the Cu and Ni (Co) d bands resulting in a charge transfer from Cu to Ni (Co) d orbitals (Wang et al. 1982). The charge transfer smoothes out the potential barrier resulting in a larger penetration of the film electron wave functions and hybridization with the substrate electronic states. Above 4 ML Ni (Co), the $3d$ hole density stays constant implying that the band structure of Ni and Co starts to stabilize.

The $3d$ hole reduction further results in a decrease of spin and orbital moments

compared to bulk Ni (Srivastava et al. 1998). Band theory early on predicted for a monolayer Ni on Cu(001) a reduced magnetic moment (Huang et al. 1984). A full-potential linear muffin-tin orbital calculation in a slab geometry resulted in a decrease of the spin moment owing to a hybridization between d bands only for one monolayer Ni on Cu(001), whereas the spin moments in Co and Fe are enhanced at the surface (Hjortstam et al. 1996). Whereas the enhanced spin moments are caused by band narrowing effects at the surface due to a reduction of the coordination number, the Ni-d - Cu-d hybridization to some extent quenches the exchange splitting, producing a spin moment which is lower than in bulk Ni. However, magnetic circular dichroism (MCD) measurements showed that the Ni magnetic moment is constant from 2 to 6 layers Ni (Tischer et al. 1995). A decrease of the $3d$ hole density and of the spin moments due to hybridization was further observed for Ni films ($1-2\,\mathrm{ML}$) on Co / Cu(001) (Dhesi et al. 1999, Dhesi et al. 2000). The hybridization was indicated by *diffuse magnetism* originating from empty s states with opposite spin polarization as the empty d states. However, these findings are in contradiction to Korringa-Kohn-Rostoker Green's function calculations of the ground state moments, which does not predict any reduction of the magnetic moment at the interface of Ni on Co / Cu(001) (Ernst et al. 2000*a*). By the same calculation method it was shown that for Ni on Cu(001) the magnetic moment is significantly reduced only in a monolayer Ni coverage and in the layer at the interface for higher Ni coverage (Ernst et al. 2000*b*). This was further shown by *ab-initio* local-spin-density calculations and reasoned in the Ni-d - Cu-d hybridization (Spišák and Hafner 2000).

Furthermore, hybridization at Ni-Cu interfaces was deduced from x-ray emission and absorption spectroscopy (XES/XAS). The empty states of thin Cu films on Ni(001) are modified and resemble the unoccupied electronic density of bulk Ni in the energy regime $\geq 3\,\mathrm{eV}$ (Karis et al. 2001). Strong hybridization at the interface between Cu and Ni in the energy regime $\geq 3\,\mathrm{eV}$ was further observed for a buried Cu monolayer in Ni, but the Cud - Ni-d hybridization is very weak (Karis et al. 2000). Moreover, resonant photoemission spectroscopy measurements show a different structure for a buried Ni layer in Cu compared to bulk Ni around $2-4\,\mathrm{eV}$ binding energy due to Ni-Cu hybridization (Jung et al. 2003).

Photoelectron angular distributions from the Fermi surface of a monolayer Ni on Cu(001) were found to be identical to those from thick Ni films and bulk Ni(001) showing a strong dispersion perpendicular to the film, and further agree with theoretical predictions for bulk Ni (Mankey et al. 1997). This bulk-like behavior in the monolayer film was attributed to the short screening length of electrons in metals, the similarity of the Ni and Cu cores, and a hybridization between Ni d bands and the Cu sp band facilitating an interaction with the underlying crystal field. The perpendicular dispersion is not expected for two-dimensional films. Moreover, similar behavior has been observed for Cu / Ni(001) and Co / Cu(001). In contrast to these findings, angle-resolved photoemission measurements proved a very different electronic structure for the monolayer and for bulk concerning Ni / Cu(001), Cu / Ni(001), Co / Cu(001), and Cu / Co(001) (Pampuch et al. 2001). Moreover, the measured binding energies support the results of local-density calculations which obtain strong narrowing of the $3d$ band width of a monolayer Ni on Cu(001) as compared to bulk Ni. An electronic structure of thin e.g. Ni films on Cu(001) different from the bulk one was further shown by the formation of discrete quantum-well

states (see section 3.5.2).

Furthermore, a mixing of Ni and Cu at the interface would reduce or suppress the film magnetism, as verified by linear muffin-tin orbital calculations (Pourovskii et al. 1999). Hence, intermixing is essentially limited to the interface and has very little effect on the magnetic moments, as shown by first-principles Green's function calculations (Lindner et al. 2000).

In summary it can be said that for thin Ni films on Cu(001) the hybridization between Ni and Cu mainly occurs in an area limited to 1 to 2 layers from the interface, resulting in an decrease of the density of $3d$ holes and of spin and orbital moments compared to bulk Ni. The electronic structure is different in thin Ni films compared to bulk Ni. Hence, there is no indication of an significantly increased density of states at the Fermi level for majority spin in thin Ni films compared to bulk Ni (see section 5.2). There are no band-structure calculations of thin fct Ni films available so far.

3.5.2 Previous measurements of quantum-well states

For Co films on Cu(001), the electronic structure below the Fermi level, investigated by spin-resolved photoemission, does not show any evidence of quantum-well states (Schneider et al. 1991, Clemens et al. 1992). However, with spin-integrated inverse photoemission, unoccupied quantum-well states above the Fermi level were detected (Ortega et al. 1993), and the dispersion of the bulk-like $3d$ states right above the Fermi level was determined (Mankey et al. 1993). Moreover, an *ab initio* calculation found spin-dependent quantum-well states and resonances with minority as well as majority spin character (van Gelderen et al. 1996). These were proved with spin-resolved inverse photoemission depending on the film thickness (Yu et al. 2003*b*). With increasing Co film thickness, the two-dimensional quantum-well states pass into the three-dimensional *sp* band. Furthermore, the calculated Co bulk band structure shows minority d holes only (Yu et al. 2003*b*).

For Cu / Co / Cu(001), the first evidence of quantum-well states in magnetic multilayers succeeded by spin-integrated inverse photoemission (Ortega and Himpsel 1992). The dispersion of the quantum-well energy with the in-plane momentum was determined (Curti et al. 1998, Danese et al. 2001). However, in this work the differentiation between bulk states and quantum-well states is not made. In addition to the quantum-well states at the belly of the Fermi surface, an extra set of quantum-well states was identified by angle-resolved photoemission at the neck of the *dog bone*-like Cu Fermi surface (Segovia et al. 1996). As a function of the electron momentum, *split* quantum-well states of both the Cu overlayer and the Co interlayer were found (Rotenberg et al. 2006). By spin-resolved photoemission, the quantum-well states in the non-magnetic Cu layer were found to be spin-polarized with minority as well as majority spin character (Carbone et al. 1993, Garrison et al. 1993, Ortega et al. 1999), what was concluded by a first-principles local density calculation as well (Nordström et al. 1995). Spin-polarized quantum-well states above the Fermi level in both the Cu film on top and the underlying Co film were found by spin-resolved inverse photoemission (Yu and Donath 2003*a*). The quantum-well states in the Cu film, with both majority as well as minority spin components, develop

into a surface resonance as a function of the electron momentum. In comparison with Curti et al. (1998) and Danese et al. (2001), the spin-polarization enables an unambiguous differentiation between quantum-well states in contrast to bulk-like and surface-derived states.

For Ni films on Cu(001), spin-integrated photoemission studies investigated the dependence of the electronic structure on the Ni film thickness below the Fermi level, but only contributions from the d bands are discussed (Pampuch et al. 2001). Spin-integrated inverse photoemission dealt with Ni films on Cu(001) and Ni / Cu / Ni (Himpsel and Rader 1995, Hwang and Himpsel 1995) and Cu / Ni / Cu (Danese et al. 2004*a*) trilayer structures. The main interest has been in the electronic states of the Cu layer. For Ni films on Cu(001), discrete quantum-well states were identified showing the typical shift to higher energy with increasing Ni film thickness, but no spin resolution was used and no dispersion was measured (Himpsel and Rader 1995).

Spin-integrated inverse photoemission measurements have been performed on Cu films on Ni(001) (Himpsel and Rader 1995, Hwang and Himpsel 1995) and on Cu films on thin Ni films on Cu(001) (Danese et al. 2004*a*). In the latter case, it is reported about an *anomalous thickness dispersion* of the unoccupied quantum-well states in Cu films on Ni. With this, a shift down in energy with increasing Cu film thickness is meant. But the identification of the spectral features is not stringent. Moreover, in the same study the occupied energy levels of the Cu overlayer display the usual upward shift with increasing overlayer thickness. The origin of the *anomalous* energy shift is believed to be tied to an interaction of the Cu and Ni *sp* levels at the overlayer-film interface. Moreover, spin-integrated photoemission studies on Ni/Cu multilayers observed a resonant interaction between two Cu quantum-well states in this double quantum-well structure (Wu et al. 2006). But all in all, there is no data available about the spin character of quantum-well states in thin Ni films.

Chapter 4

Experiment

In this chapter, the main experimental method of the present work, the spin- and angle-resolved inverse photoemission, is introduced. Furthermore, the preparation and characterization of the investigated Ni and Co ultrathin films on Cu(001) and of Cu on Ni / Cu(001) and on Co / Cu(001) is described. Finally, the experimental set-up is presented.

4.1 Spin-resolved inverse photoemission

Angle-resolved photoemission (PE) (Kevan 1992, Hüfner 1996, Johnson 1997, Osterwalder 2006) and inverse photoemission (IPE) (Dose 1983, Dose 1985, Borstel and Thörner 1988, Smith 1988, Himpsel 1990, Donath 1994) are two complementary experimental methods to investigate the electronic structure of crystalline solids. In PE, photons impinge on a sample and the emitted electrons are detected. In IPE, the reverse case takes place. As shown in figure 4.1, electrons impinge on the sample and the emitted photons are detected. While PE is sensitive to the occupied electronic states below the Fermi level and the unoccupied states above the vacuum level, IPE can detect unoccupied states above the Fermi level. In the present work, spin- and angle-resolved inverse photoemission is used to investigate the unoccupied electronic states of magnetic ultrathin films and layered structures. Theoretical and experimental aspects of this technique are outlined in the next two sections.

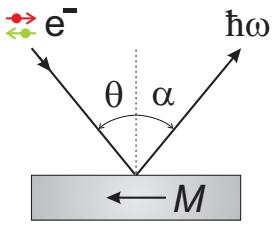

Figure 4.1: In spin- and angle-resolved inverse photoemission spin-polarized electrons impinge on a magnetic sample $\boldsymbol{M}$ at the angle of incidence θ, and the emitted photons $h\nu$ are detected at the angle α.

4.1.1 Theoretical aspects

The inverse photoemission experiment can be traced back to the discovery of the X-rays by Wilhelm Conrad Röntgen in 1895 (Röntgen 1895). For this, he was to receive the first-ever Nobel Prize in physics in 1901. Röntgen noticed that the tubes by Philipp Lenard (Lenard 1900) produce a new kind of radiation, which he called X-rays. These consist of two parts, the *Bremsstrahlung*, which arises from high energy electrons slowing down in matter, as well as the characteristic X-rays, which result from radiative transitions. The IPE process is the time-reversed photoelectric effect, that is to say the emission of electrons from a solid due to photon absorption (Hertz 1887, Einstein 1905). In IPE, incident electrons may undergo radiative transitions in a solid, what may lead to the emission of electromagnetic radiation. The theoretical description on an atomic scale succeeded not before the development of the atomic models and quantum mechanics in the 1910s and 1920s as well as of solid state physics in the second half of the 20th century.

In a solid, where the energy levels of the electrons are described by band theory (Ashcroft and Mermin 1976), an electron may absorb the energy of an incoming photon and occupy an electronic state of higher energy. In the reverse case, an electron may decay from a state of higher energy into an unoccupied state of lower energy, thereby emitting a photon. In IPE, an incoming electron is injected into an empty state of higher energy above the vacuum level. The electron may undergo a radiative transition into an empty state of lower energy and a photon is emitted.

For the description of the IPE process, the limitation to a unit cell is sufficient due to the periodicity of the solid. In reciprocal space, the unit cell corresponds to the first Brillouin zone. The energy E can then be described as a function of the electron momentum or reciprocal lattice vector $\boldsymbol{k}$, respectively, in the reduced zone scheme. One refers to this dependence as energy-momentum relation or dispersion $E(\boldsymbol{k})$.

For the present, an incoming electron occupies an unoccupied initial state $|i\rangle$ above the vacuum level E_V with energy E_i, momentum $\hbar\boldsymbol{k}_i$ ($\hbar$ = Planck's constant / 2π), and electron spin σ_i. Afterwards the electron decays into a final state $|f\rangle$ above the Fermi level E_F with lower energy E_f, momentum $\hbar\boldsymbol{k}_f$, and spin σ_f, whereby a photon with energy $\hbar\omega$ and wave vector $\boldsymbol{q}$ is emitted. This can only occur under adherence to the conservation laws for energy, momentum, and spin:

$$\begin{aligned} E_i &= E_f + \hbar\omega \\ \boldsymbol{k}_i &= \boldsymbol{k}_f + \boldsymbol{G}_{hkl} + \boldsymbol{q} \\ \sigma_i &= \sigma_f . \end{aligned} \tag{4.1}$$

For radiative transitions in the ultraviolet regime ($\hbar\omega \approx 10\,\mathrm{eV}$), the norm of $\boldsymbol{q}$ is negligible compared to the expansion of the Brillouin zone. Accordingly, the angle of photon emission does not influence the kinematics of the experiment. The reciprocal lattice vector $\boldsymbol{G}_{hkl}$ represents the momentum transfer to the lattice of the solid and is already included in the reduced zone scheme. This results in a perpendicular direct transition with momentum conservation as follows:

$$\boldsymbol{k}_i = \boldsymbol{k}_f . \tag{4.2}$$

A schematic diagram for spin-resolved inverse photoemission is presented in figure 4.2. The energy E is shown as a function of the momentum $\boldsymbol{k}$ in the reduced zone scheme. The partly unoccupied spin-split energy bands are typical for a ferromagnetic material. The magnetic moment results from the different number of majority spin ($\uparrow$) and minority spin ($\downarrow$) electrons. Vertical arrows indicate spin-conserved direct radiative transitions from initial states $E_{i,\uparrow\downarrow}$ above the vacuum level E_V into unoccupied final states $E_{f,\uparrow\downarrow}$ above the Fermi level E_F. The dotted curve indicates the final state energies of detectable transitions with fixed photon energy (see section 4.1.2). In the present case, only one transition into an empty minority band at energy $E_{f,\downarrow}$ can be detected. A corresponding schematic spin-dependent IPE spectrum is shown at the right-hand side of figure 4.2. The energy of the final states is on the ordinate and the quantum count rate of the detected photons is on the abscissa. A peak appears for minority electrons at $E_{f,\downarrow}$ only. As the majority band is completely below the Fermi level and therefore occupied, no transition into this band is possible. Hence, the spectrum for majority electron spin shows a background only.

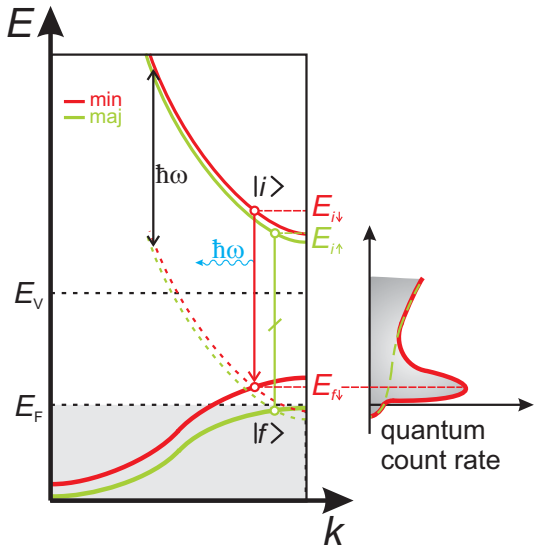

Figure 4.2: Schematic diagram illustrating the spin-resolved inverse photoemission measurement. The energy E is shown as a function of the momentum $\boldsymbol{k}$. See text for details.

The difference in energy between the minority and majority spin band is denoted as exchange splitting:

$$\Delta E_\mathrm{ex}(\boldsymbol{k}) = E_\downarrow(\boldsymbol{k}) - E_\uparrow(\boldsymbol{k}). \tag{4.3}$$

The experimentally observed spin splitting does not necessarily represent the real exchange splitting of the final band. It is rather a result of the exchange splittings $\Delta E_\mathrm{ex}(\boldsymbol{k})$ and of the dispersions $E(\boldsymbol{k}_\perp)$ of the initial as well as of the final bands. For a given transition energy $\hbar\omega$, the measured transitions may appear at slightly different $\boldsymbol{k}$ for majority and minority electrons. This may lead to different final state energies for majority and minority electrons, thus affecting the exchange splitting. The determination of the spin splitting is neither limited by the intrinsic linewidth

nor by the experimental energy resolution, because the spectra for majority and minority spin are measured separately.

In the IPE experiment energy, momentum, and spin of the initial state are defined and the emitted photon is detected. Energy, momentum, and spin of the final state are determined by the conservation laws 4.1 and 4.2.

Discussing the consequences of the conversation laws, there are differences between the components of the momentum parallel and perpendicular to the surface of the solid. Due to the influence of the crystal potential, the perpendicular momentum $\boldsymbol{k}_\perp$ of the electron, which is coupled to the solid in the initial state (i), is larger than the one of the electron that has been free in the vacuum (vac) before:

$$|\boldsymbol{k}_{i,\perp}| > |\boldsymbol{k}_{vac,\perp}|. \tag{4.4}$$

Therefore, the perpendicular momentum of the final state cannot directly be determined in contrast to the parallel momentum in the plane of the surface. However, because of the periodicity of the lattice the parallel momentum $\boldsymbol{k}_\parallel$ is conserved except for a reciprocal lattice vector $\boldsymbol{G}_{hkl,\parallel}$ (Kane 1964):

$$\boldsymbol{k}_{i,\parallel} + \boldsymbol{G}_{hkl,\parallel} = \boldsymbol{k}_{vac,\parallel}. \tag{4.5}$$

In addition, the following limitation applies for the reciprocal lattice vector due to energy conservation:

$$|\boldsymbol{k}_{i,\parallel} + \boldsymbol{G}_{hkl,\parallel}| \leq |\boldsymbol{k}_{vac}|. \tag{4.6}$$

At pure surfaces, which are not covered by a film of adsorbates having a different reciprocal surface lattice vector than the surface itself, so-called surface *Umklapp* processes with $\boldsymbol{G}_{hkl,\parallel} \neq 0$ are strongly restricted. In this case, the electrons are scattered only in the plane given by their direction of incidence and the surface normal.

According to equations 4.4 and 4.5, only the parallel momentum of the initial state can be determined by dint of the experimental parameters, namely by the choice of the kinetic energy of the initial state $\boldsymbol{E}_{kin,i}$ and of the angle of incidence θ between the direction of incidence of the electrons and the surface normal:

$$|\boldsymbol{k}_{i,\parallel}| = |\boldsymbol{k}_{vac,\parallel}| = \frac{1}{\hbar}\sqrt{2m_e E_{kin,i}}\,\sin\theta. \tag{4.7}$$

Hence, a mapping of the unoccupied band structure is possible. The measurement of the energy of the emitted photons for different angles of incidence results in the dispersion: the energy of the final states E_f as a function of parallel momentum $\boldsymbol{k}_{f,\parallel}$ and spin σ_f.

In the IPE spectra, the measured distribution of sharp peaks originating from direct transitions is superimposed by a featureless background due to non-radiating energy-loss processes like electron-hole pair generation and electron-phonon interaction (Dose and Reusing 1980). These energy-loss processes may lead to some radiative transitions resulting in a spin-dependent background in the spectra without

structural features that monotonously increases with increasing energy. In contrast to this, direct transitions cause clear structural features in the spectra.

To simplify the discussion of the spectra and the calculation of the band structure, respectively, the IPE experiment is often performed at normal electron incidence or using initial states that have even parity with respect to a mirror plane. This results in a higher symmetry by which bands may be degenerated several times, reducing the number of possible transitions. Moreover, measuring in a mirror plane gives information about the symmetry of the final state through the spectral intensities by means of the dipole matrices (Goldmann 1982).

The intensity of a transition is determined by the selection rules, namely by the possibility that an incoming electron occupies the initial state and afterwards decays into the final state. The possibility of occupation is large if the wave function of the incident electron is similar to the one of the initial state. According to Fermi's Golden Law, the transition possibility into the final state is proportional to the square of the transition matrix element (Plummer and Eberhardt 1982).

The information depth of IPE is determined by the electron inelastic mean-free path in the solid. The *universal curve* describes the electron attenuation length as a function of the kinetic electron energy (Powell 1988). It has a minimum of $\sim 5\,\text{Å}$ length at 50 eV energy and increases for higher as well as for lower energies. However, the information depth for low-energy electrons in ferromagnetic $3d$ metals is somewhat lower and amounts from to two to three layers only (Donath 1994). Hence, IPE is a very surface-sensitive technique, suitable especially for surface and thin-film studies.

Concerning theoretical models for the IPE process, in former models IPE has been described as a three-step process consisting of the absorption of the electron by the solid, the propagation through the solid and the radiative transition (Berglund and Spicer 1964). Furthermore, a one-step model describes IPE as a coherent quantum-mechanical process (Pendry 1976, Pendry 1980, Borstel and Thörner 1988, Braun and Donath 2004).

4.1.2 Experimental aspects

An inverse photoemission set-up consists of an electron source, a sample of interest, and a photon detector. A schema of the IPE set-up used in the present work is shown in figure 4.3. Circular polarized light impinges on a GaAs photocathode, which is prepared with Cs and O_2. The resulting electron beam is turned by an electrostatic bender by 90° producing a beam with transversal polarization $\boldsymbol{P}$. The polarized electrons impinge with the velocity $\boldsymbol{v}$ and the energy $E_{kin,i}$ onto the sample, and the emitted photons are detected by Geiger-Müller counters. The electron source, the photon detectors, the sample requirements, and the realization of the measurement are described in this section.

Electron source

For spin-dependent measurements, spin-polarized electrons are required. A common method to produce spin-polarized electrons is by incidence of circular polarized light

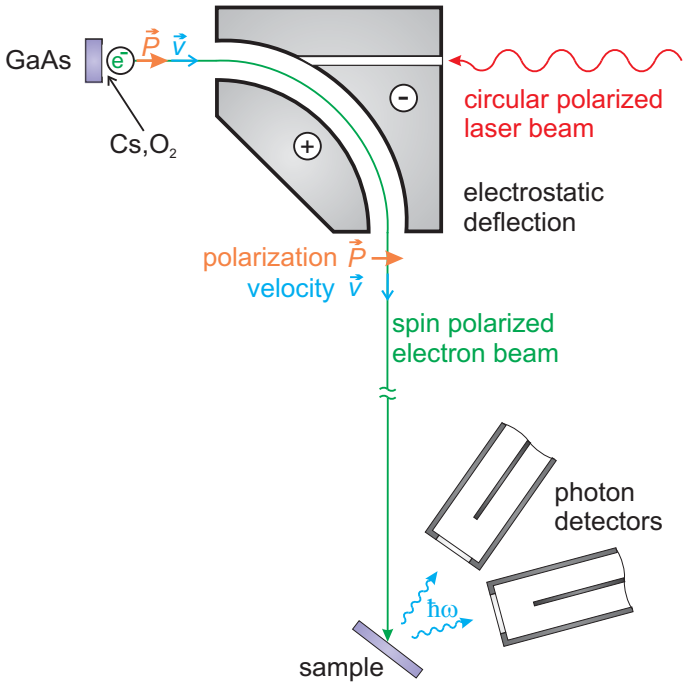

Figure 4.3: Experimental set-up for spin- and angle-resolved inverse photoemission showing the GaAs electron source, the electrostatic bender, the sample, and the photon detectors.

onto a GaAs(001) crystal (Pierce and Meier 1976). In this case, the selection rules for transitions from the valence-band maximum split by spin-orbit coupling into the conduction-band minimum result in an imbalance of majority and minority electrons. Negative electron affinity is achieved by adsorption of Cs and O_2, that lowers the work function. In the used spin-resolved inverse photoemission set-up (Kolac et al. 1988), circular polarized light is generated by a 832 nm single-mode GaAlAs laser and a liquid crystal retarder. The GaAs photocathode emits a beam of low-energy electrons ($7 - 15$ eV) with defined energy, momentum, and spin. The electron beam has a divergence of below 2° and a diameter of (3.00 ± 0.25) mm on the sample surface. The width of the energy distribution is below 300 meV for electron currents of $\sim 5\,\mu$A. The electron spin polarization amounts to (33 ± 3) % (Donath et al. 1990). The direction of spin polarization is perpendicular to the propagation direction of the electron beam and, at normal incidence, parallel to the magnetization direction of a remanently in-plane magnetized sample.

Photon detection

After impinging on the sample, the electrons may decay via radiative transitions into lower-lying unoccupied states. Concerning the detection of the photons, there are two possibilities, namely the spectroscopic analysis of the emitted radiation by means of a monochromator in combination with a photomultiplier using a fixed primary electron energy (*Bremsstrahlung* spectroscopy) (Ulmer 1959) and the detection at a fixed photon energy by means of an energy-selective Geiger-Müller counter while varying the electron energy (isochromate mode) (Dose 1977).

Using a monochromator makes the spectral analysis of the emitted radiation at fixed energy of the electrons possible. A tunable photon energy allows the determination of cross-section variations. By use of an grating UV-monochromator, the detectable energy of the photons ranges between 10 eV and 40 eV (Fauster et al. 1983, Fauster and Himpsel 1983). Furthermore, also the detection at fixed energy is possible, e.g. by use of an X-ray monochromator (1486.6 eV) (Lang and Baer 1979). The advantage of a monochromator is the better resolution, whereas the disadvantage is the loss of transmission conditional on the diffraction procedure. As a consequence, the required electron current is in the order of $\sim 1\,\mathrm{mA}$. In practice, these high currents cannot be realized with a GaAs electron source for spin-polarized electrons.

Using a Geiger-Müller counter, only photons with a fixed energy can be detected. Different final states are accessible by occupation of different initial states. At a fixed incidence angle, this can be attained by varying the kinetic energy of the incident electrons, which is determined by the potential between electron emitter and sample. Possible parameters are the incidence angle of the electrons, the emission angle of the photons, and the electron spin. An advantage of this method are the sufficient electron currents in the order of $\sim 1 - 10\,\mu\mathrm{A}$ (Denninger et al. 1979) due to the higher sensitivity compared with using a monochromator. Such currents are easy to produce with a GaAs electron source.

The spectral width of the peaks in the IPE spectra results from the superposition of the intrinsic linewidth of the observed feature and the experimental energy resolution of the apparatus function. The latter consists of two parts, namely the optical resolution of the photon detector as well as the energy distribution of the incident electrons. The energy-selective Geiger-Müller-counter serves as a band-pass filter (Dose 1977). The band-pass is limited to lower energies by the ionization probability of the filling gas and to higher energies by the transmission cut-off of the entrance window. With iodine as a filling gas, having a threshold for photoionization of 9.23 eV (Dibeler et al. 1971), and with CaF_2 as an entrance window, having a transmission cut-off of 10.33 eV (Heath and Sacher 1966), the detection energy at room temperature amounts to $\hbar\omega = (9.6 \pm 0.4)\,\mathrm{eV}$ (Dose 1977). The use of SrF_2 as an entrance window with a lower transmission cut-off of 9.69 eV (Samson 1967) improves the energy resolution and shifts the mean detection energy to $\hbar\omega = (9.4 \pm 0.2)\,\mathrm{eV}$ (Dose et al. 1986). Heating the SrF_2 window to the optimum temperature of 80 °C further improves the energy resolution to $\hbar\omega = (9.3 \pm 0.15)\,\mathrm{eV}$ (Schneider 1985, Math 2001, Braun et al. 2002). Otherwise, the sensitivity, which is proportional to the area of the optical band-pass, decreases by a factor of 4 to 5, resulting in an increased measuring time.

Sample requirements

Special experimental requirements have to be fulfilled for the realization of angle- and spin-resolved IPE measurements. The angle between the polarization direction of the electron spin and the magnetization direction of the sample have to be known for the analysis of magnetic properties of the sample. This requires an exact knowledge of the magnetization of the sample. Furthermore, for angle-resolved measurements of especially bulk-like samples, magnetic stray fields have to be avoided as much as possible not to disturb the spin-polarized low-energy electrons. For this purpose,

the magnetization has to be in the plane of the sample surface. Besides, the use of frame-shaped samples as well as a magnetization of the sample by means of U-shaped magnets, producing closed lines of magnetic flux, support a reduction of stray fields. For low-dimensional systems, stray fields are negligibly small. But the remanent magnetization of the sample is experimentally limited by the magnetic anisotropy. For the observation of surface states, the surface of the sample has to be as free of adsorbates as possible on the time scale of the experiment. Hence, the sample has to stay in an ultra-high vacuum apparatus (see section 4.3).

Measurement

In the experiment the kinetic energy of the electrons is varied by changing the potential between the GaAs crystal and the sample. At every set energy, the photon counts are measured for both spin directions until a given amount of charge is reached. The measurement time depends on the desired statistics. It is influenced by the energy range, the energy step width, the current of incident electrons, the charge, and the sample. With $2\,\mu$A electron current, the measurement time for a single spin-resolved spectrum with 60 data points typically amounts to about 20 to 30 minutes. The count rate depends on the electron current, on the electron energy, and on the sample, and typically is between 10 Hz and 200 Hz. To obtain a sufficient statistics, which means a satisfactory small scatter of the data points, several equivalent spectra have to be accumulated.

The IPE spectra represent the photon intensities as a function of the kinetic energy and the spin of the incident electrons. As the spin polarization of the electrons only amounts to $P = 33\,\%$, the spectra are normalized to hypothetical 100 % spin polarization. To obtain similar statistics compared to the non-normalized data, the measurement time has to be increased by a factor of ~ 10.

The effective spin polarization P_{eff} results from the projection of the spin polarization $\boldsymbol{P}$ onto the magnetization direction $\boldsymbol{M}/|\boldsymbol{M}|$:

$$P_{eff} = \boldsymbol{P} \cdot \frac{\boldsymbol{M}}{|\boldsymbol{M}|}. \tag{4.8}$$

The measured counts $n_\uparrow$ for majority spin and $n_\downarrow$ for minority spin are obtained for the respective spin polarization directions for $P = 33\,\%$. The corresponding counts for hypothetical 100 % spin polarization are $N_\uparrow$ and $N_\downarrow$, respectively. The spin asymmetry A is given by

$$A = \frac{N_\uparrow - N_\downarrow}{N_\uparrow + N_\downarrow} = \frac{n_\uparrow - n_\downarrow}{n_\uparrow + n_\downarrow} \cdot \frac{1}{P_{eff}}. \tag{4.9}$$

With the spin-integrated counts $N = N_\uparrow + N_\downarrow = n_\uparrow + n_\downarrow$, the counts for hypothetical 100 % spin polarization are given by

$$N_{\uparrow,\downarrow} = \frac{N}{2} \cdot (1 \pm A). \tag{4.10}$$

By changing energy, spin and incidence angle of the electrons, the electron states above the Fermi level can be probed with both spin and momentum resolution.

Further methods

In addition to inverse photoemission, the unoccupied states are further detectable by two-photon photoemission (Giesen et al. 1985, Haight 1995). In this case, two photons are used to remove the electron from the solid. The first photon by a pumping laser pulse may excite the electron to an unoccupied state below the vacuum level. If the lifetime of this state is not too short, another photon by a probing laser pulse may excite it to a final state above the vacuum level, and the electron can be detected by an energy analyzer. Thus, this technique provides information about occupied as well as about unoccupied states. It can be performed in two modes: At a fixed delay of the two laser pulses providing energy resolution as well as at a fixed energy providing time resolution. With a spin-polarization detector, additional spin-resolution is achieved (Schmidt et al. 2005). Compared with inverse photoemission, on the one hand the energy resolution is superior ($\approx 10\,\mathrm{meV}$), the measurement time is much shorter, and time resolution is available. On the other hand, it suffers from the relatively low energies and momentum vectors that can be reached and is thus unable to probe the whole Brillouin zone.

Furthermore, the local occupied as well as unoccupied electronic states can be approached by current imaging tunneling spectroscopy (Hamers et al. 1986, Hamers 1992) measuring the current-voltage characteristics with a scanning tunneling microscope (Binnig et al. 1982, Binnig et al. 1983). In this case, the tip is maintained in a fixed position with respect to the surface. On the one hand, this technique provides spatial resolution. On the other hand, the momentum resolution has to be given up. Thus, no band-mapping is possible. Using a magnetic tip, the scanning tunneling spectroscopy can also be performed with spin resolution (Bode 2003).

4.2 Sample preparation and characterization

In this section, the experimental procedure of preparing thin Ni, Co, and Cu films on a Cu(001) substrate is described.

4.2.1 The Cu(001) substrate

The Cu(001) single crystal used in the present study is 8 mm in diameter and 2 mm thick. It is polished mechanically and chemo-mechanically by the manufacturer (MaTeck) with an accuracy of 0.2°. Under ultra-high vacuum conditions, the surface is cleaned with a standard procedure of ion sputtering (Ar^+, 600 eV) and subsequent annealing by electron bombardement (800 K) (Bahr et al. 1987). Sputtering removes deposited films and extracts impurity layers and clusters. Annealing the surface recovers the thermodynamically stable surface structure by mobilizing the surface atoms.

Low-energy electron diffraction (LEED) is used to check the surface structure and quality (Zangwill 1988, Ertl and Küppers 1985). In this method, monochromatic electrons are accelerated onto the sample. The elastic backscattered electrons are collected by a fluorescent screen. This gives an image of the Bragg diffraction spots

reflecting the crystal structure in reciprocal space. Sharp patterns indicate a clean and flat surface.

The chemical composition of the surface is checked by Auger electron spectroscopy (AES) (Auger 1925, Davis et al. 1976, Ertl and Küppers 1985). This technique probes the element-specific electronic core states of a solid. Especially, the contamination of the sample with adsorbates is examined.

Finally, the IPE intensity of the respective spectral features resulting from the electronic structure of the substrate prove the quality of the substrate surface. Especially, the Cu image-potential induced surface state requires a good surface quality.

4.2.2 Preparation of Ni, Co, and Cu films

The Ni, Co, and Cu films are grown on the Cu(001) substrate by molecular beam epitaxy ((Cho 1971, Joyce 1985)) through electron beam evaporators. Here, a rod of 2 mm diameter or a crucible, filled with the respective pure material, is heated by an electron beam. The evaporated particles move towards the sample. The sample is at room temperature or cooled down to 100 K for better film growth. After film deposition, most samples are post-annealed to about 450 K to improve the film quality (see chapter 3).

The electron beam evaporators are calibrated by AES. The AES spectra are measured as a function of deposition time t. With I_s the spectrum of the pure substrate and I_f the spectrum of a thick deposited film, the parameter a is determined by fitting a calculated spectrum $I = a \cdot I_\mathrm{s} + (1-a) \cdot I_\mathrm{f}$ to each of the measured spectra. For layer-by-layer growth, the graph $a(t)$ shows kinks when an integer number of layers is obtained (von der Linden et al. 1998). Typical growth rates used in the present work are 0.5 layers per minute. As an example, a typical graph $a(t)$ for the calibration of the Ni evaporator is shown in figure 4.4 with Ni as film f and Cu as substrate s. For this, the high-energy peaks $E_{Ni} = 848\,\mathrm{eV}$ and $E_{Cu} = 920\,\mathrm{eV}$ were used. An alternative method is to plot the peak-to-peak ratio $I_{Cu}(920\,\mathrm{eV})/I_{Ni}(848\,\mathrm{eV})$ as a function of time, which results in the same deposition rate. Figure 4.4 shows $a(t)$ for the calibration of the Cu evaporator on 15 ML Co / Cu(001). In this case, the low-energy peaks $E_{Cu} = 60\,\mathrm{eV}$ and $E_{Co} = 53\,\mathrm{eV}$ have been used.

The film quality is proved by the same means as described for the Cu(001) substrate (see section 4.2.1): AES probing the chemical composition, sharp LEED patterns probing the structure of the films, and, moreover, the IPE intensity of the respective spectral features.

Figure 4.6 shows LEED pictures of the Cu(001) substrate as well as of 1, 2, 5, 8, 12 and 20 ML Ni on Cu(001) taken at a energy of $E = 154\,\mathrm{eV}$. All spectra show the fourfold symmetry of the fcc crystal structure. The position and the intensity of the LEED spots does hardly change with increasing Ni film thickness showing that the structure remains the same. The sharp spots and a low background indicate a good crystal quality. The different intensity of the four spots, especially the brighter one of the left spot, is due to the experimental set-up.

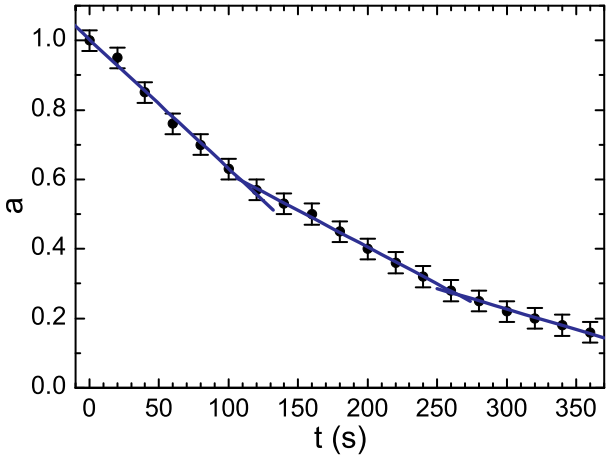

Figure 4.4: Typical graph $a(t)$ (see text) for the calibration of the Ni evaporator. Kinks in the gradient indicate a deposition rate of 1 ML in 120 s.

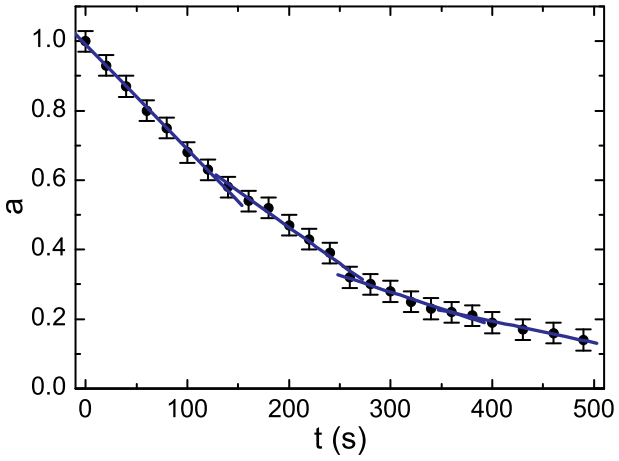

Figure 4.5: Typical graph $a(t)$ for the calibration of the Cu evaporator on 15 ML Co / Cu(001). The deposition time amounts to about 1 ML in 120 s.

4.3 Experimental set-up

The vacuum apparatus is described in detail in Math (2001). It consists of three chambers: The electron source chamber containing the GaAs photocathode, the main chamber containing the sample, and a third chamber containing an electron spin polarization detector. All chambers are separated by gate valves and can be pumped independently by ion-getter pumps and titanium-sublimation pumps. In addition, a membrane pump combined with a turbomolecular pump can assist pumping after an bake-out of the vacuum apparatus ($< 180\,^{\circ}\mathrm{C}$) or after a gas inlet e.g.

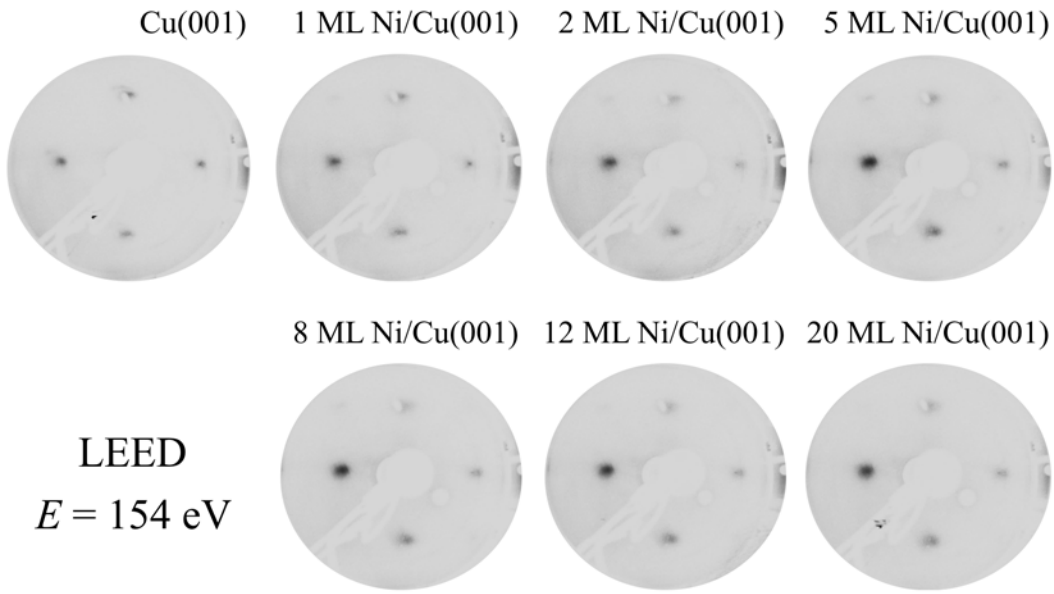

Figure 4.6: LEED pictures of n ML Ni on Cu(001), $0 \leq n \leq 20$, taken at an energy of 154 eV.

for sputtering. The base pressure amounts to below $1 \cdot 10^{-10}$ mbar.

The source chamber contains the GaAs crystal to produce the spin-polarized electrons. The electrostatic bender inside the chamber deflects the electron beam by 90° resulting in a beam with transversal spin polarization. An electron optic transfers the spin-polarized electrons to the main chamber (Kolac et al. 1988).

The substrate in the main chamber is mounted at a rotatable xyz-manipulator. It can be heated by a tungsten filament and can be cooled by nitrogen. The temperature is measured by a W(3 %)Re/W(25 %)Re thermocouple. Its accuracy amounts to ±5%. The manipulator also holds a Faraday cup to measure the profile of the electron beam.

The main chamber is divided into three planes. In the central plane, there are the entry of the electron source as well as two Geiger-Müller counters at angles of 35° and 70° with respect to the incident electron beam, respectively. Both counters have a SrF_2 entrance window, but only the one of the 70° counter can be heated.

Moreover, this plane contains an electron gun for the stimulation of secondary electrons and the electron spin detector. Secondary electrons from magnetic samples are spin-polarized (Chrobok and Hofman 1976). Thus, magnetometry with spin-polarized secondary electron emission (SPSEE) can be performed to determine magnetic order (Bland and Heinrich 1994). The spin-polarization of the emitted electrons is proportional to the sample magnetization (Siegmann 1994). The sample can be magnetized with a magnetic coil situated next to the sample in the middle of the chamber. For the detection of electron spin polarization (Kessler 1985), two types of detectors are available: a spin-polarized low energy electron diffraction (SPLEED) detector (Kirschner and Feder 1979, Yu et al. 2007) or a Mott-type detector (Gray et al. 1983, Dunning et al. 1987, Qiao et al. 1997, Zumbrägel 2007).

The lower plane contains an additional magnetic coil, which is usually used for

magneto-optic Kerr effect (MOKE). This coil can also be used to magnetize the sample before the IPE measurements.

In the upper plane, there is the equipment for preparing and characterizing the sample. The sample can be sputtered by an ion gun. Thin films can be deposited by MBE through three electron beam evaporators. The sample can be structurally characterized by LEED and chemically by AES. For this, a four-grid electron optic is mounted. For AES, an additional electron gun for grazing electron incidence is available to improve the surface sensitivity. Furthermore, a quadrupole mass spectrometer is used for residual gas analysis.

To reduce the influence of external magnetic fields on the low-energy electrons, a compensation against disturbing fields (e.g. caused by elevators, the earth's magnetic field) by three pairs of Helmholtz coils is possible. Furthermore, the vessels are lined with Conetic, a magnetic soft material shielding remaining stray fields.

Chapter 5

Ni on Cu(001)

Ultrathin Ni films on Cu(001) represent one of the most studied magnetic thin-film systems (Baberschke 1996, Baberschke 2001). They show unique magnetic properties such as unusual spin-reorientation transitions. With increasing film thickness, the magnetization changes from an in-plane to an out-of-plane orientation and back to an in-plane one (see section 3.2). Only a few spin-integrated photoemission studies have already investigated the electronic structure for Ni films on Cu (Pampuch et al. 2001) and Ni/Cu multilayers (Wu et al. 2006) (also see section 3.5). Previous work with spin-integrated inverse photoemission dealt with Ni films on Cu(001) and Ni/Cu/Ni (Himpsel and Rader 1995, Hwang and Himpsel 1995) and Cu/Ni/Cu (Danese et al. 2004*a*) trilayer structures. So far, the main interest has been in the electronic states of the Cu layer. For Ni films on Cu(001), discrete quantum-well states were identified at normal electron incidence, but no spin resolution was used and no dispersion was measured (Himpsel and Rader 1995).

In this chapter, first the experimental features that appear in the inverse photoemission spectra of ultrathin Ni films on Cu(001) are introduced, especially the spin-polarized quantum-well states. Their exchange splitting is determined. Next, the reduced asymmetry of the bulk-like Ni feature just above the Fermi level is discussed. Furthermore, the dependence of the features on the Ni film thickness is described in detail. Finally, the energy vs. momentum relation in thin Ni films on Cu(001) is studied.

5.1 Electronic states of Ni films on Cu(001)

5.1.1 Ni on Cu(001) compared to Co on Cu(001)

To begin with, the electronic states which may appear in the IPE spectra for thin Ni films are introduced and compared with the spectra of the Cu(001) substrate and of a thick Ni film. Figure 5.1 shows IPE spectra at normal electron incidence of the Cu(001) substrate and of 6 ML, 10 ML, and 100 ML thick Ni films on Cu(001). As in all shown IPE spectra, the data sets for minority and majority electron spin are represented by open red and filled green circles, respectively. The experimental statistical error is smaller than the size of the data symbols.

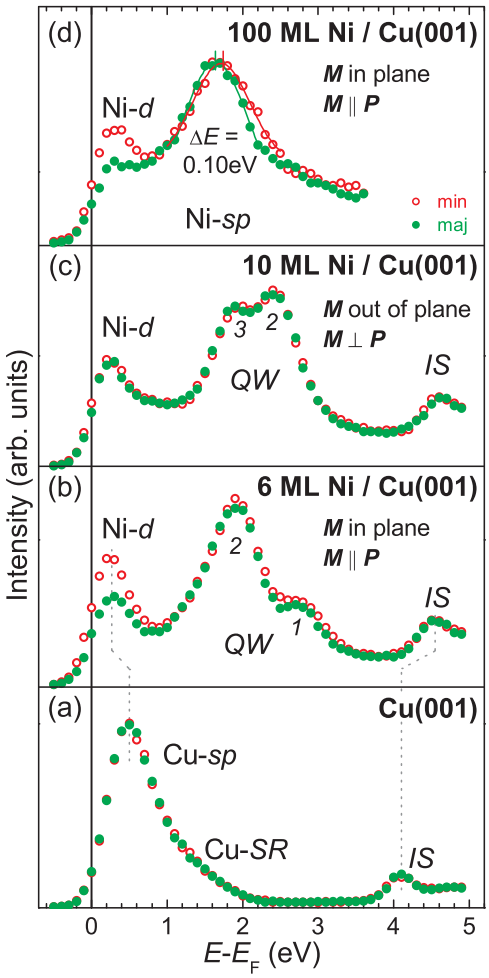

Figure 5.1: Spin-resolved inverse photoemission spectra at normal electron incidence of (a) the Cu(001) substrate and of (b) 6 ML Ni, (c) 10 ML Ni, and (d) 100 ML Ni on Cu(001). Data for minority and majority spin are presented by open red and filled green circles, respectively.

For the non-ferromagnetic Cu(001) substrate, no spin asymmetry is observed within the experimental statistical error (figure 5.1 (a)). The spectrum exhibits three features, which are well-known for Cu(001) (Graß et al. 1993). A bulk-like transition between *sp* states of Cu, marked with Cu-*sp*, appears at 0.5 eV above the Fermi level. At the high-energy side of the Cu-*sp* transition, a crystal-induced surface resonance, Cu-*SR*, shows up as a shoulder of the Cu-*sp* feature. The $n = 1$ image-potential-induced surface state (*IS*) appears at 4.15 eV. Its spectral intensity proves good surface quality.

With 6 ML ferromagnetic Ni on top of the Cu(001) substrate, the spectra change remarkably (figure 5.1 (b)). For this thickness, the magnetization $\boldsymbol{M}$ lies in the film plane and is either parallel or anti-parallel to the spin-polarization direction $\boldsymbol{P}$ of the incoming electrons at normal incidence (see section 3.2). As expected,

differences between the two spin channels can clearly be detected. The spectral feature just above the Fermi level results from indirect non-$\boldsymbol{k}$-conserving transitions into empty d states and is denoted as Ni-d. Direct transitions into empty d states are not possible in Ni along (001) for reasons of energy conservation as well as selection rules. The Ni-d feature appears at 0.25 eV. Thus, it is 0.25 eV lower in energy than the Cu-sp feature as indicated by the dotted gray line. According to the bulk band structure of Ni, the d holes exclusively have minority character (Eckardt and Fritsche 1987)(see section 2.2.1). However, the experiment shows that the Ni-d feature appears in both the minority and the majority channels, even though with a clear surplus for minority spin. The Ni-d feature is discussed in detail in section 5.2. Two more features can be observed in the spectra. They appear between the top of the sp band of the Cu band structure at 1.8 eV and the top of the sp bands of the spin-dependent Ni band structure at 2.74 eV for majority spin and at 2.78 eV for minority spin. In this energy range, complete electron confinement within the Ni film is expected (see section 2.2.1). Thus, these states can be identified as the first and second quantum-well state, denoted as *QW-1* and *QW-2*, respectively. The data are in accordance with the spin-integrated data of Himpsel and Rader (1995), except for obvious differences in the thickness calibration by a factor of about 1.6. The thickness calibration obtained for the present study is consistent with the thickness-dependent spin-reorientation transitions and was confirmed by AES (see section 4.2.2). The exchange splitting of the quantum-well states will be discussed further below (see section 5.1.2). The high spectral intensity of the image-potential-induced surface state *IS* at 4.6 eV proves good surface quality of the Ni film. The change in energy from Cu to Ni amounts to about 0.45 eV and is indicated by the dotted gray line.

The spectra for 10 ML Ni on Cu(001) are shown in figure 5.1 (c). At this film thickness, the magnetization of the film is oriented perpendicular to the film plane and thus perpendicular to the spin polarization of the incoming electrons. Consequently, no spin asymmetry is detectable within the experimental statistical error. As quantum-well states shift to higher energies with increasing film thickness (see section 5.3), the second and third quantum-well state, *QW-2* and *QW-3*, appear.

For 100 ML Ni on Cu(001), as shown in figure 5.1 (d), the magnetization is rotated back into the film plane. This is clearly reflected in the significant spin asymmetry observed for the Ni-d feature. In contrast to the 6 ML Ni film, the Ni-d feature exclusively appears in the minority spin channel: There is no majority contribution besides the background intensity. For this thickness, the quantum-well states have disappeared in favor of the well-known bulk transition between sp-like bands. The spin splitting amounts to 0.10 eV in accordance with the literature value for the (001) surface of bulk Ni (Starke et al. 1992*a*). The spin splitting has been determined by fitting Gaussian line shapes to the spectral features. It should be noted that the transition appears at somewhat higher energy for the film if compared with the bulk Ni(001) surface. The bulk value is only reached for even higher film thickness.

It is worthwhile to mention the energy shift of the image-potential-induced surface state *IS* of the Ni film relative to the one of the Cu substrate. Since the *IS* are pinned to the vacuum level, the work-function change between Ni and Cu is reflected in the energy shift of the *IS*: it shifts to higher energies for Ni films on Cu(001). For the

6 ML Ni film, the *IS* appears at about 4.6 eV as compared with 4.15 eV for Cu(001). Upon further increase of the Ni thickness, the work function of the Ni films remains unchanged.

For comparison, IPE spectra at normal electron incidence of Co films on Cu(001) are shown in figure 5.2. In the lower part of the figure, the spectra of the Cu(001) substrate are displayed again (figure 5.2 (a)). The spectra for the 5 ML and the 10 ML thick Co films (figure 5.2 (b) and (c), respectively) show similar electronic states like the spectra for the thin Ni films. Analogous to Ni, a feature resulting from indirect non-$\boldsymbol{k}$-conserving transitions into empty d states, marked as Co-d, appears just above the Fermi level. For 5 ML Co, there is still some intensity above the background intensity for majority spin, because the attenuation of the Cu sp-band transition is not complete. Thus, the Cu transition is partially suppressed, while the intensity surplus in the minority channel originates from transitions into empty d states of Co. For 10 ML Co, only the Co d band transition shows up. The Co-d feature has a much higher spin asymmetry than the Ni-d feature despite a comparable band-structure situation. The reduced asymmetry of the Ni-d feature is discussed in detail in section 5.2. At higher energies, quantum-well states and resonances in the Co film show up. Compared to Ni, the Co quantum-well features have a much larger exchange splitting, because the energy difference between the $X_{4'}$ points for minority and majority spin is much larger in Co (see section 2.2.1). The spin dependence of the whole measured energy range is much stronger in Co than in Ni, even the one of the background. This is because the magnetic moment in Co is much higher compared to Ni. The spectra for 15 ML Co on Cu(001) are shown in figure 5.2 (d). For this thickness, the discrete two-dimensional quantum-well states have turned into the continuous three-dimensional sp-band. Thus, the Co sp-band transition, marked as Co-sp, shows up. The image-potential-induced surface state *IS* proves good surface quality of the 5 ML and the 10 ML thick Co films, but the lower intensity of *IS* for the 15 ML thick Co film indicates its worse film growth (see section 3.3). A more detailed discussion of Co films on Cu(001) can be found in Yu et al. (2003*b*).

5.1.2 Exchange splitting of the quantum-well states

In order to determine the exchange splittings of the observed quantum-well states, the spectra for 6 ML Ni on Cu(001) were measured with improved energy resolution. For this, the SrF_2 entrance window of the photon counter was heated to about 80 °C (see section 4.1.2). The result is presented in figure 5.3. As above, the data sets for minority and majority electron spin are represented by open red and filled green circles, respectively. In addition, filled black squares represent the spin-averaged data, that is the sum of the minority and majority intensities divided by a factor of 2. The black dotted line is a simple connection between the data points as guide to the eye. The spin-resolved spectra are shifted in energy compared to the spin-integrated ones for better clarity.

The peak positions of the quantum-well states have been determined by fitting Gaussian line shapes to the spectral features. These are shown as red, green, and black solid lines. Exchange splittings of 0.06 eV for the first quantum-well state

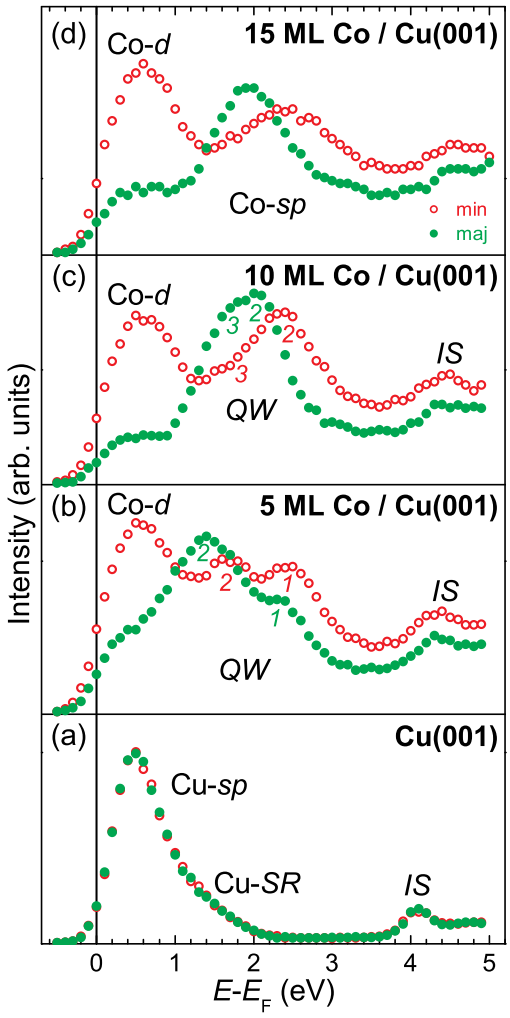

Figure 5.2: Spin-resolved inverse photoemission spectra at normal electron incidence of (a) the Cu(001) substrate and of (b) 5 ML Co, (c) 10 ML Co, and (d) 15 ML Co on Cu(001).

at about 2.70 eV, labeled *QW-1*, and of 0.02 eV for *QW-2* at about 1.90 eV are obtained. Owing to the small difference in energy between the top of the *sp* bands for minority and majority electrons, the exchange splittings of the quantum-well states are likewise quite small for Ni compared to e.g. Co (Yu et al. 2003*b*) (see above). For both quantum-well states, the minority feature is higher in energy than the majority feature. This is because the $X_{4'}$ point is also higher in energy for minority spin (see section 2.2.1).

The improved energy resolution shows that the spectral feature of the second quantum-well state is not symmetric. There is an increased intensity at the low-energy side of the peak. This is caused by the influence of the third quantum-well state, which shows up more clearly for 7 ML Ni and higher coverage (see sections 5.2.1 and 5.3).

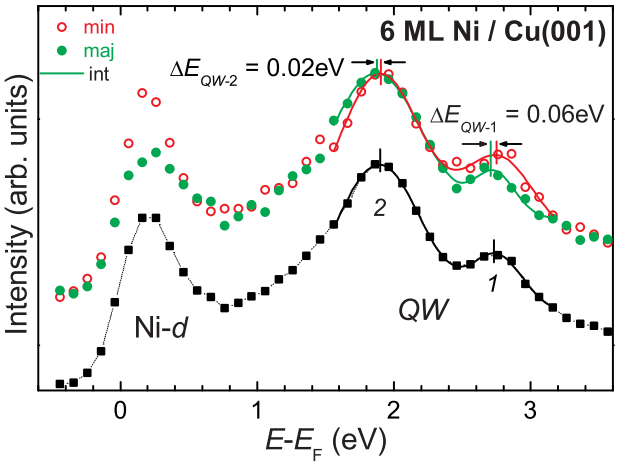

Figure 5.3: Spin-resolved inverse photoemission spectra of 6 ML Ni on Cu(001) at normal electron incidence (open red circles for minority spin, filled green circles for majority spin, black squares for spin-averaged data). The energy resolution was improved by heating the SrF_2 entrance window of the Geiger-Müller counter tube to 80 °C. The spin splitting ΔE is determined by fitting Gaussian line shapes to the spectral features.

5.1.3 Summary

The different spectral features of Ni films on Cu(001) have been introduced (Renken et al. 2007). There is no spin asymmetry in the spectra for the non-ferromagnetic Cu(001) substrate. The spectra of Ni on Cu(001) show the influence of the two spin-reorientation transitions turning the magnetization from in-plane to out-of-plane and back to in-plane with increasing Ni film thickness. At normal electron incidence, there is an spin asymmetry for in-plane magnetized films only.

The Ni-d feature just above the Fermi level, resulting from indirect non-$\boldsymbol{k}$-conserving transitions into empty d states, appears 0.25 eV lower in energy than the Cu-sp feature, resulting from bulk-like transition between sp states of Cu. For an in-plane film magnetization, the Ni-d feature of ultrathin Ni films (6 ML) appears in both the minority and the majority spin channels with a surplus for minority spin. In contrast, the Ni bulk band structure shows an exclusive minority character of the d holes (Eckardt and Fritsche 1987)(see section 2.2.1). This minority character is confirmed by IPE spectra of bulk Ni(001) (Starke et al. 1992*a*). Moreover, the Ni-d feature of an in-plane magnetized thick Ni films (100 ML) exclusively appears in the minority spin channel. As shown for comparison, also the Co-d feature of thin Co films on Cu(001) exclusively shows minority spin character. This is expected from the Co bulk band structure, which shows an exclusive minority character of the d holes as the one for Ni (see section 2.2.1). For ultrathin Ni films, the spin character of the Ni-d feature is discussed in detail in section 5.2.

The high spectral intensity of the image-potential-induced surface state proves good surface quality of the Ni films. The energy of the image state of the Ni films is

shifted relative to the one of the Cu(001) substrate, showing the work function change between Ni and Cu. The image state shifts about 0.45 eV to higher energies for Ni films on Cu(001).

As expected from the bulk band structures (see section 2.2.1), spectral features resulting from quantum-well states with complete electron confinement appear between the top of the Cu *sp* band and the top of the spin-dependent Ni *sp* bands. The energy of the quantum-well states (see section 2.2.2) and the intensity of the corresponding spectral features depend on the Ni film thickness. For 6 ML Ni on Cu(001), exchange splittings of 0.06 eV for the first quantum-well state and of 0.02 eV for the second one are obtained. Concerning the Ni bulk band structure, the exchange splittings of the quantum-well states are of the same order of magnitude as the difference in energy of the tops of the majority and minority *sp* bands, which is 0.04 eV (see section 2.2.1). For both quantum-well states, the minority feature is higher in energy than the majority feature, because the top of the minority *sp* band is also higher in energy. Compared with Co, the Ni quantum-well features have a much smaller exchange splitting, because the energy difference between the top of the *sp* bands for minority and majority spin is much smaller in Ni (see section 2.2.1). For Ni, the exchange spitting of the quantum-well state at higher energy is larger than the one of the quantum-well state at lower energy. The reason for this may be that the quantum-well feature at lower energy almost is at the top of the Cu *sp* band and thus may be a quantum-well resonance, which is less confined. In contrast, for Co on Cu(001) the exchange spitting of the quantum-well feature at lower energy is larger than the one of the quantum-well state at higher energy. The larger splitting of the quantum-well feature at lower energy, with clearly is a quantum-well resonance, is believed to be most likely caused by a stronger hybridization with the magnetic *d* states of Co (Yu et al. 2003*b*). For Ni on Cu(001), a possible hybridization of the quantum-well states with the *d* states of Ni may not strongly influence the exchange splitting of the quantum-well states, because the reduced spin-asymmetry of the Ni-*d* transition indicates a reduced magnetic behavior of thin Ni films (see section 5.2). For thick Ni films on Cu(001), the quantum-well features have disappeared in favor of the well-known bulk transition between *sp*-like bands. For 100 ML Ni, the spin splitting amounts to 0.10 eV in accordance with the literature value for the (001) surface of bulk Ni (Starke et al. 1992*a*). In contrast to the discrete quantum-well states, the measured spin splitting of the Ni-*sp* transition does not represent its actual exchange splitting, because it results from the exchange splitting and the dispersions of the initial as well as of the final band (see section 4.1.1). Concerning the Ni-*sp* transition, the energy difference between the majority and minority initial band is much larger than the one of the final band and in particular larger than the one of the top of the final *sp* band. Consequently, the measured spin splitting of the bulk Ni-*sp* transition is larger than the exchange splitting of the discrete quantum-well states. A more detailed investigation of the dependence of the spectral features on the Ni film thickness follows in section 5.3.

5.2 Spin-dependence of the Ni-*d* bulk feature

The appearance of the Ni-*d* feature in the majority channel in thin Ni films on Cu(001) as mentioned above could possibly be influenced by the underlying Cu-*sp* feature, a reduced magnetization, the magnetization direction, and a modified band structure compared to bulk Ni. All these influences are discussed in this section.

5.2.1 Influence of the Cu(001) substrate

The reduced spin asymmetry cannot be attributed to the spectral intensity of the non-ferromagnetic Cu substrate attenuated by the Ni overlayer. The Ni-*d* feature appears at an energy of about 0.25 eV. However, the Cu-*sp* transition appears at a distinctly different energy of 0.50 eV.

An inverse photoemission spectrum can be simulated if the measured transitions are known. For this, the expected peaks p are added to a background b. The sum $(b+p)$ is multiplied with $(1-f)$, where

$$f(E) = [e^{-\frac{E-E_\mathrm{F}}{k_\mathrm{B}T}} + 1]^{-1} \tag{5.1}$$

is the Fermi-Dirac function with Boltzmann's constant k_B and the temperature T. If the apparatus function is a Gaussian, a spectrum can be simulated by convoluting the result $(b+p)(1-f)$ with the apparatus function

$$a(E) = \tfrac{1}{\sqrt{2\pi\sigma^2}}\, e^{-\frac{(E-E_0)^2}{2\sigma^2}}, \tag{5.2}$$

where E_0 is the center of the Gaussian distribution and σ is its variance.

Figure 5.4 shows the measured data of 6 ML Ni on Cu(001) (open red circles for minority spin, filled green circles for majority spin) as well as $(b+p)(1-f)$ (red dotted line for minority spin, green dotted line for majority spin) and the simulated spectra (red solid line for minority spin, green solid line for majority spin). For the simulation, the temperature is $T = 300\,\mathrm{K}$ and the variance is $\sigma = 170\,\mathrm{meV}$ (full width at half maximum FWHM = 400 meV). The background is kept constant and Gaussian line-shaped peaks are used. The energies and intensities of the peaks are summarized in table 5.1. The peaks of the quantum-well state, that is actually Ni-*QW-2*, are assumed to be at 1.90 eV with slightly different intensities for minority spin and majority spin. The $\mathrm{Ni}_{\uparrow\downarrow}$-*d* peaks are at 0.20 eV and the Cu-*sp* peak at 0.50 eV. Compared to the $\mathrm{Ni}_{\uparrow\downarrow}$-*d* peaks, the intensity of the Cu-*sp* peak is very small. Moreover, it is not possible to get an acceptable result for the simulated spectra by increasing the intensity of the Cu-*sp* peak and therefore reducing the intensity of the $\mathrm{Ni}_{\uparrow}$-*d* peak. This would lead to a similar asymmetry in the peak maximum, but it would also shift the peak too high in energy. Thus, it is necessary to use the majority Ni-*d* peak to simulate the experimental spectra. There is no or only insignificant influence of the Cu-*sp* peak on the spin asymmetry.

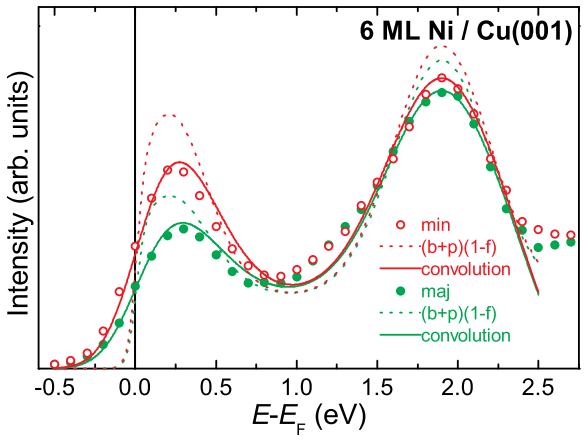

Figure 5.4: Simulated spin-dependent inverse photoemission spectra of 6 ML Ni on Cu(001) at normal electron incidence (open red circles for minority spin, filled green circles for majority spin, dotted lines for background b and peaks p multiplied with unity minus the Fermi-Dirac function, $(1-f)$, and solid lines for the simulated spectra including the convolution with the apparatus function). See text for details.

	E (eV)	I (arb. units)
Cu-sp	0.50	0.2
$\mathrm{Ni}_{\downarrow}$-d	0.20	3.7
$\mathrm{Ni}_{\uparrow}$-d	0.20	2.0
$\mathrm{Ni}_{\downarrow}$-QW	1.90	5.2
$\mathrm{Ni}_{\uparrow}$-QW	1.90	4.9

Table 5.1: Energies E and intensities I of the respective peaks used for the simulated IPE spectra of 6 ML Ni on Cu(001) shown in figure 5.4.

5.2.2 Influence of the reduced magnetization

The Curie temperature T_C of a thin Ni film is strongly thickness-dependent and is reduced compared to bulk Ni (Huang et al. 1994, Tischer et al. 1994, Baberschke 1996, Baberschke 2001). As a consequence, for measurements at room temperature, T/T_C is enhanced from 0.46 for bulk Ni to about 0.75 for a 6 ML thick Ni film on Cu(001). Thus, the magnetization of the Ni film is reduced compared to bulk Ni. Figure 5.5 shows a sketch of the magnetization M in units of the saturation magnetization M_0 as a function of the temperature T in units of the Curie temperature T_C for 6 ML Ni on Cu(001). With increasing temperature, the magnetization decreases following the power law $M/M_0 = (1-T/T_\mathrm{C})^{0.23}$ until the Curie temperature is reached. This power law well describes the behavior in thin Ni films on Cu(001)

also for low temperatures (Huang et al. 1994), although actually the power law is only valid for temperatures near the Curie temperature (see section 3.1). According to the power law, at room temperature T_R it is $M/M_0(T = T_R) = 0.72$. As can be further seen by the graph, for $T = 100\,\mathrm{K}$, it is $M/M_0(T = 100\,\mathrm{K}) = 0.93$.

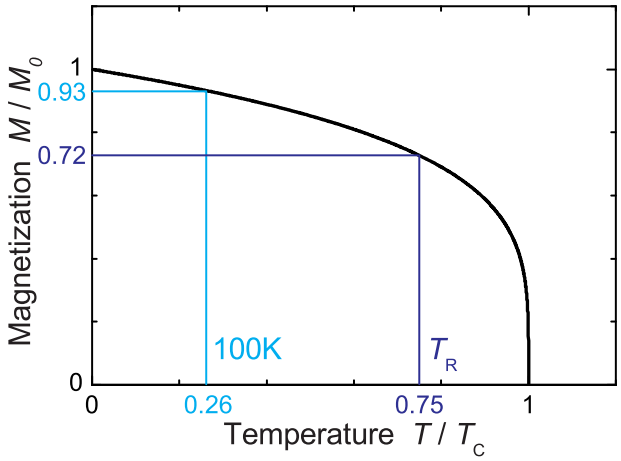

Figure 5.5: Sketch of the magnetization M/M_0 as a function of the temperature T/T_C for 6 ML Ni on Cu(001).

The reduced magnetization can be taken into account when normalizing the IPE spectra to hypothetical 100 % spin polarization (see section 4.1.2). For this, the spin polarization of the electron beam $P = 33\,\%$ has to be multiplied with the reduced magnetization M/M_0 to obtain the effective polarization: $P_{eff} = 0.33\ M/M_0$. Here it is assumed that the magnetization direction is totally in-plane and parallel to the polarization direction of the electron beam. A possible out-of-plane magnetization direction is discussed in 5.2.3. Figure 5.6 (a) displays a part of the spectra shown in figure 5.3, namely the spin-resolved Ni-d feature for 6 ML Ni at room temperature measured with heated SrF_2 entrance window of the photon counter (80 °C). In figure 5.6 (b), these spectra are normalized to the hypothetical magnetization $M = M_0$ using $M/M_0 = 0.72$. Minority and majority data are represented by open red and filled green circles, respectively, the spin-averaged data by a solid grey line just connecting the data points. The peaks are fitted by Gaussian line shapes. As can be seen by comparison of figures 5.6 (a) and (b), the spin asymmetry is only slightly increased by considering the reduced magnetization. The Ni-d feature still appears for majority spin.

What happens if a measurement is taken at a temperature far below room temperature? For this situation, figure 5.7 (a) shows spectra of the Ni-d feature at normal electron incidence taken at $T = 100\,\mathrm{K}$ with improved experimental resolution ($T_{SrF_2} = 80\,°\mathrm{C}$) and (b) shows the corresponding hypothetical spectra for $M = M_0$ using $M/M_0 = 0.93$. To compare the spectra with those taken at room temperature, all spectra are normalized to the same background intensity at $E = 0.8\,\mathrm{eV}$. The asymmetry of the Ni-d feature in figure 5.7 (a) is noticeably higher if compared to

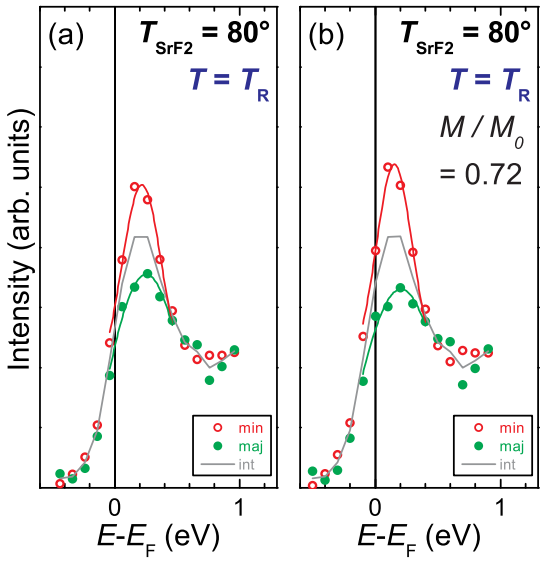

Figure 5.6: Spin-resolved inverse photoemission spectra of 6 ML Ni on Cu(001) at normal electron incidence (open red circles for minority spin, filled green circles for majority spin, solid grey line for spin-averaged data). The spectra in (a) show the Ni-d feature of the spectra from figure 5.3 taken at room temperature. The spectra in (b) are normalized to the hypothetical magnetization $M = M_0$. The peaks are fitted by Gaussian line shapes.

the spectra taken at room temperature (figure 5.6). Considering the little temperature dependence of the magnetization for such low temperatures, the asymmetry of the hypothetical spectra in figure 5.7 (b) is further only slightly increased. It has to be noted that normalizing the two spectra measured at room temperature and at $T = 100\,\mathrm{K}$ to $M = M_0$ should result in the same hypothetical spectra. But obviously figure 5.6 (b) and figure 5.7 (b) show different spectra. The intensity of the spin-averaged feature is higher for $T = 100\,\mathrm{K}$ reflecting the temperature dependence of the bulk-like transitions. This also influences the asymmetry, that is higher for $T = 100\,\mathrm{K}$ than for room temperature. Moreover, the value $T_\mathrm{R}/T_\mathrm{C} = 0.75$ is taken from Huang et al. (1994) for actual 6.2 ML Ni on Cu(001). In addition, the thickness calibration may be slightly different. Thus, the true value for $T_\mathrm{R}/T_\mathrm{C}$ may be higher. Owing to the strong temperature dependence of the magnetization in the range of the room temperature, the value for the reduced magnetization at room temperature consequently may be smaller than the used $M/M_0(T_\mathrm{R}) = 0.72$. This would result in a higher asymmetry for the spectra for $M = M_0$ at room temperature.

Nevertheless, there is still a little peak left for the majority electrons at $T = 100\,\mathrm{K}$. Consequently, the reduced Curie temperature of thin Ni films on Cu(001) and the temperature dependence of the magnetization cannot sufficiently give reasons for the appearance of the Ni-d feature for majority spin.

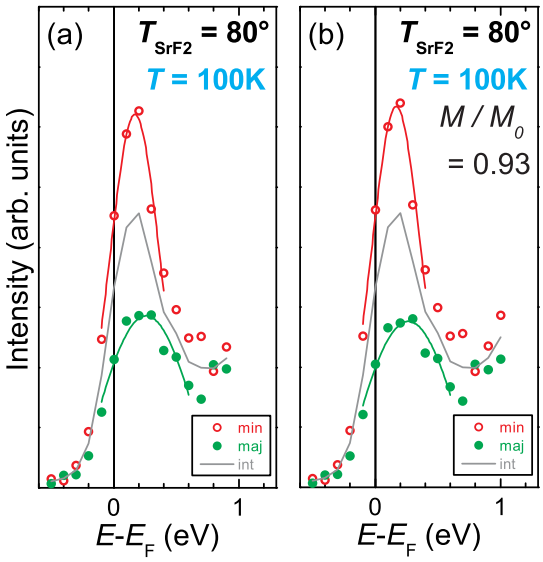

Figure 5.7: (a) Spin-resolved inverse photoemission spectra of 6 ML Ni on Cu(001) at normal electron incidence at $T = 100\,\mathrm{K}$, $T_{\mathrm{SrF_2}} = 80\,^{\circ}\mathrm{C}$. The spectra in (b) are normalized to a hypothetical magnetization $M = M_0$.

5.2.3 Influence of the magnetization direction

To begin with, the thickness of the spin-reorientation transition from in-plane to out-of-plane magnetization in Ni films on Cu(001) depends on the sample temperature, too (see section 3.2). But as this thickness increases with increasing temperature, the different asymmetries for the two $M = M_0$ spectra discussed in section 5.2.2 cannot be attributed to a change of the magnetization direction caused by the temperature-dependent spin-reorientation transition.

Another possible reason for the appearance of the minority Ni-d feature may be a magnetic structure of the Ni film, containing magnetic domains with different in-plane magnetization directions. But this has not been reported in the literature so far. The magnetization of the Ni films has further been checked by measuring the spin polarization of secondary electrons (see section 5.3).

Moreover, the asymmetry in the IPE spectra may be reduced by magnetic domains which are magnetized out of plane. Owing to the film growth, the film is not perfectly flat and may contain islands of thicker layers (Shen et al. 1995) with out-of-plane magnetization, thereby reducing the observed in-plane spin asymmetry. The influence of an out-of-plane magnetization can be deduced from measurements taken at off-normal electron incidence. Figure 5.8 shows the Ni-d feature for 6 ML Ni on Cu(001) at (a) normal electron incidence ($T_{\mathrm{SrF_2}} = T_{\mathrm{R}}$) and at (b) $\theta = 45°$ off-normal electron incidence. All spectra are normalized to equal background intensity to simplify a comparison with each other. At $\theta = 45°$, the effective spin polarization just consists of half in-plane magnetization and half out-of-plane magnetization. The spectra show that the intensity of the Ni-d feature is much higher at $\theta = 45°$, and so is the spin asymmetry. Taking only this into account, it cannot be said whether the reason for the higher asymmetry is in out-of-plane magnetized domains

or in the different angle of incidence. In addition, the spectra have to be compared with corresponding spectra of totally out-of-plane magnetized films. For this, figure 5.9 shows spectra of 10 ML Ni on Cu(001) at (a) normal electron incidence and at (b) $\theta = 50°$ off-normal electron incidence. The spectra at normal incidence do not show any spin dependence. This means that there is no in-plane magnetization, the 10 ML Ni film is completely magnetized out of plane. But at $\theta = 50°$, the Ni-d feature still appears for majority spin. As a consequence, the reduced asymmetry of the Ni-d feature cannot be attributed to a mixture of in-plane and out-of-plane magnetized domains. Furthermore, the intensity as well as the spin asymmetry of the Ni-d feature for 10 ML Ni and at $\theta = 50°$ are similar to those for 6 ML Ni and at normal electron incidence. Aside from small differences owing to the different off-normal angles of incidence, this means that the asymmetry of the spectra from 6 ML Ni can as well be derived from one magnetization direction only, which in this case is the in-plane magnetization direction. There are no out-of-plane domains for 6 ML Ni which may lead to a decrease of the in-plane spin-asymmetry.

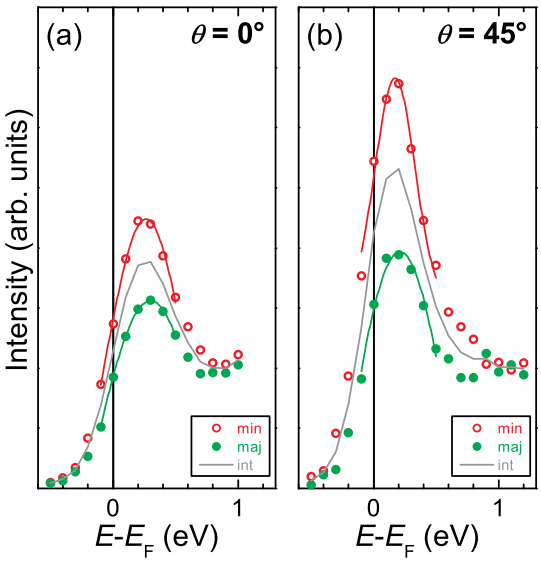

Figure 5.8: Spin-resolved inverse photoemission spectra of 6 ML Ni on Cu(001) at (a) $\theta = 0°$ and (b) $\theta = 45°$ at sample room temperature.

Another fact supports that the appearance of the Ni-d feature for majority spin is neither due to a reduced magnetization nor to an out-of-plane magnetization. For thin Ni films on Co, the magnetization of the Ni films is pinned to the magnetization in the underlying Co. Therefore there is no spin-reorientation transition and even Ni films thicker than 8 ML are completely in-plane magnetized (Won et al. 2003). As a Co underlayer a 12 ML thick film is chosen, because for this thickness the Curie temperature is high enough to allow a fully magnetized film and the film quality is still good, making a flat Co-Ni interface possible. Figure 5.10 displays spectra of (a) 6 ML Ni on Cu(001) and of (b) 6 ML Ni on 12 ML Co / Cu(001) at normal electron incidence. Both spectra show about the same intensity and spin asymmetry for the Ni-d peak. Consequently, both 6 ML Ni films have the same magnetization. The

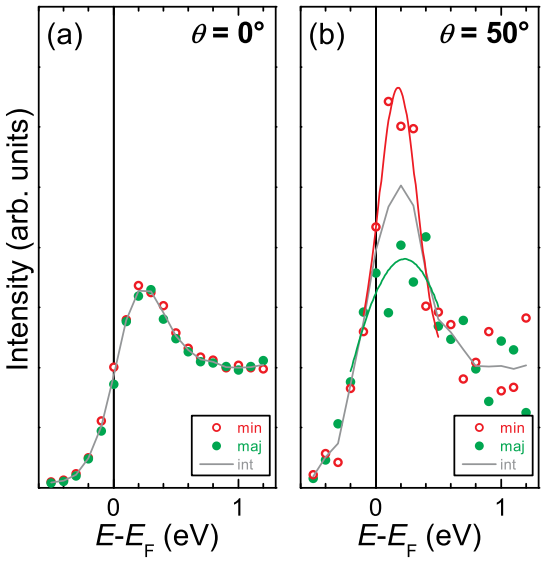

Figure 5.9: Spin-resolved inverse photoemission spectra of 10 ML Ni on Cu(001) at (a) $\theta = 0°$ and (b) $\theta = 50°$ at sample room temperature.

Ni film on Cu(001) is completely in-plane magnetized as the Ni film on Co. The pinning of the magnetization in Ni films on Co is confirmed by the spectra shown in figure 5.11 of (a) 10 ML Ni on Cu(001) and of (b) 10 ML Ni on 12 ML Co / Cu(001) at normal electron incidence. For 10 ML Ni on Cu(001), the magnetization is out of plane and there is zero spin asymmetry. But for 10 ML Ni on Co, the magnetization of the Ni film is pinned to the magnetization of the Co film. Thus, both the Co film and the Ni film are in-plane magnetized. Nevertheless, the asymmetry of the Ni-d feature is not that high as to be expected on the basis of the bulk band structure or of a 100 ML thick Ni film. But the appearance of the Ni-d feature for majority spin cannot be explained by an out-of-plane magnetization.

5.2.4 Summary

The Ni-d feature in thin in-plane magnetized Ni films on Cu(001) (6 ML) appears in both the minority and in the majority spin channel with a surplus for minority spin. This is in contrast to expectations from the Ni bulk band structure, which shows an exclusive minority character of the d holes (see section 2.2.1). This minority character is confirmed by IPE spectra of bulk Ni(001) (Starke et al. 1992*a*) and of thick in-plane magnetized Ni films (100 ML).

Since the Ni-d transition and the Cu-sp transition appear at distinctly different energies, the reduced spin asymmetry of the Ni-d feature cannot be attributed to the spectral intensity of the non-ferromagnetic Cu substrate attenuated by the Ni overlayer, what has been confirmed by simulating the spectra. The reduced Curie temperature of thin Ni films on Cu(001) compared to bulk Ni and the temperature dependence of the magnetization cannot sufficiently give reasons for the reduced spin asymmetry, what has been shown by considering the reduced magnetization when

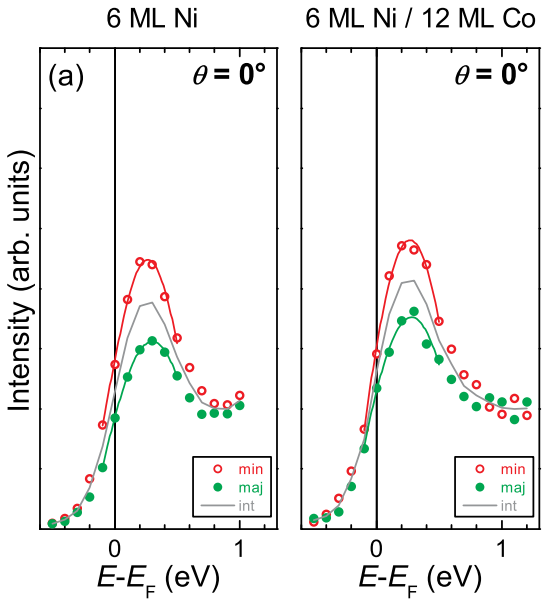

Figure 5.10: Spin-resolved inverse photoemission spectra at normal electron incidence of (a) 6 ML Ni on Cu(001) and of (b) 6 ML Ni on 12 ML Co / Cu(001).

normalizing the IPE spectra to hypothetical 100 % spin polarization. A reduction of the spin asymmetry cannot be attributed to domains with different magnetization direction, what has been checked by measurements at off-normal electron incidence and what has been confirmed by measurements on magnetic pinned in-plane magnetized Ni films on Co. Moreover, it has been mentioned that the reduction of the spin asymmetry of the Ni-*d* feature cannot be due to intensity contributions by transitions into quantum-well states.

Consequently, no indication has been found that the reason for the appearance of the Ni-*d* feature in both the minority and in the majority spin channel is due to the Cu substrate or the magnetization of the Ni film. Hybridization between the Ni *d* bands and the Cu substrate can be excluded, because this affects the interface layers only (see section (3.5.1). In particular, the majority Ni-*d* feature appears in 6 ML Ni on Cu(001) and also in 10 ML Ni on Co / Cu(001) and the inverse photoemission technique probes the topmost layers only. Moreover, a hybridization between Ni *d* bands and Cu *d* bands is not likely. The Cu *d* bands are significant lower in energy than the Ni *d* bands, so that hybridization does not shift the Ni *d* bands to higher energy. A hybridization between the Ni *d* bands and Cu *sp* bands only occurs at the interface. Thus, the reduced spin asymmetry of the Ni-*d* feature in thin Ni films compared to bulk Ni must rather have its origin in a modified band structure such that the majority *d* bands are not entirely below the Fermi level. Owing to the existence of majority *d* holes, thin Ni films on Cu(001) do not represent a strong ferromagnet. Consequently, transitions into the unoccupied *d* bands lead to the spectral intensity for majority spin. To check the modified band structure of thin Ni films compared to bulk Ni, a calculation of the spin-resolved band structure of thin Ni films on Cu(001) would be helpful. A calculation of spin-resolved inverse

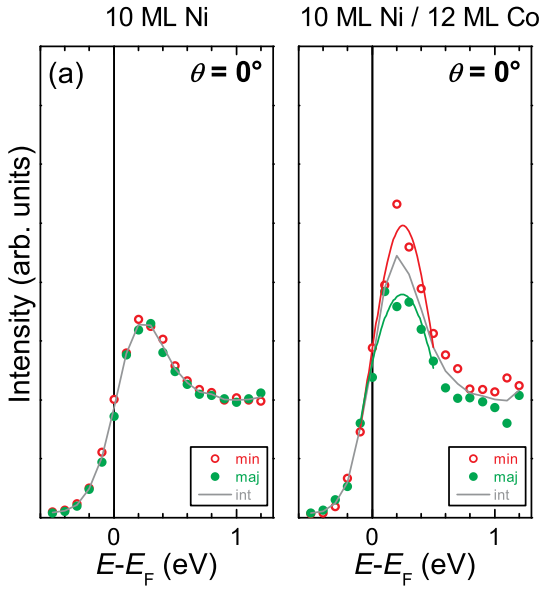

Figure 5.11: Spin-resolved inverse photoemission spectra at normal electron incidence of (a) 10 ML Ni on Cu(001) and of (b) 10 ML Ni on 12 ML Co / Cu(001).

photoemission spectra by J. Braun is in progress.

5.3 Ni on Cu(001): Thickness dependence

In detail, the dependence of the IPE spectra on the Ni film thickness of n ML Ni on Cu(001) is presented in figure 5.12, covering the range from pure Cu(001) to 15 ML Ni. The spin-averaged spectra are shown in figure 5.12 (a) and the spin-resolved spectra in figure 5.12 (b). The spectra are normalized to equal spin-averaged background intensity at an energy of about 3.7 eV. The spectra for the Cu(001) substrate are multiplied by a factor of 0.2, the spectra for 1 and 2 ML Ni by a factor of 0.5 for an easier presentation of the data. From the bulk band structures of Ni and Cu (see section 2.2.1), in the energy range between the Fermi level and $E^{Cu}_{X_{4'}} = 1.80$ eV quantum-well resonances may be detected. This energy range is marked by the yellow hatched area. The energy range between $E^{Cu}_{X_{4'}} = 1.80$ eV and $E^{Ni}_{X_{4'}} = 2.76$ eV (spin-averaged), in which the formation of true quantum-well states is possible, is marked by the yellow area. The shift in energy of the individual states as a function of the Ni film thickness is accentuated by the colored solid lines.

In the lower part of figure 5.12 (a) the spectrum of the Cu(001) substrate is presented again. With increasing Ni coverage, the intensity of the Cu-*sp* feature at 0.5 eV rapidly decreases because of the attenuation of the Cu *sp*-band transition owing to the Ni overlayers. Moreover, the Cu-*sp* feature becomes superimposed by the Ni-*d* feature at 0.25 eV. The latter appears for a film thickness from 3 ML and does not shift in energy. For 2 ML, the feature further contains contributions from transitions into the second quantum-well states, *QW-2*. The first quantum-well state, *QW-*

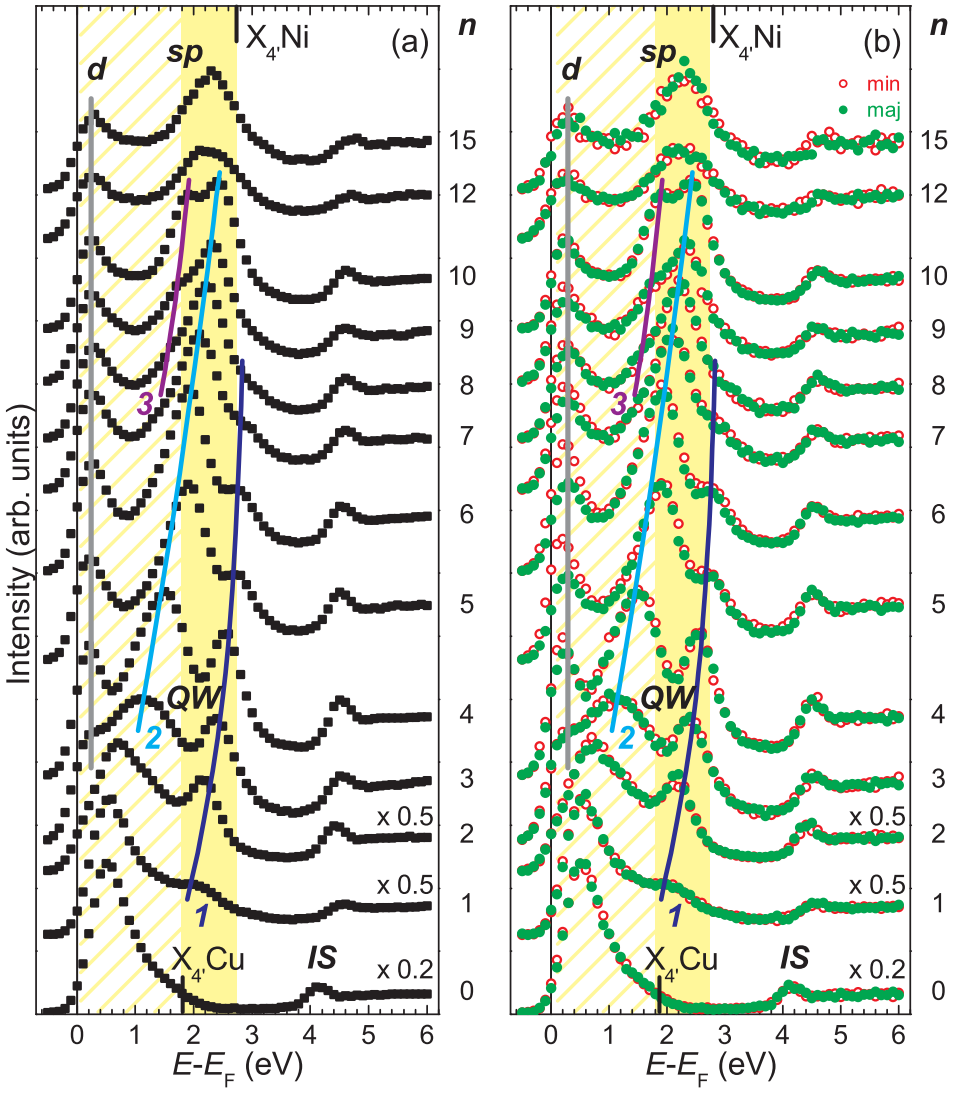

Figure 5.12: Spin-averaged (a) and spin-resolved (b) inverse photoemission spectra of n ML Ni on Cu(001), $0 \leq n \leq 15$, at normal electron incidence, showing the thickness dependence of the Ni-*d* bulk feature, the quantum-well features *QW-1,2,3* and the Ni-*sp* bulk feature, respectively, and the image-potential-induced surface state *IS*. The spectra are normalized to equal background intensity. The spectra for 0, 1, and 2 ML Ni are reduced by the given factors. See text for details.

1, shows up in the thickness range between 1 and 8 ML Ni. Like all observed quantum-well features, the corresponding spectral feature shifts up in energy with increasing Ni coverage and converges to the energy of the Ni $X_{4'}$ point. Its energy position lies in the yellow-colored range between $E^{Cu}_{X_{4'}}$ and $E^{Ni}_{X_{4'}}$, thus it is a true quantum-well state. For a Ni film thickness above 8 ML, *QW-1* cannot be clearly observed any more. The intensity of *QW-1* decreases to zero and the feature becomes superimposed by *QW-2*. The latter contributes to the feature just above the Fermi

level in the spectrum for 2 ML Ni. In the thickness range from 2 to 4 ML Ni, *QW-2* is a quantum-well resonance, but from 5 ML Ni it becomes a true quantum-well state. As best can be seen from the spectra for 3 and 4 ML Ni, the feature caused by the quantum-well resonance *QW-2* is much broader than the feature caused by the true quantum-well state *QW-1*. The reason for this is that the resonance states are less confined. Furthermore, the intensity of *QW-2* rapidly increases from 3 to 5 ML Ni when the resonance state becomes a true quantum-well state. A third quantum-well feature, *QW-3*, emerges in the spectrum for 7 ML Ni as a resonance state and becomes a true quantum-well state for about 9 ML Ni. For 12 and 15 ML, the discrete quantum-well states cannot be resolved in the spectra any more. Only one broad spectral feature remains, showing the turning of the discrete quantum-well states into the continuous Ni-*sp* bulk band. The image-potential-induced surface state *IS* continuously shifts to higher energies with increasing Ni film thickness owing to the changing work function.

The spin-resolved spectra in figure 5.12 (b) only show a very weak spin dependence of thin Ni films on Cu(001). The spin dependence can be best observed for the feature just above the Fermi level. For a film thickness up to 4 ML Ni, no spin asymmetry shows up, because the Curie temperature is below room temperature (see section 3.2). A clear spin asymmetry can be observed from 5 ML Ni. The asymmetry is largest for 6 ML Ni, and it decreases for thicker films due to the spin-reorientation transition. For the spectra of 5 and 6 ML Ni, also the spin dependence of the quantum-well states is strongest. The change of the magnetization from in-plane to out-of-plane does not show up all of the sudden in the spectra, because the film thickness is not uniform. For example, a 8 ML Ni film also contains parts with 7 as well as 9 ML Ni. Thus, the parts with 9 ML may be already magnetized out of plane, while the other parts may be still magnetized in plane. By these IPE measurements, the thickness of the spin-reorientation transition amounts to about 9 ML Ni.

The in-plane magnetization of thin Ni films on Cu(001) is reflected in the spin asymmetry of secondary electrons. Figure 5.13 shows the spin asymmetry as a function of the Ni film thickness. For very low coverage, the Curie temperature is below room temperature, thus the asymmetry is zero. The asymmetry increases with increasing coverage and reaches the highest values for 6 and 7 ML Ni. In the maximum, the spin asymmetry amounts to $(0.6 \pm 0.1)\,\%$. With A the spin asymmetry and S_{eff} the effective Sherman function, the spin polarization of the secondary electrons is $P = A/S_{eff}$ (Kessler 1985). The Sherman function gives the quantitative relation between asymmetry and polarization and is a measure of the analyzing power. For the used Mott detector, the Sherman function has been determined by measuring the known polarization of the spin-polarized electron source (33 %). It is $S_{eff} = (15 \pm 1)\,\%$. Thus, the maximum polarization of the secondary electrons from the Ni films is $P = (4 \pm 1)\,\%$. This is in accordance with the spin polarization of secondary electrons from bulk Ni(001), which is between 2 and 10 % depending on the electron energy (Landolt 1986). For 8 ML Ni, the spin-reorientation transition has already started to turn the magnetization direction out of plane. For higher coverage, the Ni films are completely magnetized out of plane, and again the asymmetry is zero.

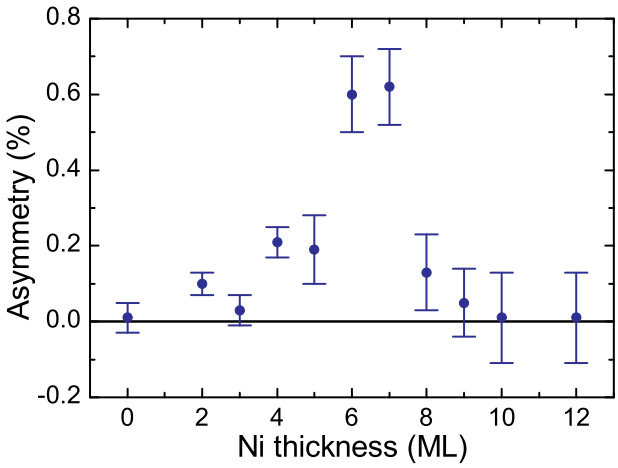

Figure 5.13: In-plane spin asymmetry as a function of the Ni film thickness of n ML Ni on Cu(001).

The energies of the quantum-well states as a function of the film thickness have been modeled by the phase accumulation model (see section 2.2.2) for ultrathin Ni films on Cu(001). Figure 5.14 shows the energy relative to the Fermi level as a function of the film thickness. The data points represent the spin-averaged quantum-well features *QW-1,2,3* from figure 5.12 (a). The solid lines represent the calculated energy-thickness relation of the respective quantum-well states obtained by equations 2.7 and 2.10. The film thickness is $\frac{d_\nu(E)}{a} = n$, with n from figure 5.12. The free parameter $G = 0.9$ gives the best agreement between the model calculation and the experimental data for the first quantum-well state. Only the first quantum-well state is completely confined for every measured Ni coverage. For only partial electron confinement, deviations from the model are expected. This is true for the second and third quantum-well state below $E^{Cu}_{X_4'} = 1.80\,\text{eV}$, where these states actually are quantum-well resonances.

For further increased Ni film thickness, the spin-averaged spectra of n ML Ni on Cu(001) with $10 \leq n \leq 100$ are shown in figure 5.15. The spectra are normalized to equal background intensity at an energy of 3.7 eV. As before, in the yellow hatched area quantum-well resonances may appear, whereas in the yellow area the formation of true quantum-well states is possible.

The spectrum of 10 ML Ni on Cu(001) again shows the Ni-*d* feature just above the Fermi level, the second and the third quantum-well state *QW-2,3* at higher energy as well as the image state *IS*. The quantum-well feature contains contributions from two discrete quantum-well states, which show up as two peak structures in the spectrum. With increasing Ni film thickness, the Ni-*d* feature remains at constant energy during the whole thickness range. The image-potential induced surface state *IS* strongly decreases in intensity with increasing Ni film thickness. Above 15 ML Ni, the image state does not show up as a peak anymore. Only an edge at the vacuum level appears in the spectra. This reflects the worse film quality due to the pyramidal growth

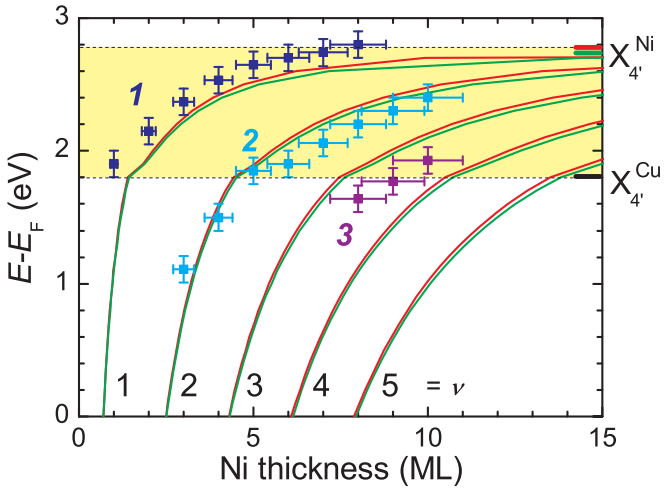

Figure 5.14: The energy of the quantum-well states relative to the Fermi level for ultrathin Ni films on Cu(001) as a function of the film thickness. The measured quantum-well energies, obtained from the spin-averaged spectra in figure 5.12 (a), are compared with the curves calculated by the phase accumulation model.

above 10 ML Ni (see section 3.2). The film surface is no longer plain, inhibiting the formation of image-potential induced surface states. Furthermore, the part of surface with different film thickness than the average one increases with increasing film thickness. Therefore, contributions from transitions into quantum-well states resulting from different film thickness are mixed in the spectrum. This smears out the individual spectral features to one resulting broad feature above 10 ML Ni. Up to 15 ML Ni, this resulting feature shows the typical behavior of quantum-well states: It shifts up in energy with increasing film thickness towards the top of the Ni *sp* band and the Ni $X_{4'}$ point, respectively, at 2.76 eV. But above 15 ML Ni, this behavior changes: Now the resulting feature shifts down in energy with increasing film thickness. This is no longer a typical quantum-well-like behavior. For 80 ML Ni, the resulting feature appears at the same energy as the transition into the bulk Ni-*sp* band at 1.7 eV. Therefore, it cannot be identified as quantum-well feature any more. Instead, the bulk *sp* band is formed. Above 80 ML Ni, no further energy shift of the corresponding spectral feature appears.

Thus, between 15 and 80 ML Ni the transition from two-dimensional discrete quantum-well states to a three-dimensional continuous bulk band occurs. The discrete quantum-well states appear as peaks in the spectra at their individual energies owing to their broadening in $\boldsymbol{k}_\perp$ (see section 2.2.3). In contrast, $\boldsymbol{k}_\perp$ is a good quantum number for a continuous band. The optical transition into the bulk *sp* band results in exactly one peak in the spectra at an energy where the photon detection energy matches the energy difference between the initial and the final band. Moreover, the quantum-well states converge towards $X_{4'}^{Ni} = 2.76$ eV, whereas the Ni-*sp* bulk transition appears at the lower energy 1.7 eV. As a consequence, the spectral

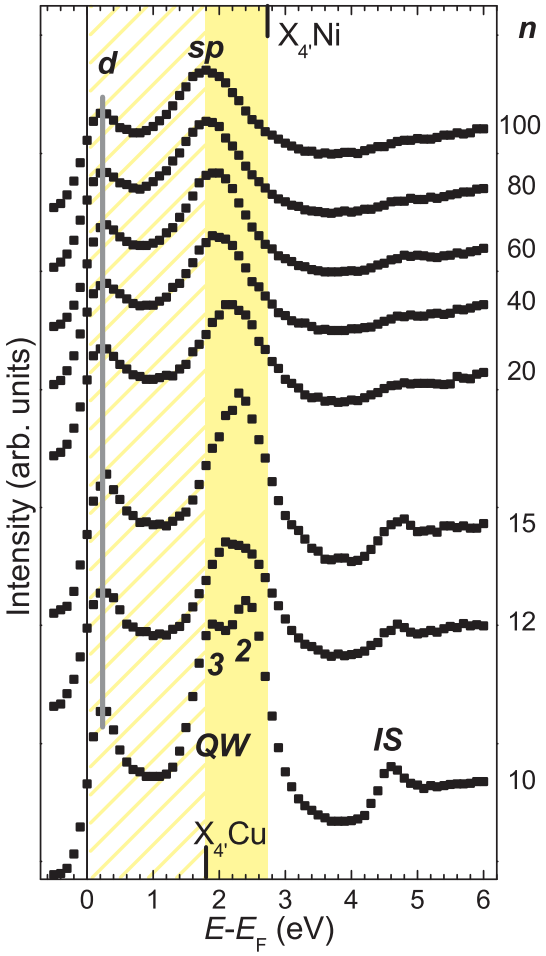

Figure 5.15: Spin-averaged inverse photoemission spectra of n ML Ni on Cu(001), $10 \leq n \leq 100$, at normal electron incidence, showing the transition from quantum-well features (*QW-2,3*) to the Ni-*sp* bulk feature.

feature shifts down in energy with increasing Ni film thickness when the bulk band is formed.

Summary

All measured features depend on the Ni film thickness. With increasing Ni film thickness, the image-potential-induced surface state continuously shifts to higher energies owing to the changing work function. The Ni-*d* feature appears for a film thickness from 3 ML Ni and does not shift in energy. Three quantum-well features are clearly resolved and show the typical behavior: They shift up in energy with increasing Ni film thickness and converge towards the top of the Ni *sp* band. This thickness dependence has been confirmed by the phase accumulation model. Above 10 ML Ni, the discrete quantum-well states cannot be resolved in the spectra any more due to the worth film quality. Above 15 ML Ni, the bulk *sp* band begins to

form. The corresponding spectral feature shifts down in energy until the energy of the transition into the bulk Ni-*sp* band is reached at 80 ML Ni.

The spin-resolved spectra only show a weak spin dependence. Up to 4 ML Ni film thickness, there is no spin asymmetry owing to the Curie temperature, which is below room temperature. The asymmetry is largest for 6 ML Ni. It decreases for thicker films due to the spin-reorientation transition. This behavior has been confirmed by spin-polarized secondary electron emission.

The appearance of discrete quantum-well states indicates a two-dimensional behavior up to 15 ML Ni film thickness. For these ultrathin films, $\boldsymbol{k}_\perp$ is not yet a good quantum number and the Ni-*sp* band is not continuous. The formation of the three-dimensional continuous bulk *sp* band is not completed below 80 ML Ni film thickness. In contrast, transitions into the localized Ni-*d* bands appear from 3 ML Ni film thickness. However, discrete quantum-well states derived from occupied *d* bands have been identified in Ag films on Fe (Luh et al. 2000) and in Au films on W(110) (Shikin et al. 2002). Whereas the *sp* electrons are nearly free-electron-like, the *d* electrons are much more localized. They have a wave function that is more compact and concentrated near the atomic core. They experience a larger correlation effect, have much smaller energy dispersions and group velocities and a generally short lifetime. Thus the mean free path, being the product of the group velocity and the lifetime, is also short. Consequently, the *d* wave functions are much more localized, and quantum-well states diminish when the film thickness becomes larger than the mean free path because of the loss of phase coherence. For Ni, the mean free path is quiet small (see section 4.1.1). The unoccupied *d* bands of Ni show up in a small energy range only, and the flat dispersion makes the detection of discrete quantum-well states with inverse photoemission difficult due to its broad energy resolution.

5.4 Ni on Cu(001): Angular dependence

Electron confinement by a relative energy gap depends on the probing direction. IPE spectra have been measured as a function of the electron incidence angle θ in the [110] azimuth for the 6 ML Ni film on Cu(001) in order to study the energy vs. momentum relation in thin Ni films on Cu(001) (Renken et al. 2007). The spectra, displayed in figure 5.16, are normalized to equal background intensity. As the angle increases, the Ni-*d* feature just above the Fermi level remains at the same energy. The *IS* feature as well as the quantum-well states shift to higher energy up to an angle of about 30°. In addition, the first quantum-well state disappears, the third one shows up. At $\theta = 35°$, the dispersion behavior changes. The quantum-well-related spectral features now disperse to lower energy with increasing angle and change their character to a surface resonance (*SR*) as they approach the band-gap boundary. This kind of surface resonance was observed in IPE measurements on bulk Cu(001) and bulk Ni(001) and was theoretically confirmed (Graß et al. 1993, Starke et al. 1992*b*, Schneider et al. 1992). Furthermore, another spectral feature appears with negative dispersion identified as a well-known surface state (*SS*) in accordance with IPE data of bulk Ni(001) (Starke et al. 1992*b*). As expected for a surface state, its energy is independent of the Ni film thickness. It should be noted that

the surface state and the surface resonance were observed to be more sensitive to adsorbates than quantum well and bulk-derived spectral features, thus confirming their surface character.

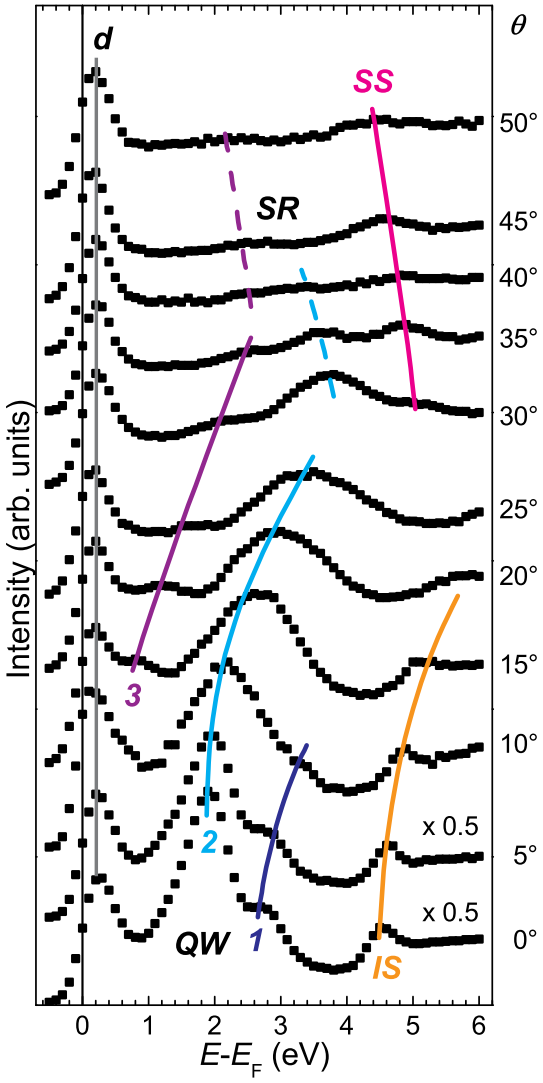

Figure 5.16: Inverse photoemission spectra (spin-averaged) of 6 ML Ni on Cu(001) as a function of the electron incidence angle θ in the [110] azimuth. Different spectral features can be identified as contributions from Ni d bands (d), quantum-well states (*QW 1,2,3*), crystal-induced surface resonances (*SR*), surface states (*SS*), and image-potential surface states (*IS*).

To summarize the dispersion behavior observed in the spectra of figure 5.16, an $E(\boldsymbol{k}_{\parallel})$ diagram is presented in figure 5.17, together with the projected bulk band structure of Ni(001) (Donath 1994). The variation of $\boldsymbol{k}_{\parallel}$ along the [110] direction corresponds to $\bar{\Gamma}\bar{X}$ in terms of the surface Brillouin zone. The non-hatched areas denote the calculated gaps of the Ni bulk band structure, projected onto the (001)

surface. The thin solid and dashed lines represent the majority and minority band-gap boundaries, respectively. The thick solid lines indicate two transitions into bulk-like states of Ni(001), labeled *d* and *sp*, according to their band character, and, furthermore, the Ni image-potential surface state *IS* and the crystal-induced surface state *SS* appearing in energy gaps. The circles and squares represent the peak positions of the spectra in figure 5.16. The Ni-*d* state of the 6 ML film shows no dispersion like the *d* state of bulk Ni(001) in the whole $\boldsymbol{k}_{\parallel}$ range. All surface-related features, the image-potential induced surface state, the crystal-induced surface state, and the surface resonance have the same dispersion behavior for the 6 ML Ni film as for bulk Ni(001) (Starke et al. 1992*b*, Schneider et al. 1992). The three quantum-well states *QW 1,2,3* exhibit similar dispersion behavior as the bulk *sp* transition, but with different energy shifts relative to the bulk *sp* transition. Upon approaching the band-gap boundary, the quantum-well states evolve into a surface resonance state. A similar phenomenon was observed for non-ferromagnetic Cu films on Co / Cu(001) (Yu and Donath 2003*a*). Moreover, the dispersion behavior of Fe / Cu(001) along the [110] direction is similar to the one of Ni, although it is not reported about quantum-well states in the early work (Glatzel et al. 1992). Anyway, the Fe dispersion shows a transition from quantum-well states to a surface resonance.

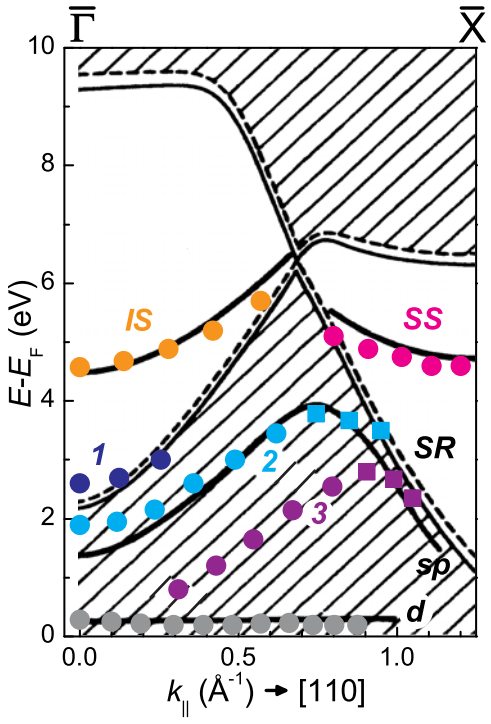

Figure 5.17: Energy dispersion as a function of the electron momentum parallel to the surface along the [110] direction, $E(k_{||})$, for 6 ML Ni on Cu(001). Colored circles and squares represent the spectral features shown in figure 5.16 as indicated. The non-hatched areas denote gaps of the projected Ni(001) bulk band structure, thin solid and dashed lines the majority and minority band-gap boundaries. Thick solid lines represent the energy dispersions of *d*- and *sp*-like bulk states, image-potential surface state *IS* and crystal-induced surface state *SS* of bulk Ni(001).

Chapter 6

Cu on Ni(001) and on Co(001)

In the present chapter, the electronic structure above the Fermi level of Cu films on both thin Ni and Co films, deposited each on the Cu(001) substrate, is investigated by spin- and angle-resolved inverse photoemission.

6.1 Electronic states of Cu films on Ni(001)

Concerning the energy dependence on the film thickness, the quantum-well states in a thin film typically shift up in energy with increasing film thickness. This behavior is reported on Cu on fcc Co (Ortega and Himpsel 1992, Ortega et al. 1993, Garrison et al. 1993, Li et al. 1995, Danese and Bartynski 2002), Cu on fcc Fe (Ortega and Himpsel 1992, Ortega et al. 1993, Danese et al. 2004*a*), as well as for Ni on Cu(001) (Himpsel and Rader 1995) (also see section 5.3), Co on Cu(001) (Yu et al. 2003*b*), Ag on Fe(001) (Smith et al. 1994), Ag on Au(001), and Au on Ag(001) (Chiang 2000). Furthermore, it is confirmed by the phase-accumulation model (see section 2.2.2). The only exceptions are spin-integrated inverse photoemission measurements on Cu films on Ni(001) (Himpsel and Rader 1995, Hwang and Himpsel 1995) and on Cu films on thin Ni films on Cu(001) (Danese et al. 2004*a*). In the latter case, it is reported about an *anomalous thickness dispersion* of the unoccupied quantum-well states in Cu films on Ni. With this, a shift down in energy with increasing Cu film thickness is meant. But the identification of the spectral features is not stringent. Moreover, in the same study the occupied energy levels of the Cu overlayer display the usual upward shift with increasing overlayer thickness. The origin of the *anomalous* energy shift is believed to be tied to an interaction of the Cu and Ni *sp* levels at the overlayer-film interface. In the present section, the true origin of the measured spectral features is identified. Furthermore, the reason for the energy shift of the spectral features is explained.

6.1.1 Cu on Ni / Cu(001): Thickness dependence

The coverage of a Ni film on Cu(001) with Cu on top reduces the thickness of the spin-reorientation transition (see section 3.2). This is shown in figure 6.1 presenting spin-resolved inverse photoemission spectra of n ML Cu / 6 ML Ni / Cu(001) at

normal electron incidence at $T = 100\,\mathrm{K}$. The spectra are normalized to equal spin-averaged intensity of the Ni-d peak maximum. In the lower part of the figure the Ni-d feature of uncovered 6 ML Ni on Cu(001) is displayed. For 0.25 ML Cu coverage, the spin-asymmetry is dramatically reduced. For 0.5 ML Cu coverage, the spin-asymmetry is almost reduced to zero. The rapid reduction of the spin asymmetry cannot be explained by the attenuation of the Ni-d transition by the Cu overlayer, because the attenuation length in Cu is about 10 ML for 10 eV electrons (Lindau and Spicer 1974, Yu and Donath 2003*a*) (see below). Hence, it is the thickness of the spin-reorientation transition that may be reduced to below 6 ML Ni due to a very low coverage of only 0.5 ML Cu, so that the film is already be magnetized out of plane. For this reason, only the spin-averaged inverse photoemission spectra of Cu films on Ni / Cu(001) are discussed in the following.

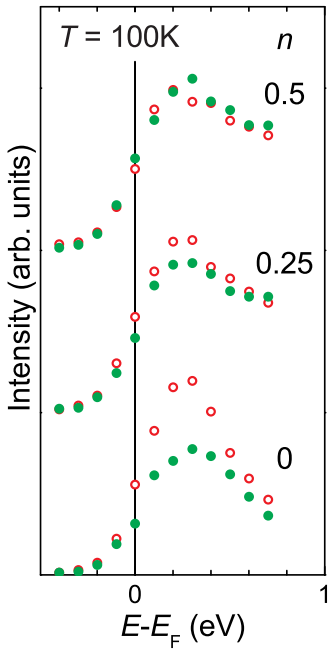

Figure 6.1: Spin-resolved inverse photoemission spectra of n ML Cu / 6 ML Ni / Cu(001) at normal electron incidence and $T = 100\,\mathrm{K}$. The spin asymmetry of the Ni-d feature rapidly decreases with increasing Cu coverage owing to the reduced thickness of the spin reorientation transition.

The dependence of the IPE spectra at normal electron incidence on the Cu film thickness n for a fixed Ni thickness of 6 ML on Cu(001) is presented in detail in figure 6.2. The left-hand side of the figure shows the spin-averaged spectra for $0 \leq n \leq 4$. The right-hand side shows the spectra for $4 \leq n \leq 20$ as well as the spectrum for pure Cu(001). The spectra are normalized to equal background intensity at an energy of 3.7 eV, but the scaling in the two parts of the figure is different. The yellow hatched area indicates the energy range between the Fermi level and $E^{Cu}_{X_{4'}} = 1.80\,\mathrm{eV}$, in which quantum-well resonances in Cu as well as in Ni may be detected. The yellow area indicates the energy range between $X^{Cu}_{4'} = 1.80\,\mathrm{eV}$ and $X^{Ni}_{4'} = 2.76\,\mathrm{eV}$ (spin-

averaged), in which the formation of true quantum-well states in Ni is possible. The peak positions of the individual features are accentuated by the colored marks: The Ni-*d* bulk feature and the image-potential-induced surface state *IS* by black marks, the quantum-well features of Ni by red marks and the ones of Cu by orange marks, and the Cu-*sp* feature by blue marks.

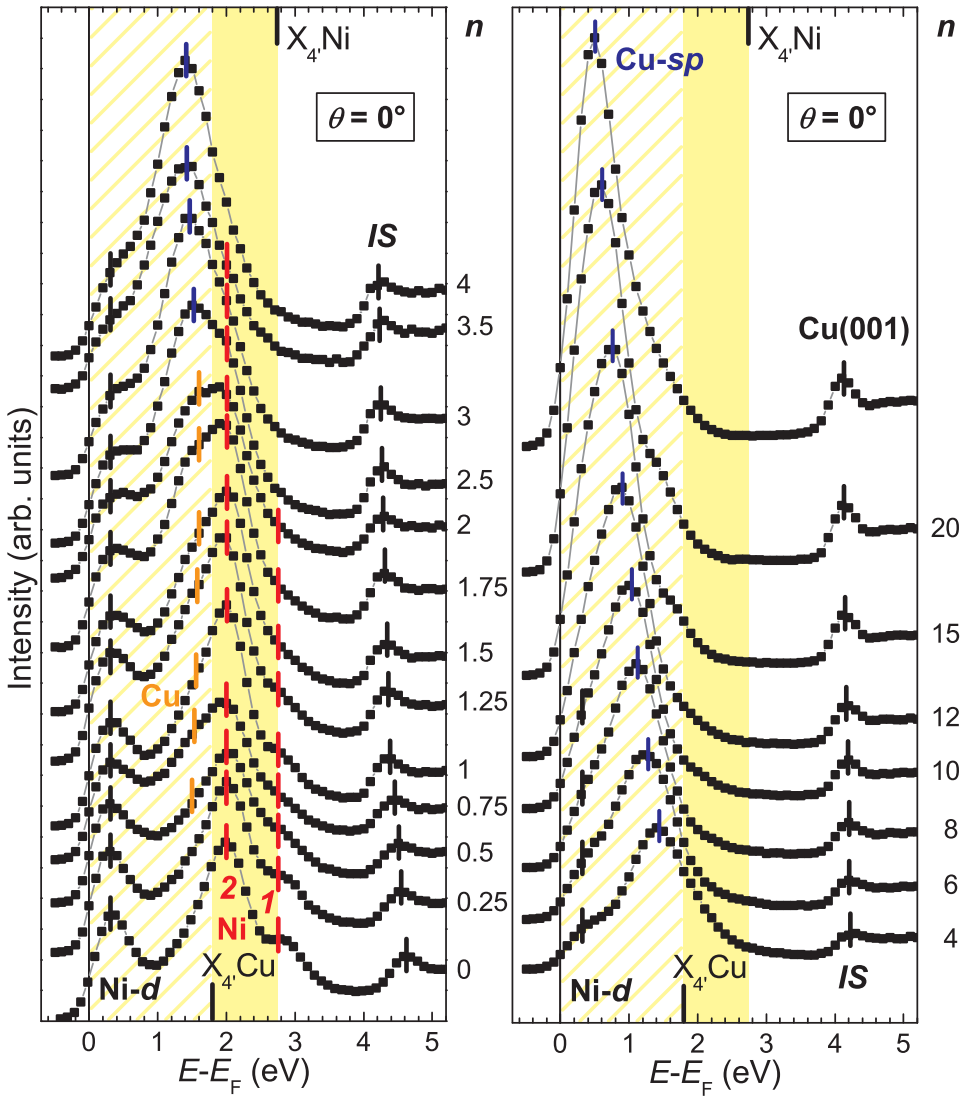

Figure 6.2: Spin-averaged inverse photoemission spectra of n ML Cu / 6 ML Ni / Cu(001) at $\theta = 0°$, showing the thickness dependence of the Ni-*d* bulk feature, the quantum-well features of Ni and Cu and the Cu-*sp* bulk feature, respectively, and the image-potential-induced surface state *IS*. The spectra are normalized to equal background intensity. See text for details.

The spectrum of uncovered 6 ML Ni on Cu(001) is once more presented in the lower part of the left-hand side of figure 6.2, showing the Ni-*d* bulk feature, the first and the second quantum-well feature of Ni, Ni-*1* and -*2*, and the image-potential-induced

surface state *IS*. With increasing Cu coverage, the energy of the Ni-*d* feature at 0.25 eV does not change. The bulk state does not depend on surface and overlayer conditions. The Ni-*d* state shows clearly up as a peak up to 2 ML and as a shoulder up to 10 ML Cu coverage. This is consistent with the attenuation length of about 10 ML for 10 eV electrons in Cu (Lindau and Spicer 1974, Yu and Donath 2003*a*). The intensity of the Ni-*d* feature slightly decreases up to 4 ML Cu coverage due to the attenuation of the Ni *d*-band transition by the Cu overlayers. For higher Cu coverage, the Ni-*d* feature becomes superimposed by the Cu-*sp* feature (see below). The image-potential-induced surface state *IS* continuously shifts to lower energies with increasing Cu film thickness owing to the change in work function. Furthermore, its high intensity reflects the good film growth of the Cu films grown on 6 ML Ni / Cu(001).

Concerning the quantum-well features, the first Ni quantum-well feature, Ni-*1*, still appears in the spectra up to 2 ML Cu coverage as a shoulder at the high-energy side of the second Ni quantum-well feature, Ni-*2*. For even higher Cu coverage, there is still some intensity from the Ni-*1* transition, but a peak position cannot be determined any more. The energy position of Ni-*1* does not change with increasing Cu coverage. First, the thickness of the Ni film stays constant, not giving any reason for a change in energy. Second, the boundary of the quantum well changes from Ni-vacuum to Ni-Cu. But as figure 6.2 shows, this hardly influences the energy level of the quantum-well state. The intensity of Ni-*1* slightly decreases with increasing Cu coverage, likewise owing to the attenuation by the Cu overlayer. The second Ni quantum-well feature appears up to 2 ML Cu coverage as a clear peak and up to 3.5 ML Cu coverage as a shoulder at the feature at lower energy, which results from transitions into the Cu overlayer (see below). The latter also influences the intensity of Ni-*2*, which is why its decrease with increasing Cu coverage can only be observed for very low Cu coverage. Concerning the stronger attenuation of Ni-*1* compared to Ni-*2* and even stronger compared to Ni-*d*, without hybridization this may reflect the trend that the attenuation length decreases with increasing energy in this energy range according to the *universal curve* (see section 4.1.1). Both Ni-*1* and Ni-*2* are true quantum-well states with energies between $X_{4'}^{Cu}$ and $X_{4'}^{Ni}$. In contrast, the third quantum-well state, having an energy below $X_{4'}^{Cu}$, is a quantum-well resonance. According to the phase-accumulation model, its energy for 6 ML Ni on Cu(001) is about 1.3 eV (see section 5.3). The corresponding spectrum shows only a small shoulder at this energy, but the influence of the third quantum-well state is clearly recognizable.

With increasing Cu coverage, another feature shows up from 0.5 ML Cu coverage below $X_{4'}^{Cu}$ as a shoulder at the low-energy side of the second Ni quantum-well feature. Below 1 ML Cu coverage this feature appears at an energy of about 1.5 eV. But for more than 1 ML Cu coverage, it shifts to higher energies, namely towards $X_{4'}^{Cu}$, with increasing Cu coverage, in contrast to the Ni quantum-well features, whose energies do not show any dependence on the Cu coverage. As a consequence, this feature can be identified as Cu quantum-well resonance. For 1 ML Cu coverage, the Cu quantum-well resonance is already slightly shifted higher in energy compared to 0.5 ML Cu coverage. This can be attributed to the film growth producing also islands which are already 2 ML thick, leading to a higher energy of the Cu quantum-well resonance. The Cu quantum-well resonance appears up to 2 ML Cu coverage.

For this thickness, it already shows up as a peak in the spectrum having about the same intensity as the second Ni quantum-well state and an energy of 1.6 eV. By this, the energy is a little higher than for 2 ML Cu on 5 ML Co / Cu(001) (see Yu and Donath (2003*a*) and section 6.2). For the latter, it is also the quantum-well resonance in the underlying Co, which is superimposed by the first quantum-well resonance in Cu. To sum up it can be said that, up to 2 ML Cu film thickness, the Cu quantum-well resonance shows the expected behavior: Like all quantum-well features, also the Cu quantum-well resonance shifts up in energy with increasing film thickness. There is no *anomalous thickness dispersion* for quantum-well states in Cu on Ni(001) as reported before by Danese et al. (2004*a*).

Nevertheless, for a coverage above 2.5 ML Cu, the behavior of the observed Cu feature changes. From now on its energy shifts to lower energies with increasing Cu coverage. Above 3.5 ML Cu coverage, only one big feature appears besides the Ni-*d* feature. In detail, this Cu feature shifts from 1.5 eV for 2.5 ML Cu to 0.6 eV for 20 ML Cu (right-hand side of figure 6.2). For comparison, the bulk Cu-*sp* transition appears at 0.5 eV. Furthermore, the intensity of the Cu feature strongly increases with increasing Cu coverage. For 2 ML Cu coverage, the signal-to-background ratio for the Cu quantum-well resonance only amounts to $s/b = I(1.6\text{eV})/I(3.7\text{eV}) = 6.2$. In contrast, for the Cu feature at higher Cu coverage, it is $s/b = I(1.4\text{eV})/I(3.7\text{eV}) = 9.7$ for 4 ML Cu and $s/b = I(0.6\text{eV})/I(3.7\text{eV}) = 26.5$ for 20 ML Cu. For bulk Cu-*sp*, it is $s/b = I(0.5\text{eV})/I(3.7\text{eV}) = 28.0$. Above 12 ML Cu coverage, also the Cu crystal-induced surface resonance at the high-energy side of the Cu-*sp* feature shows up.

Hence, the behavior of the Cu feature, concerning decrease in energy as well as increase in intensity, reflects the transition of discrete quantum-well resonances to the continuous Cu-*sp* bulk band. On the one hand, the Cu quantum-well resonances converge towards $X_{4'}^{Cu} = 1.8\,\text{eV}$. On the other hand, the bulk Cu-*sp* transition appears at 0.5 eV. Therefore, there is a shift to lower energy with increasing Cu coverage when the three-dimensional bulk band structure is formed. For Cu on Ni, this already influences the spectral features at a very low Cu coverage from 2.5 ML. Moreover, in the end more than 20 ML Cu are required to form the Cu-*sp* bulk band structure.

For comparison, for Ni on Cu(001) the typical shift of the quantum-well states to higher energy with increasing Ni film thickness shows up up to 15 ML Ni. The Ni-*sp* band is formed at 80 ML Ni (see section 5.3). For Ni on Cu, the energy difference between $X_{4'}^{Ni}$ and the Ni-*sp* bulk transition amounts to about 1.0 eV. In contrast, for Cu on Ni the energy difference between $X_{4'}^{Cu}$ and the Cu-*sp* bulk transition amounts to about 1.3 eV. Hence, the broader energy range for Cu on Ni results in a larger energy shift. The *sp*-band is formed at a much lower film thickness for Cu on Ni / Cu(001) than for Ni on Cu(001). One possible reason may be a coupling of the Cu film with the underlying Cu(001) substrate. But even for 100 ML Ni interlayer thickness the Cu-*sp* transition appears at about 0.5 eV for about 20 ML Cu overlayer thickness (Danese et al. 2004*a*). Furthermore, a coupling between the Cu and Ni *sp*-bands is not likely, because then the Ni *sp*-band would be influenced by the underlying Cu(001) substrate, too. Another possible reason may be a coupling between the *sp*-levels of the Cu overlayer with the *d*-levels of the Ni interlayer at the

interface. However, hybridization between Ni and Cu mainly occurs at the interface (see section 3.5.1).

The transition from quantum-well states to bulk transitions also shows up for higher parallel electron momenta. Figure 6.3 displays spin-averaged IPE spectra of n ML Cu / 6 ML Ni / Cu(001) at $\theta = 25°$ with $0 \leq n \leq 4$ on the left-hand side and $4 \leq n \leq 20$ as well as pure Cu(001) on the right-hand side. The spectra are normalized to equal background intensity. The projected bulk band structures of Cu and Ni depend on the electron momentum and thus on the angle of electron incidence (see figure 6.5 below). At $\theta = 25°$, the lower edge of the Cu band gap is at 4.6 eV (Braun 2005). It is true that the lower edge of the Ni band gap is at 6.5 eV (spin-averaged), but the upper edge of the Cu band gap is already at 5.0 eV. Consequently, only in the very narrow energy range between 4.6 eV and 5.0 eV, indicated by the yellow area, true quantum-well states in Ni may form. Quantum-well resonances in Cu as well as in Ni may show up below 4.6 eV as well as between 5.0 eV and 6.5 eV.

In the lower part of the left-hand side of figure 6.3 the spectrum of uncovered 6 ML Ni on Cu(001) is presented, showing the Ni-d bulk feature and the second and the third quantum-well features of Ni, *2* and *3* (see also section 5.4). In contrast to $\theta = 0°$, the spectral features appear much broader at $\theta = 25°$. For the latter the dispersion $E(\boldsymbol{k}_{\parallel})$ shows a higher gradient, thus the uncertainty in $\boldsymbol{k}_{\parallel}$ results in a higher uncertainty in energy. With increasing Cu coverage, the energy of the Ni-d feature at 0.25 eV stays constant, and its intensity again decreases due to the attenuation by the Cu overlayers. At first sight, the broad Ni quantum-well feature *2* seems to shift slightly to lower energy with increasing Cu coverage. But for little Cu coverage, this feature is that broad, that it may contain contributions from transitions into Cu states as well. These Cu quantum-well resonances are expected to have energies below the lower edge of the Cu band gap at 4.6 eV and thus lower than the true Ni quantum-well states. Furthermore, the intensity of the Ni quantum-well states decreases with increasing Cu coverage due to the attenuation by the Cu overlayer. Consequently, this may shift the overall observed feature in the yellow area to lower energy with increasing Cu coverage. Up to 2 ML Cu coverage, there is only a slight shift in energy with increasing Cu coverage. But above 2 ML Cu coverage, the thickness dependence becomes stronger. The feature shifts to lower energy and further strongly increases in intensity.

Also above 2 ML Cu coverage, another feature shows up at about 1.5 eV, which shifts to higher energy with increasing coverage. Its contribution to the spectra can be observed up to 10 ML Cu coverage. The energy of this feature increases with increasing Cu coverage, thus it can be identified as Cu quantum-well resonance. In contrast to $\theta = 0°$, this is not the $n = 1$ quantum-well resonance, but one of higher order (see section 6.1.2).

The Cu quantum-well resonance, which shifts upwards in energy with increasing Cu coverage, and the broad feature, which contains contributions from Ni as well as from Cu for low Cu coverage and shifts downwards in energy, result in one big feature above 10 ML Cu coverage. This feature further shifts to lower energy until it reaches the energy of the Cu-sp transition, 1.6 eV, for 20 ML Cu coverage. As at $\theta = 0°$, this again shows the transition of discrete quantum-well resonances into the

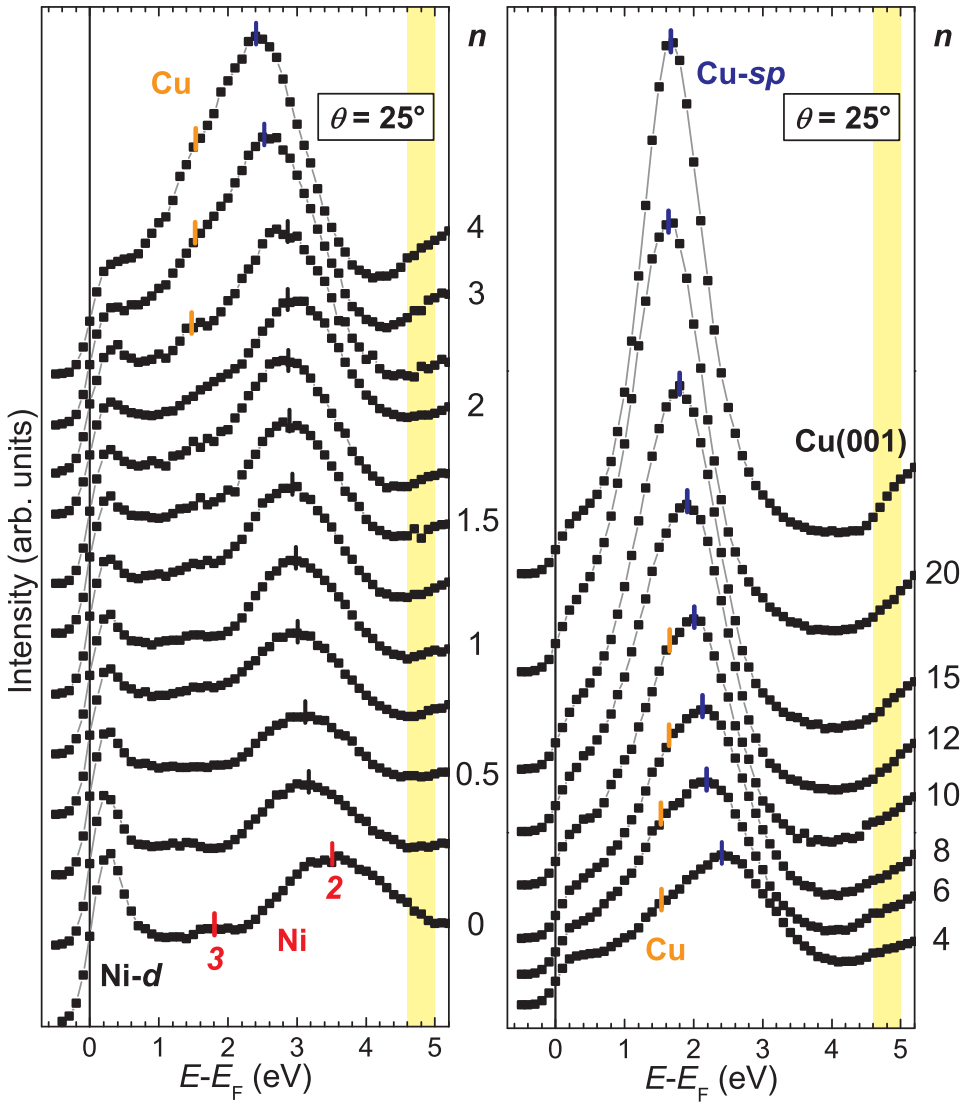

Figure 6.3: Spin-averaged inverse photoemission spectra of n ML Cu / 6 ML Ni / Cu(001) at $\theta = 25°$, showing the thickness dependence of the Ni-d bulk feature and the quantum-well features of Ni and Cu and the Cu-sp bulk feature, respectively. The spectra are normalized to equal background intensity. Compared to $\theta = 0°$, the QW features appear much broader. See text for details.

continuous Cu-sp bulk band.

6.1.2 Cu on Ni / Cu(001): Angular dependence

As for 6 ML Ni / Cu(001) (see section 5.4), IPE spectra have been measured as a function of the electron incidence angle θ in the [110] azimuth for 2 ML Cu / 6 ML Ni / Cu(001) in order to study the energy vs. momentum relation in this bilayer structure on Cu(001). The spin-averaged spectra, normalized to equal background intensity,

are displayed in figure 6.4. Some spectra are reduced by the given factors for easier representation. In the lower part of the figure the spectrum at normal electron incidence is presented one more time, showing the Ni-*d* feature just above the Fermi level, the Ni quantum-well features Ni-*1, 2*, the Cu quantum-well feature Cu-*1*, and the Cu image-potential surface states (*IS*). With increasing angle, the Ni-*d* feature remains at the same energy. The Cu *IS* feature shifts to higher energy and appears in the spectra up to $\theta = 18°$. The first Ni quantum-well state, Ni-*1*, appears as a shoulder at the high-energy side of the big feature resulting from Ni-*2* and Cu-*1* at lower energy. A peak position cannot be determined at angles above $\theta = 0°$. The feature resulting from transitions into the second Ni quantum-well state, Ni-*2*, as well as into the Cu quantum-well resonance, Cu-*1*, shifts to higher energy up to an angle of about 35°. In addition, the third Ni quantum-well feature, Ni-*3*, appears in the range from 10° up to about 40° and also shifts to higher energy. To identify this feature originating from the Ni film and not from the Cu overlayer, the $E(\boldsymbol{k}_{\|})$ diagram has to be studied (see below). As for the Ni quantum-well states in 6 ML Ni / Cu(001), the dispersion behavior changes above 35°. The spectral features labeled *SR* and *SS*, again crystal-induced surface resonance and surface state, respectively, now shift to lower energy with increasing angle.

In figure 6.5 the dispersion behavior of the spectral features from figure 6.4 is shown in an $E(\boldsymbol{k}_{\|})$ diagram, with $\boldsymbol{k}_{\|}$ along the [110] direction corresponding to $\bar{\Gamma}\bar{X}$ in terms of the surface Brillouin zone. The circles and squares represent the peak positions of the corresponding spectral features in figure 6.4. The non-hatched areas represent gaps of the projected Ni(001) bulk band structure, thin solid and dashed lines the majority and minority band-gap boundaries, thick solid lines the energy dispersions of *d*- and *sp*-like bulk states, image-potential surface state *IS* and crystal-induced surface state *SS* of bulk Ni(001). The solid blue lines denote the band-gap boundaries of the projected Cu(001) bulk band structure (Braun 2005). The area between the respective upper and lower solid blue line represents the band gap.

The Ni-*d* state shows the same non-dispersive behavior in the whole $\boldsymbol{k}_{\|}$ range than for 6 ML Ni / Cu(001) and, consequently, than for the *d* state of bulk Ni(001) (see section 5.4). There is no influence by the Cu overlayer. The surface state *IS* exactly follows the dispersion of the image-potential-induced surface state of bulk Cu(001) (Graß et al. 1993). Also the surface state *SS* follows the dispersion of the crystal-induced surface state of bulk Cu(001), but is slightly shifted to higher energy. A similar shift has been reported for 2 ML Cu / 5 ML Co / Cu(001) (Yu and Donath 2003*a*). The three quantum-well states of the Ni intervening film, Ni-*1, 2, 3*, in 2 ML Cu / 6 ML Ni / Cu(001) almost perfectly match the dispersion of the quantum-well states of the Ni overlayer film in 6 ML Ni/ Cu(001). Small discrepancies may be due to the difficult estimation of the spectral peak positions, because the Ni spectral features are influenced by the Cu spectral quantum-well feature. Moreover, the transition from quantum-well states to surface resonances at the band-gap boundary shows up for the third Ni quantum-well state, Ni-*3*, similar to 2 ML Cu / 5 ML Co / Cu(001) (Yu and Donath 2003*a*). Besides, the Ni quantum-well states converge towards the Ni band-gap boundary. In contrast, the Cu quantum-well state, which shows up at energies slightly below the second Ni quantum-well state, converges towards the Cu band-gap boundary. Especially, it does not appear

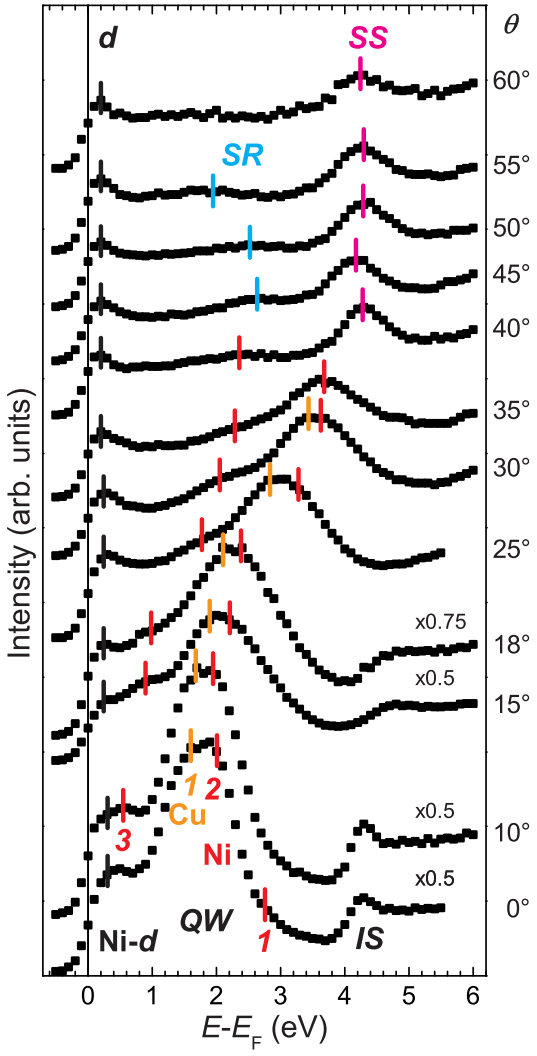

Figure 6.4: Inverse photoemission spectra (spin-averaged) of 2 ML Cu / 6 ML Ni / Cu(001) as a function of the electron incidence angle θ in the [110] azimuth. The spectra are normalized to equal background intensity and some are reduced by the given factors. The spectral features are indicated as contributions from Ni d bands (Ni-d), quantum-well states from Ni-(Ni-*1, 2, 3*) and Cu (Cu-*1*), crystal-induced surface resonances (*SR*), surface states (*SS)*, and image-potential surface states (*IS*).

in the area between the Cu and the Ni band-gap boundaries. Therefore, it may be identified originating from the Cu overlayer. In addition, it may be identified as Cu electronic state owing to the dependence on the thickness of the Cu overlayer (see above).

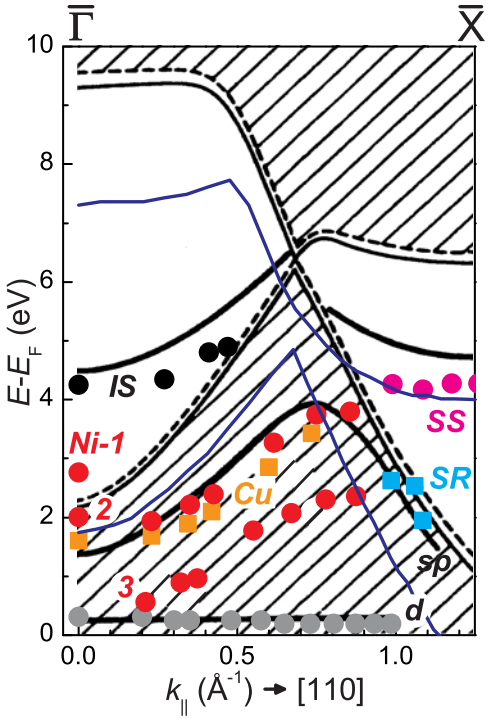

Figure 6.5: Energy dispersion as a function of the electron momentum parallel to the surface along the [110] direction, $E(k_{||})$, for 2 ML Cu / 6 ML Ni / Cu(001). Colored circles and squares represent the spectral features shown in figure 6.4 as indicated. The non-hatched areas denote gaps of the projected Ni(001) bulk band structure, thin solid and dashed lines the majority and minority band-gap boundaries. Thick solid lines represent the energy dispersions of *d*- and *sp*-like bulk states, image-potential surface state *IS* and crystal-induced surface state *SS* of bulk Ni(001). The solid blue lines denote the band-gap boundaries of the projected Cu(001) bulk band structure.

6.2 Electronic states of Cu films on Co(001)

For Cu on Co / Cu(001), so far the dispersion of 2 ML Cu / 5 ML Co / Cu(001) has been reported as well as the thickness dependence of the transitions into Co *d* bands for *n* ML Cu / 5 ML Co / Cu(001) at normal incidence (Yu and Donath 2003*a*). In this section, the thickness dependence of the Cu quantum-well states as well as of the Cu surface states is presented.

6.2.1 Cu on Co / Cu(001): Quantum-well states

The dependence of the quantum-well states on the Cu film thickness is displayed in figure 6.6, showing spin-averaged IPE spectra (left-hand side) as well as spin-resolved spectra (right-hand side) of *n* ML Cu on 5 ML Co / Cu(001), $0 \leq n \leq 10$, at an electron incidence angle of $\theta = 25°$. The spectra are normalized to equal spin-averaged background intensity at an energy of 4.3 eV. At $\theta = 25°$, the lower edge of the Co band gap is at 5.8 eV (spin-averaged) (Braun 2005). Thus as for Ni, only in

a narrow energy range between 4.6 eV and 5.0 eV, indicated by the yellow area, also true quantum-well states in Co may form. Quantum-well resonances in Cu as well as in Co may show up below 4.6 eV as well as between 5.0 eV and 5.8 eV. The peak positions of the individual features are accentuated by the colored marks: The Co-*d* bulk feature, which originates from transitions into Co *d* bands, by black marks, the Co quantum-well feature by red, black, and blue marks, and the Cu quantum-well feature by orange marks for the spin-averaged spectra. For the spin-resolved spectra, the corresponding peak positions are accentuated by green marks for majority spin and by red marks for minority spin.

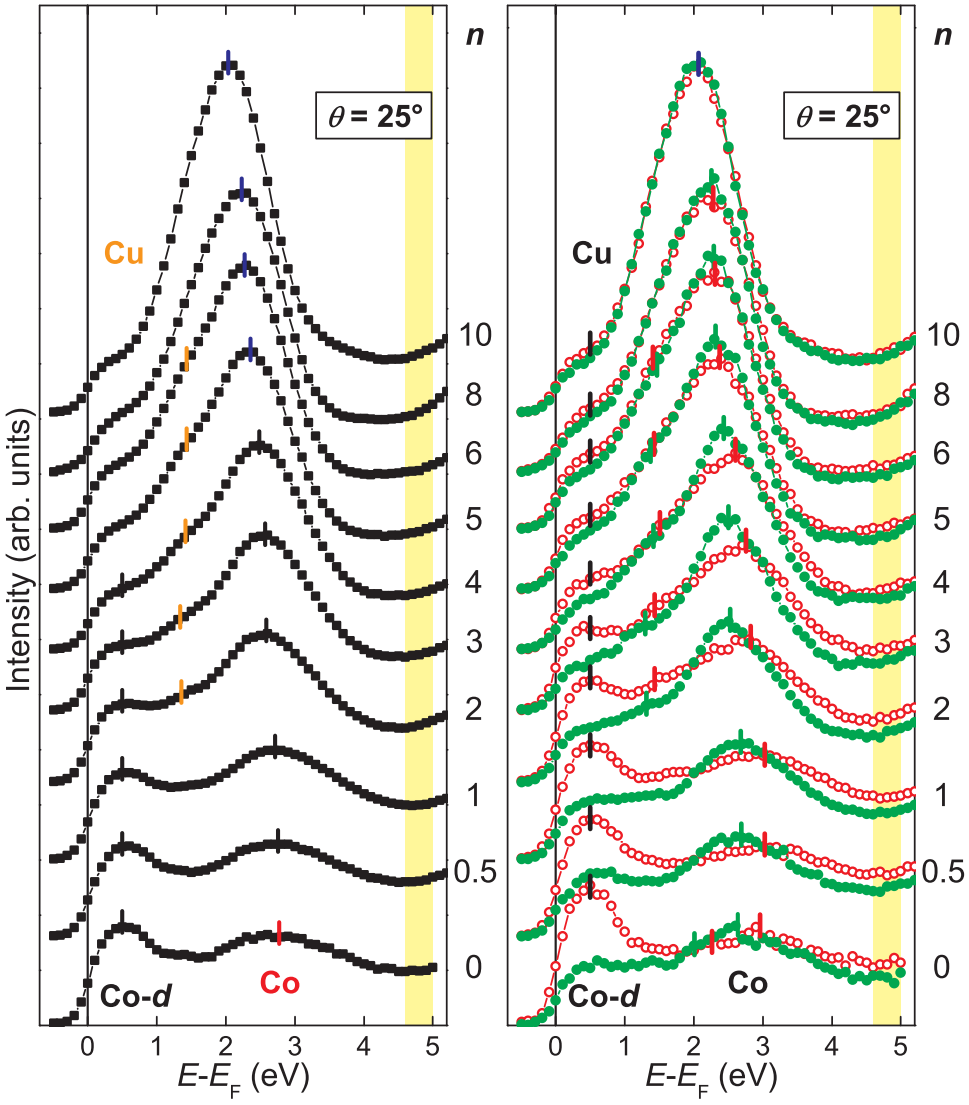

Figure 6.6: Spin-averaged (left-hand-side) and spin-resolved (right-hand-side) inverse photoemission spectra (green for majority spin, red for minority spin) of n ML Cu / 5 ML Co / Cu(001) at $\theta = 25°$, showing the thickness dependence of the Co-*d* bulk feature and the quantum-well features of Co and Cu. The spectra are normalized to equal spin-averaged background intensity.

In the lower part of the figures, the spectra for 5 ML Co / Cu(001) is presented, showing the Co-*d* bulk feature as well as Co quantum-well features. The spin-averaged spectrum only shows one broad feature, but the spin-resolved spectra show two clearly spin-split Co quantum-well features. With increasing Cu coverage, the Co-*d* state remains at the same energy during the whole thickness range, but gets weakened in intensity owing to the attenuation by the Cu overlayer. For 10 ML Cu coverage, it is nearly vanished, only a very small spin asymmetry is left. This is in accordance with the mean-free path of Cu. The same behavior has been observed for the attenuation of the Ni-*d* feature (see section 6.1.1). Concerning the quantum-well states, the spin-averaged spectra show that the one broad quantum-well feature remains at the same energy up to 1 ML Cu coverage, but then slightly shifts to lower energy with increasing Cu coverage. This again may be due to the influence of Cu quantum-well features, which, according to the Cu bulk band structure, are expected to appear at lower energy. Above 5 ML Cu coverage, the energy shift with increasing coverage becomes stronger. In addition, another feature appears from 2 ML Cu coverage at lower energy. In comparison with *n* ML Cu / 6 ML Ni / Cu(001), $\theta = 25°$, this feature may be identified as Cu quantum-well resonance. It shows the typical quantum-well-like behavior: It shifts up in energy with increasing Cu coverage. Above 7 ML Cu coverage, this Cu feature and the feature at higher energy become one total feature, which shifts to lower energy with increasing Cu coverage. As for *n* ML Cu / 6 ML Ni / Cu(001), in this thickness range the transition of discrete quantum-well resonances to the continuous Cu-*sp* bulk band starts.

The spin-resolved spectra show only one broad quantum-well feature from 0.5 ML Cu coverage. The estimation of the peak positions of a second feature at lower energy is hardly possible within the statistical error. With increasing Cu coverage, the spin splitting and the spin asymmetry of the Co quantum-well feature at higher energy decrease. The spin splitting is reduced to zero at about 6 ML Cu coverage, the spin asymmetry vanishes above 8 ML Cu coverage. This would correspond with the attenuation length in Cu if this feature originated from the underlying Co film only. But it also contains contributions from the Cu overlayer, as the shift to lower energy shows. Furthermore, the Cu quantum-well feature is strongly spin-dependent. But as for the Co quantum-well feature, spin splitting and spin asymmetry decrease with increasing Cu coverage. Above 4 ML Cu coverage, the spin-dependence of the Cu quantum-well feature is almost lost. This reflects the decoupling of the electron wave function in the Cu overlayer from the underlying ferromagnetic Co layer at the Cu-Co interface at about 4 ML Cu coverage. It is no longer the spin-dependent reflection at the Cu-Co interface which results in discrete two-dimensional spin-polarized quantum-well states. Instead, the formation of the continuous three-dimensional spin-independent Cu *sp* band begins.

6.2.2 Cu on Co / Cu(001): Surface states

An *sp*-derived crystal-induced surface state, which is related to the $L_{2'} - L_1$ energy gap of the bulk electronic structure, appears near the $\bar{X}$ symmetry point for the (001) surfaces of fcc crystals (Goldmann et al. 1985). In the present work, this surface state has been measured for Ni / Cu(001) (see section 5.4) and Cu / Ni / Cu(001) (see section 6.1.2). Both the Ni and the Cu surface state show the same energy

dispersion behavior along the [110] direction as the surface states of the Ni and Cu bulk (001) surfaces, respectively. Whereas the surface state further appears for fcc Fe on Cu(001) (Gubanka et al. 1996*a*), so far it is not reported about a crystal-induced surface state for Co(001). The latter is addressed in detail in this section.

For comparison of the respective crystal-induced surface states, IPE spectra of Cu(001) (T_R), Ni(001) ($T = 340\,\mathrm{K}$) (Starke et al. 1992*a*), 6 ML Fe / Cu(001) ($T = 90\,\mathrm{K}$) (Gubanka et al. 1996*a*, Gubanka et al. 1996*b*), and 5 ML Co / Cu(001) (T_R) are presented at $\theta = 50°$ in figure 6.7. The spin-integrated spectra, shown on the left-hand side of figure 6.7, are not normalized. All spectra show a crystal-induced surface state *SS* at an energy between 3.5 and 5.0 eV. Its intensity is highest for Cu, followed by Ni and Fe. For Co, the intensity is much lower, and the surface state only appears as slight increase in intensity. The low intensity makes the Co surface state difficult to measure (see below). The spectra further contain *sp*-derived surface features *SR* between 1.5 and 3.0 eV. Moreover, the spectra of the magnetic Ni, Fe, and Co show features related to transitions into the respective bulk *d* bands. Spin-resolved spectra of the Ni and Fe surface state are presented on the right-hand side of figure 6.7. Since the wave function of the surface state is confined within the topmost atomic layers, investigating the magnetic exchange splitting of the surface state is a surface-sensitive probe of magnetic properties. Close to $\bar{X}$ at $\theta = 50°$, the exchange splitting is 0.92 eV at $T = 90\,\mathrm{K}$ ($T/T_\mathrm{C} = 0.35$) for the Fe and 0.18 eV at $T = 340\,\mathrm{K}$ ($T/T_\mathrm{C} = 0.54$) for the Ni surface state.

Concerning fcc Co, the spin-resolved dispersion of the crystal-induced surface state along the [110] direction has been calculated by Braun (2005). Figure 6.8 presents an $E(k_\parallel)$ contour plot for calculated (inverse) photoemission densities of Co(001) along [110] for a photon energy of $\hbar\omega = 9.4\,\mathrm{eV}$. Dark regions represent high values of spectral density, whereas the yellow pattern indicate nearly zero intensity. The calculation is done by using an improved formulation of the one-step model of photoemission within a spin-polarized, fully relativistic framework (Braun and Donath 2004). By this calculation, the Co surface state is predicted to show up near the $\bar{X}$ symmetry point between 5.0 and 6.5 eV. The spin splitting is expected to amount to about 0.6 eV in the dispersion minimum.

It has turned out that it is very difficult to measure the Co surface state with inverse photoemission. The probability for transitions into the surface state is very low. Therefore, it needs a lot of spectra and many sample preparations to sum up. A lot of different methods for the film preparation have been tried out. Co layers have been evaporated at room temperature and at low temperature with and without subsequent annealing. The importance of an integer number of monolayers has been checked. However, a clear dependence of the spectral intensity on the sample preparation has not been found. The surface quality has been checked by AES and LEED. The existence of image-potential induced surface states and quantum-well states indicates a good surface quality and the existence of a flat surface. Furthermore, Co films have been investigated by scanning tunneling microscopy (STM) in another vacuum system. For this, another but similar Cu(001) substrate has been used. Figure 6.9 shows an STM picture of 5.0 ML Co / Cu(001) grown at room temperature without subsequent annealing. The $(100\,\mathrm{nm})^2$ picture shows three steps. Each step contains 60 % of the average film thickness and 20 % of +1 ML and −1 ML,

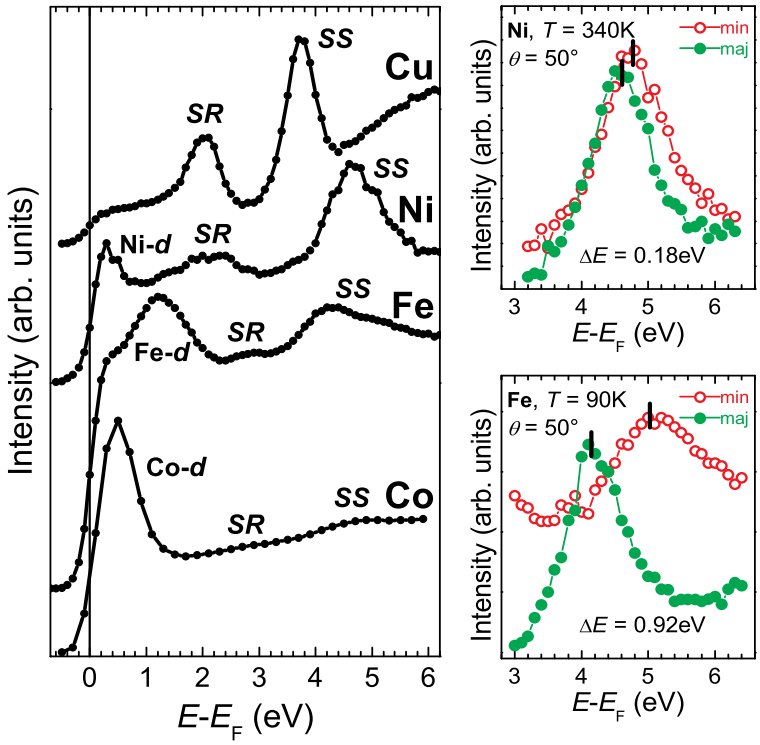

Figure 6.7: Inverse photoemission spectra of Cu(001) (T_R), Ni(001) (T = 340 K) (Starke et al. 1992*a*), 6 ML Fe / Cu(001) (T = 90 K) (Gubanka et al. 1996*b*), and 5 ML Co / Cu(001) (T_R) at $\theta = 50°$ to compare the respective surface states *SS*.

respectively. The area of average thickness may be increased to more than 70 % by subsequent annealing. By this, roughness of the Co film may not be responsible for the low spectral intensity of the surface state.

Spin-resolved IPE spectra of 5 ML Co on Cu(001) at $\theta = 50°$ are presented in figure 6.10. The spin-integrated spectrum is shown as well. The same spin-averaged linear background has been subtracted from all spectra, and the spectra are normalized to the background intensity. The spin-integrated spectrum clearly shows the Co crystal-induced surface state at an energy of 4.7 eV. Furthermore, the surface resonance state appears at about 2.9 eV. The peak positions have been determined by fitting Gaussian line shapes to the spectral features, which are shown as blue solid line. Even though both states are weak in intensity, they appear in many single spectra from different measurements and different sample preparations. In the spin-resolved spectra, there is hardly any spectral feature recognizable for minority spin. The intensity may be slightly higher in a broad range between about 3.5 and 5.5 eV. However, the surface state results in a clearly visible spectral feature in the majority spin spectrum. The same is true for the surface resonance.

The direction of the dipole axis of transition into the Co surface state can be estimated by different geometrical arrangements of the IPE set-up as described in the following. The intensity of the Co surface state depends on the angle of photon

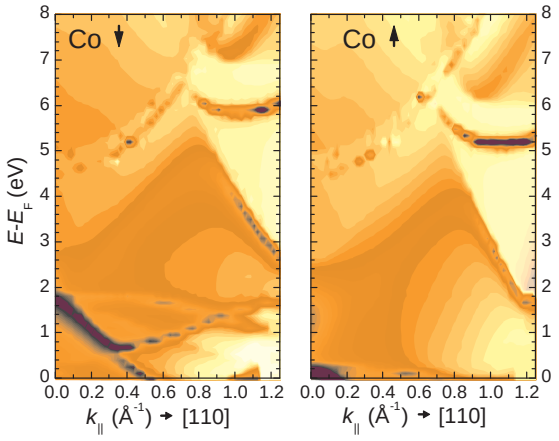

Figure 6.8: Contour plot $E(k_{||})$ of calculated minority (left-hand side) and majority (right-hand side) (inverse) photoemission spectral densities of Co(001) along [110] for a photon energy of $\hbar\omega = 9.4\,\mathrm{eV}$ (Braun 2005). Values of high spectral density are indicated by dark regions.

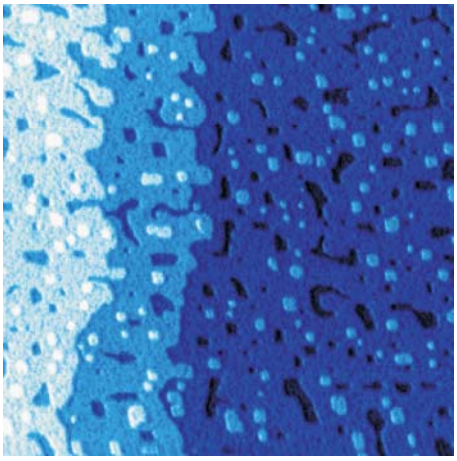

Figure 6.9: Scanning tunneling microscopy picture of 5 ML Co / Cu(001), $(100\,\mathrm{nm})^2$ (Bachmann 2003).

detection. The photon take-off angle is correlated with the electron incidence angle. The geometrical arrangement of the IPE set-up is shown in figure 6.11. The angle of electron incidence is $\theta = 45°$. The two photon counters are mounted at 35° and 70° with respect to the direction of electron incidence. This corresponds to photon take-off angles of $\alpha = -10°$ and $\alpha = 25°$, respectively. At $\theta = -45°$, the emitted photons can only be detected by the 35° photon counter. Thus, the photon take-off angle is $\alpha = 80°$. This situation is symmetrically identical to $\theta = 45°$, $\alpha = -80°$, and a photon counter at $-35°$ as shown in figure 6.11.

IPE spectra of 5 ML Co on Cu(001) at $\theta = -45°$ are presented in figure 6.12. For higher negative angles of electron incidence, the overall photon intensity becomes very low. The same spin-averaged linear background has been subtracted from all spectra, and the spectra are normalized to the background intensity. In the spin-integrated spectrum, the surface state appears at 4.3 eV. Compared to $\theta = 50°$, at

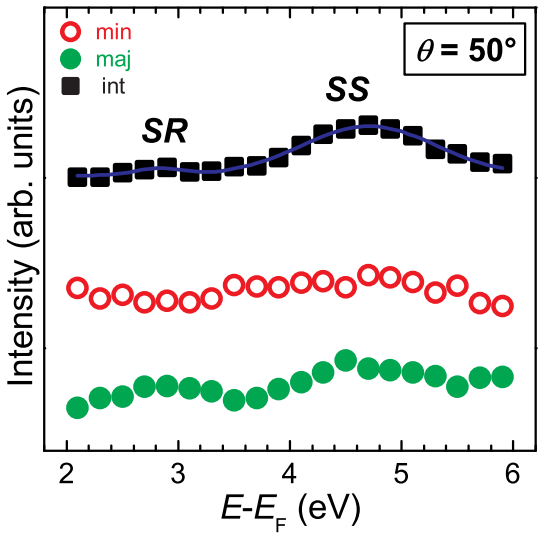

Figure 6.10: Inverse photoemission spectra of 5 ML Co / Cu(001) at $\theta = 50°$, showing the Co crystal-induced surface resonance *SR* and the surface state *SS*.

$\theta = -45°$ the intensity of the surface state is much higher. Moreover, a clear spectral feature appears only for majority spin, whereas for minority spin the intensity may be only slightly increased in a broad energy range.

Furthermore, at $\theta = 45°$ the surface state can be hardly identified in the spectra of the 35° counter. In this case, the intensity of the surface state is lowest. It is higher for $\theta = 45°$ in the 70° counter and highest for $\theta = -45°$ in the 35° counter. This is consistent with the intensities of the Ni(001) surface state measured at similar geometrical arrangements (Starke et al. 1992*a*). From the different intensities, the direction of the dipole axes of the emitted radiation can be estimated. An investigation of the angular distribution of the Cu(001) surface state found the dipole axes at about −45° with respect to the surface normal towards the direction of the incident electrons (Fauster et al. 1989). By this, at $\theta = 45°$ the dipole axis would be in the same direction as the incoming electron beam. Consequently, the intensity would be the same in the 35° and in the −35° counter. This is not the fact for the measurements on 5 ML Co on Cu(001). Since the intensity of the Co surface state is much higher in the −35° counter than in the 35° counter, the angle of the dipole axis should be higher than −45°. Since there is at least low intensity in the 35° counter, the angle of the dipole axis should be lower than 0°. In figure 6.11, the angle of the dipole axis is −20° with respect to the surface normal. In this case, the intensity ratio of the −35° counter and the 70° counter approximately agrees with the experimentally observed intensities. The discrepancy in the direction of the dipole axis with Fauster et al. (1989) may have its origin in the kind of determination. The angular distribution of the spectral intensity measured for Cu(001) results in a broad maximum making the exact determination of the angle of maximum intensity

difficult. Moreover, in this work there is also a difference of about 20° between the measured and the calculated dipole axis of bulk states.

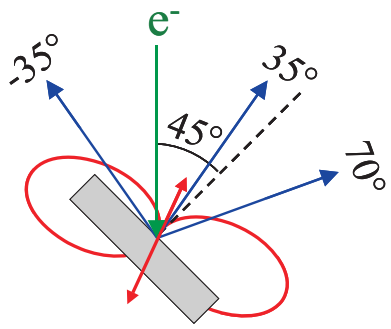

Figure 6.11: Geometrical arrangement of the IPE set-up at an angle of electron incidence $\theta = 45°$ and dipole radiation (red).

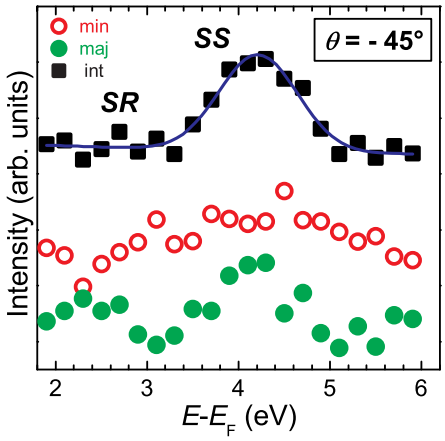

Figure 6.12: Inverse photoemission spectra of 5 ML Co / Cu(001) at $\theta = -45°$, showing the Co crystal-induced surface resonance *SR* and the surface state *SS*.

The intensity of the surface state is much higher if some Cu is put on top of the Co surface. Figure 6.13 shows IPE spectra of 0.5 ML Cu / 5 ML Co / Cu(001) at $\theta = 45°$. A spin-averaged linear background has been subtracted from the spectra, and the spectra are normalized to the background intensity. For 0.5 ML Cu coverage, the surface state appears at an energy of 4.3 eV (spin-integrated) as for 5 ML Co / Cu(001) at $\theta = -45°$. In contrast to the pure Co surfaces, the surface state of 0.5 ML Cu / 5 ML Co / Cu(001) clearly appears for both minority and majority spin. As for Ni and Fe, the spectral width of the minority feature is much larger, which means that its lifetime is shorter. The exchange splitting of the surface state amounts to 0.20 eV. However, it may be decreased by the Cu coverage. The fact

that Cu coverage results in an intensity increase of the surface state indicates that the lower intensity of the pure Co surface state is not due to a bad quality of the surface.

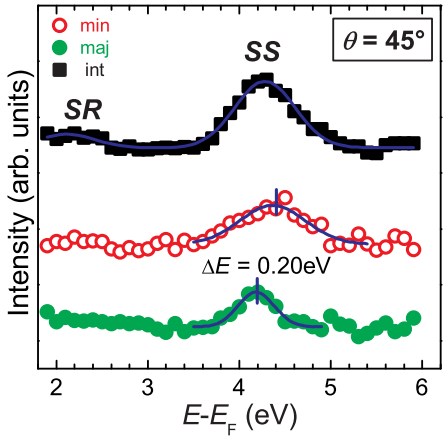

Figure 6.13: Inverse photoemission spectra of 0.5 ML Cu / 5 ML Co / Cu(001) at $\theta = 45°$, showing the Co crystal-induced surface resonance *SR* and the surface state *SS*.

To show the development of the surface states with further increasing Cu coverage, the IPE spectra of n ML Cu on 5 ML Co / Cu(001), $0 \leq n \leq 30$, are presented in figure 6.14 at an electron incidence angle of $\theta = 40°$ with the spin-averaged spectra on the left-hand side of the figure and the spin-resolved spectra on the right-hand side. The spectra are normalized to equal spin-averaged background intensity at an energy of about 1.5 eV. The peak positions of the individual features are accentuated by the colored marks: The Co-d bulk feature by black marks, the surface resonance *SR* by cyan marks, the surface state *SS* by magenta marks, and the Cu bulk feature *B* by blue marks.

In the lower part of figure 6.14 the spectrum of 5 ML Co / Cu(001) is presented showing the Co-d bulk transition, the surface resonance, and the surface state. With increasing Cu coverage, the Co-d transition gets attenuated by the Cu layer. As for Cu on Ni (see 6.1.1), the attenuation length amounts to about 10 ML. The surface state continuously shifts to lower energy. The strongest energy shift occurs between 1.5 and 4 ML Cu coverage. From 2 ML Cu its intensity is much higher. The surface resonance shifts to higher energy, too. Its intensity is strongly increased from 4 ML Cu. Above 3 ML Cu, another feature appears in the spectra (*B*). This is a bulk-like Cu state (Graß et al. 1993).

In figure 6.15 spin-resolved IPE spectra of only the surface state of n ML Cu / 5 ML Co / Cu(001) at $\theta = 45°$ are presented with better statistics. The spectra are normalized to equal spin-averaged background intensity. With increasing Cu coverage, the surface state continuously shifts to lower energy and its intensity increases. It appears for both minority and majority spin with about equal intensity. The spin

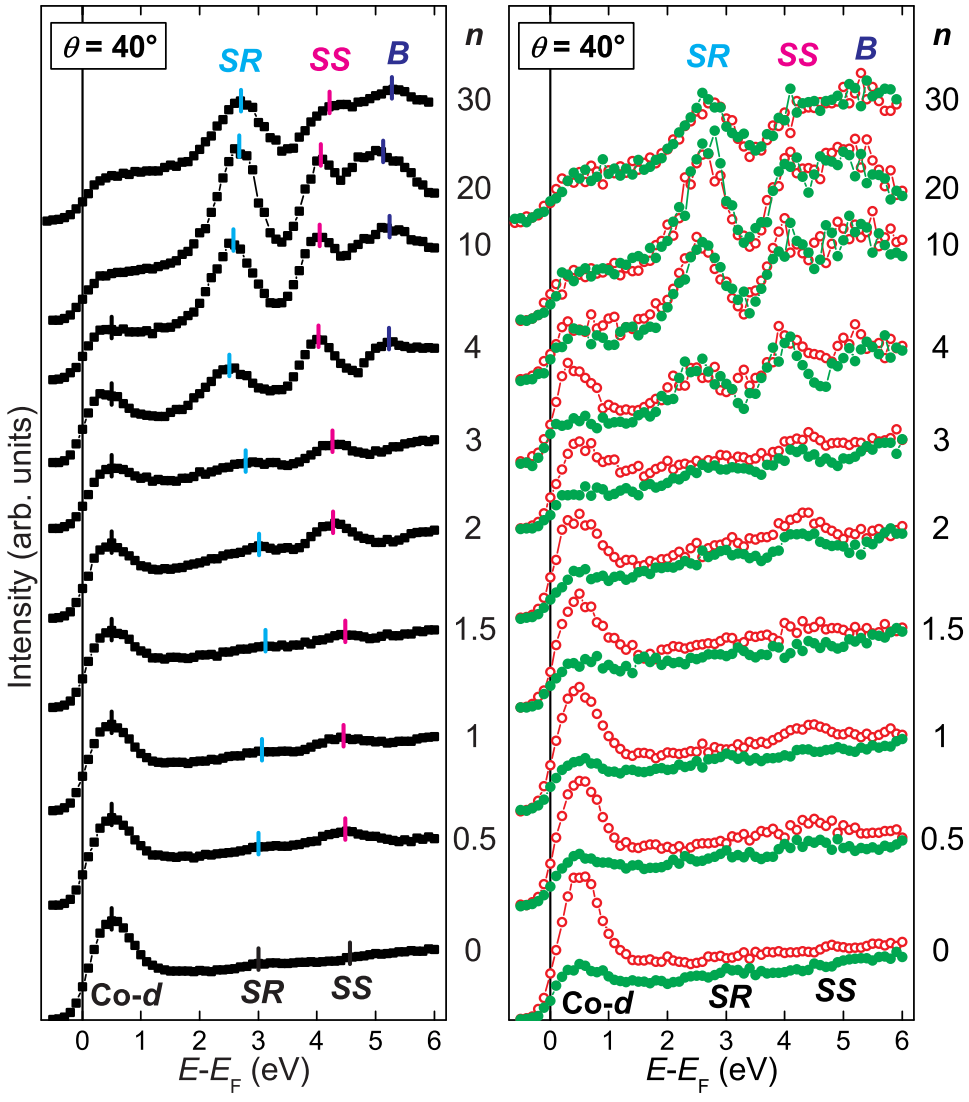

Figure 6.14: Spin-averaged (left-hand-side) and spin-resolved (right-hand-side) inverse photoemission spectra of n ML Cu / 5 ML Co / Cu(001) at $\theta = 40°$, showing the thickness dependence of the Co-d bulk feature, the surface resonance SR, the surface state SS, and the Cu bulk feature B. The spectra are normalized to equal spin-averaged background intensity.

asymmetry slightly decreases with increasing Cu coverage owing to the attenuation by the Cu overlayer. For 7 ML Cu, the surface state has not yet reached the energy of the surface state at Cu(001).

Compared to the calculated photoemission spectral densities, the Co(001) crystal-induced surface state appears at little lower energies. Its exchange splitting of 0.20 eV is lower than predicted by the calculation. Hence, the exchange splitting could not be determined for pure Co(001) but for 0.5 ML Co / Cu(001). The Cu overlayer may reduce the exchange splitting of the Co surface state. Furthermore,

the value is between the one for Ni and the one for Fe. This is expected from their magnetic moments, which is smallest for Ni and highest for Fe.

To sum up, the *sp*-derived crystal-induced surface state in the $L_{2'} - L_1$ energy gap near the $\bar{X}$ symmetry point has been experimentally identified the first time for Co(001). Compared to the corresponding surface states of Cu, Ni, and Fe, the spectral intensity is much lower for the Co surface state. The lower intensity does not have its origin in the sample preparation or a bad surface quality. Moreover, the intensity increase of the surface state due to Cu coverage indicates a good Co surface quality. For 0.5 ML Cu / 5 ML Co / Cu(001), the exchange splitting of the surface state amounts to 0.20 eV.

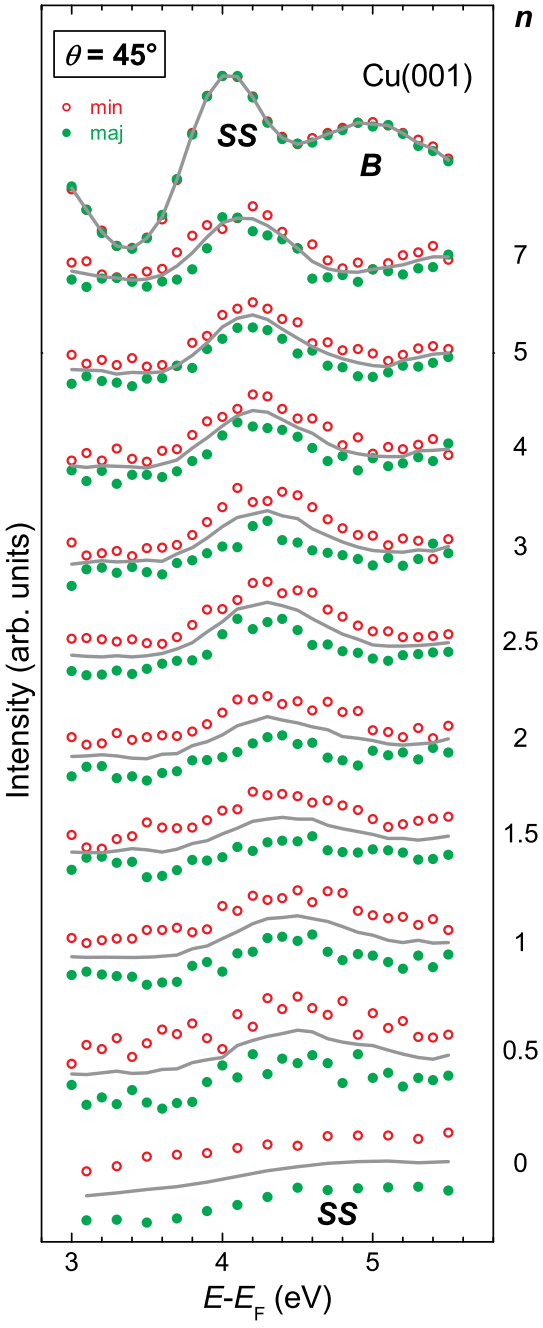

Figure 6.15: Spin-averaged (grey lines) and spin-resolved (red and green data points) inverse photoemission spectra of n ML Cu / 5 ML Co / Cu(001) at $\theta = 45°$, showing the dependence of the surface state *SS* on the Cu overlayer thickness. The spectra are normalized to equal spin-averaged background intensity.

Chapter 7

Summary

In the present study, electron confinement in two-dimensional magnetic systems has been investigated by measuring discrete unoccupied quantum-well states. By means of spin- and angle-resolved inverse photoemission, the electronic structure above the Fermi level has been probed. As samples, Ni films on Cu(001) and Cu films on Ni / Cu(001) as well as on Co / Cu(001) have been chosen.

For Ni / Cu(001), the different spectral features have been introduced and the spectra have been compared with the corresponding ones of Co / Cu(001). In particular, discrete spin-polarized quantum-well states in the films show up owing to electron confinement as expected from the bulk band structures. The spectra of Ni / Cu(001) show the influence of the two spin-reorientation transitions. At normal electron incidence, there is an spin asymmetry for in-plane magnetized films only. A 6 monolayer thick Ni film shows maximum spin asymmetry, and the exchange splitting has been determined. It amounts to 0.06 eV for the first quantum-well state at higher energy and to 0.02 eV for the second one at lower energy. These values are in accordance with the Ni bulk band structure.

For an in-plane film magnetization, the Ni-d feature of thin Ni films, resulting from transitions into Ni d bands, shows up for both minority and majority electron spin with a surplus for minority spin. This is in contradiction to expectations from the Ni bulk band structure, which shows an exclusive minority character of the d holes. This minority character is confirmed by inverse photoemission spectra of bulk Ni(001) (Starke et al. 1992*a*) and of thick in-plane magnetized Ni films. It has been shown that the reason for the reduced asymmetry of the Ni-d feature in thin films compared to bulk Ni is not in structural or magnetic film properties, e.g. a reduced magnetization due to the Curie temperature or to mixed magnetic domains, or spectral intensity by the Cu substrate or by quantum-well states. Hybridization between the Ni d bands and electronic states of the Cu substrate can be excluded, because this affects the interface layers only. Hence, the reduced spin asymmetry of the Ni-d feature must have its origin in a modified band structure such that the majority d bands are not entirely below the Fermi level. Owing to the existence of majority d holes, thin Ni films on Cu(001) do not represent a strong ferromagnet. Ultimately, a calculation of the spin-resolved band structure of thin Ni films on Cu(001) and of spin-resolved inverse photoemission spectra by J. Braun is in progress.

Furthermore, the dependence of the spectral features on the Ni film thickness has

been investigated. With increasing film thickness, the quantum-well features typically shift up in energy and converge towards the top of the Ni *sp* band. This thickness dependence has been confirmed by the phase accumulation model. The spin-resolved spectra only show a weak spin dependence. Up to 4 ML Ni coverage, there is no spin asymmetry owing to the phase transition from ferromagnetism to paramagnetism. The asymmetry is largest for 6 ML Ni. It decreases for thicker films due to the spin-reorientation transition. This behavior has been confirmed by spin-polarized secondary electron emission. The appearance of discrete quantum-well states indicates a two-dimensional behavior. The perpendicular electron momentum is not yet a good quantum number and the Ni-*sp* band is quantized. Above 15 ML Ni coverage, the bulk *sp* band begins to form, and the corresponding spectral feature shifts down in energy with increasing Ni coverage. The Ni quantum-well states converge towards the top of the Ni *sp* band, but the bulk Ni-*sp* transition appears at lower energy. This results in a shift to lower energy with increasing Ni coverage when the three-dimensional bulk band structure is formed. The formation of the three-dimensional continuous bulk *sp* band is not completed below 80 ML Ni coverage.

For 6 monolayers thick Ni films, the energy dispersion of the spectral features along the [110] direction has been determined. The Ni-*d* state shows no dispersion like the *d* state of bulk Ni(001). The image-potential induced surface state, the crystal-induced surface state, and the surface resonance have the same dispersion behavior for the Ni film as for bulk Ni(001). The three quantum-well states exhibit similar dispersion behavior as the bulk *sp* transition, but with different energy shifts relative to the bulk *sp* transition. Upon approaching the band-gap boundary, the quantum-well states evolve into a surface resonance state.

Furthermore, the electronic structure of thin Cu films on Ni / Cu(001) as well as on Co / Cu(001) has been investigated. With Cu on top of Ni / Cu(001) the thickness of the spin-reorientation transition decreases, thus only the spin-integrated inverse photoemission spectra of Cu / Ni / Cu(001) have been discussed.

For Cu / 6 ML Ni / Cu(001), the dependence of the spectral features on the Cu film thickness has been investigated. With increasing Cu coverage, the Ni quantum-well features do not change in energy, because the thickness of the Ni film stays constant, and the changing boundary conditions are negligible. Moreover, a Cu quantum-well resonance is identified. Up to 2 ML Cu coverage, it shows the expected behavior and shifts up in energy with increasing film thickness. However, the Cu spectral feature shifts down in energy with further increasing Cu coverage. It becomes superimposed with the Ni quantum-well features and strongly increases in intensity. Hence, the behavior of the Cu feature, concerning decrease in energy as well as increase in intensity, reflects the transition of discrete quantum-well resonances to the continuous Cu-*sp* bulk band. More than 20 ML Cu are required to complete the formation of the Cu-*sp* bulk band structure. The transition from discrete quantum-well states to bulk transitions also shows up for higher parallel electron momenta.

The energy dispersion along the [110] direction for 2 ML Cu / 6 ML Ni / Cu(001) shows that with increasing momentum the Ni-*d* feature remains at same energy. The image-potential induced surface state and the crystal-induced surface state show the same dispersion behavior for the Cu film as for bulk Cu(001). The Ni

quantum-well states exhibit exactly the same dispersion as in 6 ML Ni / Cu(001). Upon approaching the Ni band-gap boundary, they evolve into a surface resonance state. In addition, the Cu quantum-well resonance follows the *sp* band dispersion as well and converges towards the Cu band-gap boundary.

The dependence of the quantum-well states on the Cu film thickness has also been measured for Cu on 5 ML Co / Cu(001) at an electron incidence angle of $\theta = 25°$. With increasing Cu coverage, the Cu quantum-well resonance shifts up in energy for low Cu coverage, but down in energy for a Cu coverage above 7 ML. The transition of discrete quantum-well resonances to the continuous Cu-*sp* bulk band begins. The spin splitting is reduced to zero at about 6 ML Cu coverage, the spin asymmetry vanishes above 8 ML Cu coverage. In particular, the Cu quantum-well feature is strongly spin-dependent. Above 4 ML Cu coverage, the spin-dependence of the Cu quantum-well feature is almost lost reflecting the decoupling of the electron wave function in the Cu overlayer from the underlying ferromagnetic Co layer at the Cu-Co interface. It is no longer the spin-dependent reflection at the Cu-Co interface which results in discrete two-dimensional spin-polarized quantum-well states. Instead, the formation of the continuous three-dimensional spin-independent Cu *sp* band begins.

Finally, the *sp*-derived crystal-induced surface state has been experimentally identified the first time for Co(001). Compared to the corresponding surface states of Cu, Ni, and Fe, the spectral intensity is much lower for the Co surface state. The lower intensity does not have its origin in the sample preparation or a bad surface quality. The direction of the dipole axes of the emitted radiation has been estimated to about $-20°$ with respect to the surface normal towards the direction of the incident electrons from measurements at different geometrical arrangements. The intensity of the surface state strongly increases on Cu coverage. The surface state clearly appears for both minority and majority spin. The exchange splitting of the surface state amounts to 0.20 eV for 0.5 ML Cu / 5 ML Co / Cu(001) at an angle of electron incidence of $\theta = 45°$. However, it may be decreased by the Cu coverage. With further increasing Cu coverage, the surface state continuously shifts to lower energy, and its intensity is strongly increased. It appears for both minority and majority spin with about equal intensity. The spin asymmetry slightly decreases with increasing Cu coverage owing to the attenuation by the Cu overlayer. For 7 ML Cu, the surface state has not yet reached the energy of the surface state at Cu(001).

Zusammenfassung

In der vorliegenden Arbeit wurde der Einschluss von Elektronen in zweidimensionalen magnetischen Systemen durch die Messung diskreter unbesetzter Quantentrogzustände untersucht. Mittels spin- und winkelaufgelöster Inverser Photoemission wurde die elektronische Struktur oberhalb der Fermi-Energie bestimmt. Als Proben wurden Ni Filme auf Cu(001) und Cu Filme sowohl auf Ni / Cu(001) als auch auf Co / Cu(001) gewählt.

Bezüglich Ni / Cu(001) wurden die verschiedenen Strukturen in den Spektren vorgestellt, und die Spektren wurden mit den entsprechenden Spektren von Co / Cu(001) verglichen. Im Besonderen treten aufgrund von Elektroneneinschluss diskrete spinpolarisierte Quantentrogzustände in den Ni Filmen auf, wie dies aufgrund der Volumenbandstruktur zu erwarten ist. Die Spektren von Ni / Cu(001) zeigen den Einfluss der beiden Spinreorientierungsübergänge. Unter senkrechtem Elektroneneinfall liegt nur eine Spinasymmetrie für Filme vor, welche in der Ebene magnetisiert sind. Ein 6 Monolagen dicker Ni Film weist maximale Spinasymmetrie auf. Für diesen beträgt die Austauschaufspaltung 0.06 eV für den ersten Quantentrogzustand bei höherer Energie und 0.02 eV für den zweiten Quantentrogzustand bei niedrigerer Energie. Diese Werte sind mit der Volumenbandstruktur von Ni in Übereinstimmung.

Bei einer Magnetisierung in der Filmebene erscheint der Ni-d-Übergang, welcher aus Übergängen in die d-Bänder von Ni entsteht, bei dünnen Ni-Filmen sowohl für Minoritätselektronenspin als auch für Majoritätselektronenspin mit einem Mehrbetrag beim Minoritätselektronenspin. Dies steht im Widerspruch zu den Erwartungen aus der Ni-Volumenbandstruktur, welche einen exklusiven Minoritätscharakter der d-Löcher aufweist. Dieser Minoritätscharakter wird durch Inverse Photoemissionsspektren von volumenartigem Ni(001) (Starke et al. 1992a) und von dicken Ni-Filmen, welche in der Filmebene magnetisiert sind, bestätigt. Wie gezeigt liegt der Grund für die reduzierte Spin-Asymmetrie des Ni-d-Übergangs in dünnen Filmen im Vergleich zu volumenartigem Ni nicht in strukturellen oder magnetischen Filmeigenschaften, wie z.B. in einer reduzierten Magnetisierung aufgrund der Curie-Temperatur oder verschiedener magnetischer Domänen, oder in Intensitätsbeiträgen vom Cu-Substrat oder von Quantentrogzuständen. Eine Hybridisierung des Ni-d-Bandes mit elektronischen Zuständen des Cu-Substrates kann ausgeschlossen werden, da dies nur die Lagen an der Grenzfläche beeinflusst. Daher liegt der Ursprung der reduzierten Asymmetrie des Ni-d-Übergangs in einer derart modifizierten Bandstruktur, in welcher die Majoritäts-d-Bänder nicht vollständig unterhalb der Fermi-Energie liegen. Aufgrund der Existenz dieser Majoritäts-d-Löcher stellen dünne Ni Filme auf Cu(001) keinen starken Ferromagneten dar.Eine Berechnung der spinaufgelösten Bandstruktur dünner Ni-Filme auf Cu(001) und spinaufgelöster Inverser

Photoemissionsspektren von J. Braun in Vorbereitung.

Weiterhin wurde die Abhängigkeit der Strukturen in den Spektren von der Dicke der Ni-Filme untersucht. Mit zunehmender Filmdicke verschieben sich die Quantentrogzustände typischerweise zu höheren Energien und konvergieren gegen die Bandkante des Ni-*sp*-Bandes. Die Abhängigkeit von der Filmdicke wurde durch das Phasenakkumulationsmodell bekräftigt. Die spinaufgelösten Spektren zeigen nur eine schwache Spinabhängigkeit. Unterhalb von 4 ML Ni-Bedeckung liegt aufgrund des Phasenübergangs vom Ferromagnetismus zum Paramagnetismus keine Spinasymmetrie vor. Die Asymmetrie ist für 6 ML Ni am größten. Für dickere Filme geht sie aufgrund des Spinreorientierungsübergangs zurück. Dieses Verhalten wurde durch spinpolarisierte Sekundärelektronenemissionsmessungen bestätigt. Das Auftreten diskreter Quantentrogzustände weist auf ein zweidimensionales Verhalten hin. Der senkrechte Elektronenimpuls stellt noch keine gute Quantenzahl dar, und das Ni-*sp*-band ist quantisiert. Oberhalb von 15 ML Ni-Bedeckung beginnt die Bildung des volumenartigen *sp*-Bandes, und die entsprechenden Strukturen in den Spektren verschieben sich mit zunehmender Ni-Bedeckung zu niedrigeren Energien. Während die Ni-Quantentrogzustände gegen die Bandkante des Ni-*sp*-Bandes konvergieren, erscheint der volumenartige Ni-*sp*-Übergang bei niedrigerer Energie, was mit zunehmender Ni-Bedeckung zu einer Verschiebung zu niedrigeren Energien führt, wenn die dreidimensionale volumenartige Bandstruktur gebildet wird. Die Bildung des dreidimensionalen kontinuierlichen volumenartigen *sp*-Bandes ist nicht unterhalb einer Ni-Bedeckung von 80 ML Ni abgeschlossen.

Für einen 6 Monolagen dicken Ni film wurde die Energiedispersion der Strukturen in den Spektren entlang der [110]-Richtung bestimmt. Der Ni-*d*-Übergang zeigt keine Dispersion so wie der *d*-Übergang von volumenartigem Ni(001). Der Bildladungszustand, der kristallinduzierte Oberflächenzustand und die Oberflächenresonanz weisen das gleiche Dispersionsverhalten für die Ni-Filme auf wie für volumenartiges Ni(001). Die drei Quantentrogzustände zeigen ähnliches Dispersionsverhalten wie der volumenartige *sp*-Übergang, sind aber relativ zum volumenartigen *sp*-Übergang unterschiedlich in der Energie verschoben. Beim Annähern an die Grenze der Bandlücke entwickeln sich die Quantentrogzustände in eine Oberflächenresonanz.

Des Weiteren wurde die elektronische Struktur dünner Cu-Filme sowohl auf Ni / Cu(001) als auch auf Co / Cu(001) untersucht. Durch die Bedeckung von Ni / Cu(001) mit Cu nimmt die Schichtdicke, bei der der Spinreorientierungsübergang stattfindet, ab, weshalb nur die spinintegrierten Inversen Photoemissionsspektren von Cu / Ni / Cu(001) diskutiert wurden.

Für Cu / 6 ML Ni / Cu(001) wurde die Abhängigkeit der Strukturen in den Spektren von der Dicke des Cu-Films untersucht. Mit zunehmender Cu-Bedeckung ändert sich die Energie der Ni-Quantentrogzustände nicht, da die Dicke des Ni-Films unverändert bleibt und die veränderten Bedingungen an den Grenzflächen vernachlässigbar sind. Weiterhin wurde eine Cu-Quantentrogresonanz identifiziert. Bis zu einer Cu-Bedeckung von 2 ML zeigt diese das erwartete Verhalten und verschiebt sich mit zunehmender Filmdicke zu höheren Energien. Jedoch verschiebt sich die Cu-Struktur mit weiterhin zunehmender Cu-Bedeckung zu niedrigeren Energien. Sie wird mit den Ni-Quantentrogzuständen überlagert und nimmt stark an Intensität zu. Das Verhalten der Cu-Struktur bezüglich der Energieverringerung und der

Intensitätszunahme reflektiert daher den Übergang von diskreten Quantentrogresonanzen zum kontinuierlichen volumenartigen Cu-*sp*-Band. Letztendlich sind mehr als 20 ML Cu erforderlich um die Bildung der volumenartigen Cu-*sp*-Bandstruktur abzuschließen. Der Übergang von diskreten Quantentrogzuständen zu volumenartigen Übergängen zeigt sich auch bei höheren parallelen Elektronenimpulsen.

Die Energiedispersion entlang der [110]-Richtung von 2 ML Cu / 6 ML Ni / Cu(001) zeigt, dass der Ni-*d*-Übergang mit zunehmendem Impuls bei gleicher Energie bleibt. Der Bildladungszustand und der kristallinduzierte Oberflächenzustand weisen für den Cu-Film das gleiche Dispersionsverhalten auf wie für volumenartiges Cu(001). Die Ni-Quantentrogzustände zeigen genau die gleiche Dispersion wie in 6 ML Ni / Cu(001). Beim Annähern an die Grenze der Ni-Bandlücke entwickeln sie sich zu Oberflächenresonanzen. Zudem folgt die Cu-Quantentrogresonanz der Dispersion des *sp*-Bandes und konvergiert gegen die Grenze der Cu-Bandlücke.

Die Abhängigkeit der Quantentrogzustände von der Dicke des Cu-Films wurde auch für Cu auf 5 ML Co / Cu(001) unter einem Elektroneneinfallswinkel von $\theta = 25°$ gemessen. Mit zunehmender Cu-Bedeckung verschiebt sich die Cu-Quantentrogresonanz bei niedriger Cu-Bedeckung zu höheren Energien, aber ab einer Cu-Bedeckung von 7 ML zu niedrigeren Energien. Der Übergang von diskreten Quantentrogresonanzen zum kontinuierlichen volumenartigen Cu-*sp*-Band beginnt. Eine Austauschaufspaltung existiert ab etwa 6 ML Cu-Bedeckung nicht mehr, eine Spinasymmetrie ab etwa 8 ML Cu-Bedeckung. Im Besonderen ist die Cu-Quantentrogresonanz stark spinabhängig. Oberhalb von einer Cu-Bedeckung von 4 ML ist die Spinabhängigkeit der Cu-Quantentrogresonanz nahezu verschwunden, was die Entkopplung der Elektronenwellenfunktion im oberen Cu-Film von der darunter liegenden ferromagnetischen Co-Schicht an der Cu-Co-Grenzfläche zeigt. Es liegt keine spinabhängige Reflektion an der Cu-Co-Grenzfläche mehr vor, welche zu diskreten zweidimensionalen spinpolarisierten Quantentrogzuständen führt. Vielmehr beginnt die Bildung des kontinuierlichen dreidimensionalen Cu-*sp*-Bandes.

Schließlich ist zum ersten mal der experimentelle Nachweis des *sp*-abgeleiteten kristallinduzierten Oberflächenzustands von Co(001) gelungen. Im Vergleich zu den entsprechenden Oberflächenzuständen von Cu, Ni und Fe ist die spektrale Intensität des Co-Oberflächenzustandes viel geringer. Die geringere Intensität hängt nicht mit der Probenpräparation oder einer schlechten Oberflächenqualität zusammen. Die Richtung der Dipolachse der emittierten Strahlung wurde aufgrund von Messungen bei unterschiedlichen geometrischen Anordnungen zu etwa $-20°$ relativ zur Oberflächennormale entgegen der Elektroneneinfallsrichtung abgeschätzt. Die Intensität des Oberflächenzustands nimmt bei zunehmender Cu-Bedeckung stark zu. Der Oberflächenzustand erscheint deutlich sowohl für Minoritäts- als auch für Majoritätsspin. Die Austauschaufspaltung des Oberflächenzustands beträgt 0.20 eV für 0.5 ML Cu / 5 ML Co / Cu(001) unter einem Elektroneneinfallswinkel von $\theta = 45°$. Sie kann durch die Cu-Bedeckung jedoch verringert sein. Mit weiter zunehmender Cu-Bedeckung verschiebt sich der Oberflächenzustand kontinuierlich zu kleineren Energien und seine Intensität nimmt stark zu. Er erscheint sowohl für Minoritäts- als auch für Majoritätsspin mit etwa gleicher Intensität. Die Spinasymmetrie nimmt aufgrund der Abschwächung durch die obere Cu-Schicht mit zunehmender Cu-Bedeckung leicht ab. Für 7 ML hat der Oberflächenzustand die Energie des

Oberflächenzustands von Cu(001) fast erreicht.

Bibliography

Aharoni, A. (1986), *J. Appl. Phys.* **61**, 3302.

Allenspach, R. and Bischof, A. (1992), *Phys. Rev. Lett.* **69**, 3385.

Ashcroft, N. W. and Mermin, N. D. (1976), *Solid state physics*, Holt, Rinehart, and Winston, New York.

Auger, P. (1925), *Le Journal des Physique et le Radium* **6**, 205.

Baberschke, K. (1996), *Appl. Phys. A* **62**, 417.

Baberschke, K. (2001), Anisotropy in magnetism, *in* K. Baberschke, M. Donath and W. Nolting, eds, 'Band-ferromagnetism: Ground-state and finite-temperature phenomena', Vol. 580 of *Lecture Notes in Physics*, Springer, Berlin/Heidelberg/New York, p. 27.

Bachmann, A. (2003), private communication.

Bahr, C. C., Barton, J. J., Hussain, Z., Robey, S. W., Tobin, J. G. and Shirley, D. A. (1987), *Phys. Rev. B* **35**, 3773.

Baibich, M. N., Broto, J. M., Fert, A., Nguyen Van Dau, F., Petroff, F., Etienne, P., Creuzet, G., Friederich, A. and Chazelas, J. (1988), *Phys. Rev. Lett.* **61**, 2472.

Bander, M. and Mills, D. L. (1988), *Phys. Rev. B* **38**, 12015.

Bastard, G. (1988), *Wave mechanics applied to semiconductor heterostructures*, Les editions de physique, Les Ulis, France, chapter III.

Bauer, E. (1958), *Z. Kristallogr.* **110**, 372.

Bennett, W. R., Schwarzacher, W. and Egelhoff Jr., W. F. (1990), *Phys. Rev. Lett.* **65**, 3169.

Berglund, C. N. and Spicer, W. E. (1964), *Phys. Rev. A* **136**, 1030+1044.

Bernhard, T., Pfandzelter, R., Gruyters, M. and Winter, H. (2005), *Surf. Sci.* **575**, 154.

Binash, G., Grünberg, P., Saurenbach, F. and Zinn, W. (1989), *Phys. Rev. B* **39**, 4828.

Binder, K. and Landau, D. P. (1984), *Phys. Rev. Lett.* **52**, 318.

Binnig, G., Rohrer, H., Gerber, C. and Weibel, E. (1982), *Appl. Phys. Lett.* **40**, 178.

Binnig, G., Rohrer, H., Gerber, C. and Weibel, E. (1983), *Phys. Rev. Lett.* **50**, 120.

Bland, J. A. C. and Heinrich, B., eds (1994), *Ultrathin magnetic structures*, Vol. 1, Springer, Berlin, Heidelberg.

Blundell, S. (2001), *Magnetism in condensed matter*, Oxford University Press, New York.

Bode, M. (2003), *Rep. Prog. Phys.* **66**, 523.

Borstel, G. and Thörner, G. (1988), *Surf. Sci. Rep.* **8**, 1.

Bovensiepen, U., Poulopoulos, P., Platow, W., Farle, M. and Baberschke, K. (1999), *J. Magn. Magn. Matter* **192**, L386.

Bramwell, S. T. and Holdsworth, P. C. W. (1993), *J. Phys.: Condens. Matter* **5**, L53.

Braun, J. (2005), private communication.

Braun, J. and Donath, M. (2004), *J. Phys.: Condens. Matter* **16**, S2539.

Braun, J., Math, C., Postnikov, A. and Donath, M. (2002), *Phys. Rev. B* **65**, 184412.

Brown Jr., W. F. (1963), *Micromagnetics*, Interscience, New York.

Brubaker, M. E., Mattson, J. E., Sowers, C. H. and Bader, S. D. (1991), *Appl. Phys. Lett.* **58**, 2306.

Brune, H. (2001), Growth modes, *in* K. Samwer, ed., 'Physical properties of thin films and artificial multilayers', Encyclopedia of materials: Science and technology, Pergamon Press, chapter 1.9, pp. 3683–3693.

Bruno, P. (1993*a*), *Europhys. Lett.* **23**, 615.

Bruno, P. (1993*b*), *J. Magn. Magn. Matter* **121**, 248.

Bruno, P. (1995), *Phys. Rev. B* **52**, 411.

Bruno, P. (1999), *J. Phys.: Condens. Matter* **11**, 9403.

Burton, W. K., Cabrera, N. and Frank, F. C. (1951), *Trans. Roy. Soc. A* **243**, 299.

Carbone, C., Vescovo, E., Rader, O., Gudat, W. and Eberhardt, W. (1993), *Phys. Rev. Lett.* **71**, 2805.

Cerdá, J. R., de Andres, P. L., Cebollada, A., Miranda, R., Navas, E., Schuster, P., Schneider, C. M. and Kirschner, J. (1993), *J. Phys.: Condens. Matter* **5**, 2055.

Chen, Y., Tong, S. T., Kim, J. S., Mohamed, M. H. and Kesmodel, L. L. (1991), *Phys. Rev. B* **43**, 6788.

Chiang, T.-C. (2000), *Surf. Sci. Rep.* **39**, 181.

Chiang, T.-C. (2005), *Chinese Journal of Physics* **43**, 154.

Cho, A. Y. (1971), *Appl. Phys. Lett.* **19**, 467.

Chrobok, G. and Hofman, M. (1976), *Phys. Lett.* **57A**, 257.

Clarke, A., Jennings, G., Willis, R. F., Rous, P. J. and Pendry, J. B. (1987), *Surf. Sci.* **187**, 327.

Clemens, W. (1997), *J. Appl. Phys.* **81**, 4310.

Clemens, W., Kachel, T., Rader, O., Vescovo, E., Blügel, S., Carbone, C. and Eberhardt, W. (1992), *Solid State Commun.* **81**(739).

Cohen, M. S., Huber Jr., E. E., Weiss, G. P. and Smith, D. O. (1960), *J. Appl. Phys.* **31**, 291.

Crampin, S. (1993), *J. Phys.: Condens. Matter* **5**, 4647.

Curti, F. G., Danese, A. and Bartynski, R. A. (1998), *Phys. Rev. Lett.* **80**, 2213.

Daalderop, G. H. O., Kelly, P. J. and Schuurmans, M. F. H. (1994), *Phys. Rev. B* **50**, 9989.

Danese, A., Arena, D. A. and Bartynski, R. A. (2001), *Prog. Surf. Sci.* **67**, 249.

Danese, A. and Bartynski, R. A. (2002), *Phys. Rev. B* **65**, 174419.

Danese, A. G., Curti, F. G. and Bartynski, R. A. (2004*b*), *Phys. Rev. B* **70**, 165420.

Danese, A. G., Yao, H., Arena, D. A., Hochstrasser, M., Tobin, J. G. and Bartynski, R. A. (2004*a*), *Phys. Sat. Sol. (b)* **241**, 2358.

Davis, L. E., McDonald, N. C., Palmberg, P. W., Riach, G. E. and Weber, R. E. (1976), *Handbook of Auger electron spectroscopy*, Physical Electronics Industries, Eden Prairie, MN.

de Vries, J. J., Schudelaro, A. A. P., Jungblut, R., Bloemen, B. J. H., Reinders, A., Kohlhepp, J., Coehoorn, R. and de Jonge, W. J. M. (1995), *Phys. Rev. Lett.* **75**, 4306.

de Vries, J. J., van de Vorst, M. T. H., Johnson, M. T., Jungblut, R., Reinders, A., Bloemen, P. J. H., Coehoorn, R. and de Jonge, W. J. M. (1996), *Phys. Rev. B* **54**, R748.

Denninger, G., Dose, V. and Scheidt, H. (1979), *Appl. Phys.* **18**, 375.

Dhesi, S. S., Dürr, H. A., van der Laan, G., Dudzik, E. and Brookes, N. B. (1999), *Phys. Rev. B* **60**, 12852.

Dhesi, S. S., Dudzik, E., Dürr, H. A., Brookes, N. B. and van der Laan, G. (2000), *Surf. Sci.* **454-456**, 930.

Dibeler, V. H., Walker, J. A., Culloh, K. E. M. and Rosenstock, H. M. (1971), *Int. J. Mass Spectrom. Ion Phys.* **7**, 209–.

Domb, C. (1973), *J. Phys. A* **6**, 1296.

Donath, M. (1994), *Surf. Sci. Rep.* **20**, 251.

Donath, M., Dose, V., Ertl, K. and Kolac, U. (1990), *Phys. Rev. B* **41**, 5509.

Dose, V. (1977), *Appl. Phys.* **14**, 117.

Dose, V. (1983), *Prog. Surf. Sci.* **13**, 225.

Dose, V. (1985), *Surf. Sci. Rep.* **5**, 337.

Dose, V., Fauster, T. and Schneider, R. (1986), *Appl. Phys. A* **40**, 203.

Dose, V. and Reusing, G. (1980), *Appl. Phys.* **23**, 131.

Dunning, F. B., Gray, L. G., Ratliff, J. M., Tang, F.-C., Zhang, X. and Walters, G. K. (1987), *Rev. Sci. Instrum.* **58**, 1706.

Echenique, P. M. and Pendry, J. B. (1978), *J. Phys. C* **11**, 2065.

Echenique, P. M. and Pendry, J. B. (1989), *Prog. Surf. Sci.* **32**, 111.

Eckardt, H. and Fritsche, L. (1987), *J. Phys. F* **17**, 925.

Egger, S., Back, C. H., Krewer, J. and Pescia, D. (1999), *Phys. Rev. Lett.* **83**, 2833.

Ehrlich, G. and Hudda, F. (1966), *J. Chem. Phys.* **44**, 1039.

Einstein, A. (1905), *Ann. Phys.* **17**, 132.

Erickson, R. P. and Mills, D. L. (1991), *Phys. Rev. B* **43**, 11527.

Ernst, A., Lueders, M., Temmermann, W. M., Szotek, Z. and van der Laan, G. (2000*b*), *J. Phys.: Condens. Matter* **12**, 5599.

Ernst, A., van der Laan, G., Temmermann, W. M., Dhesi, S. S. and Szotek, Z. (2000*a*), *Phys. Rev. B* **62**, 9543.

Ertl, G. and Küppers, J. (1985), *Low energy electrons and surface chemistry*, VCH, Weinheim.

Farle, M., Mirwald-Schulz, B., Anisimov, A. N., Platow, W. and Baberschke, K. (1997*a*), *Phys. Rev. B* **55**, 3708.

Farle, M., Platow, W., Anisimov, A. N., Poulopoulos, P. and Baberschke, K. (1997*b*), *Phys. Rev. B* **56**, 5100.

Farle, M., Platow, W., Anisimov, A. N., Schulz, B. and Baberschke, K. (1997*c*), *J. Magn. Magn. Matter* **165**, 74.

Fassbender, J., Allenspach, R. and Dürig, U. (1997), *Surf. Sci.* **383**, L742.

Fassbender, J., May, U., Schirmer, B., Jungblut, R. M. and abd G. Güntherodt, B. H. (1995), *Phys. Rev. Lett.* **75**, 4476.

Fauster, T. and Himpsel, F. J. (1983), *J. Vac. Sci. Technol.* **A 1**, 1111.

Fauster, T., Himpsel, F. J., Donelon, J. J. and Marx, A. (1983), *Rev. Sci. Instrum.* **54**, 68.

Fauster, T., Schneider, R. and Dürr, H. (1989), *Phys. Rev. B* **40**, 7981.

Ferrenberg, A. M. and Landau, D. P. (1991), *Phys. Rev. B* **44**, 5081.

Frank, F. C. and van der Merwe, J. H. (1949), *Proc. R. Soc. London Ser. A* **198**, 216.

Fukumoto, K., Daimon, H., Chelaru, L., Offi, F., Kuch, W. and Kirschner, J. (2002), *Surf. Sci.* **514**, 151.

Fuss, A., Demokritov, S., Grünberg, P. and Zinn, W. (1992), *J. Magn. Magn. Matter* **103**, L221.

Garrett, R. F. and Smith, N. V. (1986), *Phys. Rev. B* **33**, 3740.

Garrison, K., Chang, Y. and Johnson, P. D. (1993), *Phys. Rev. Lett.* **71**, 2801.

Giesen, K., Hage, F., Himpsel, F. J., Riess, H. J. and Steinmann, W. (1985), *Phys. Rev. Lett.* **55**, 300.

Glatzel, H., Schneider, R., Fauster, T. and Dose, V. (1992), *Z. Phys. B - Condensed Matter* **88**, 53.

Goldmann, A. (1982), *Vakuum-Technik* **31**, 204.

Goldmann, A., Donath, M., Altmann, W. and Dose, V. (1985), *Phys. Rev. B* **32**, 837.

Graß, M., Braun, J., Borstel, G., Schneider, R., Dürr, H., Fauster, T. and Dose, V. (1993), *J. Phys.: Condens. Matter* **5**, 599.

Gray, L. G., Hart, M. W., Dunning, F. B. and Walters, G. K. (1983), *Rev. Sci. Instrum.* **55**, 88.

Grünberg, P., Schreiber, R., Pang, Y., Brodsky, M. B. and Sowers, H. (1986), *Phys. Rev. Lett.* **57**, 2442.

Gruyters, M., Bernhard, T. and Winter, H. (2005), *Phys. Rev. Lett.* **94**, 227205.

Gubanka, B., Donath, M. and Passek, F. (1996*a*), *Phys. Rev. B* **54**, R11153.

Gubanka, B., Donath, M. and Passek, F. (1996*b*), *J. Magn. Magn. Matter* **5161**, L11.

Guo, Y., Zhang, Y.-F., Bao, X.-Y., Han, T.-Z., Tang, Z., Zhang, L.-X., Zhu, W.-G., Wang, E. G., Niu, Q., Qiu, Z. Q., Jia, J.-F., Zhao, Z.-X. and Xue, Q.-K. (2004), *Science* **306**, 1915.

Gurney, B. A., Tsang, M. C. C., Williams, M., Parkin, S. S. P., Fontana Jr., R. E., Grochowski, E., Pinarbasi, M., Lin, T. and Mauri, D. (2005), Spin valve giant magnetoresistive sensor materials for hard disk drives, *in* B. Heinrich and J. A. C. Bland, eds, 'Ultrathin magnetic structures IV', Springer, Berlin, Heidelberg, chapter 6.

Haight, R. (1995), *Surf. Sci. Rep.* **21**, 275.

Hamers, R. J. (1992), *in* H.-J. Güntherodt and R. Wiesendanger, eds, 'Scanning tunneling microscopy', Springer, Berlin.

Hamers, R. J., Tromp, R. M. and Demuth, J. E. (1986), *Phys. Rev. Lett.* **56**, 1972.

Hansen, M. (1958), *Constitution of binary alloys*, McGraw-Hill, New York.

Harris, M. J. (1999), *American Mineralogist* **84**, 1632.

Heath, D. F. and Sacher, P. A. (1966), *Appl. Optics* **5**, 937.

Heckmann, O., Magnan, H., le Fevre, P., Chandesris, D. and Rehr, J. J. (1994), *Surf. Sci.* **312**, 62.

Heinrich, B. and Cochran, J. F. (1993), *Adv. Phys.* **42**, 523.

Heisenberg, W. (1928), *Z. Phys.* **49**, 619.

Hertz, H. (1887), *Ann. Phys.* **31**, 983.

Hüfner, S. (1996), *Photoelectron spectroscopy*, Vol. 82 of *Springer Ser. Solid-State Sci.*, 2nd edn, Springer, Berlin/Heidelberg.

Himpsel, F. J. (1990), *Surf. Sci. Rep.* **12**, 1.

Himpsel, F. J., Ortega, J. E., Mankey, G. J. and Willis, R. F. (1998), *Adv. in Phys.* **47**, 511.

Himpsel, F. J. and Rader, O. (1995), *Appl. Phys. Lett.* **67**, 1151.

Hirsch, A. A., Ahilea, E. and Friedman, N. (1969), *Phys. Lett.* **28A**, 763.

Hjortstam, O., Trygg, J., Wills, J. M., Johansson, B. and Eriksson, O. (1996), *Phys. Rev. B* **53**, 9204.

Hormandinger, G. and Pendry, J. B. (1993), *Surf. Sci.* **295**, 34.

Huang, F., Kief, M. T., Mankey, G. J. and Willis, R. F. (1994), *Phys. Rev. B* **49**, 3962.

Huang, H., Zhu, X. and Hermanson, J. (1984), *Phys. Rev. B* **29**, 6186.

Hubbard, J. (1963), *Proc. Roy. Soc. A* **276**, 238.

Hubbard, J. (1964*a*), *Proc. Roy. Soc. A* **277**, 237.

Hubbard, J. (1964*b*), *Proc. Roy. Soc. A* **281**, 401.

Hwang, C. and Himpsel, F. J. (1995), *Phys. Rev. B* **52**, 15368.

Jalocholwski, M. and Bauer, E. (1988), *Phys. Rev. B* **38**, 5272.

Jalochowski, M. (1995), *Prog. Surf. Sci.* **48**, 287.

Jiang, C.-S., Li, S.-C., Yu, H.-B., Eom, D., Wang, X.-D., Ebert, P., Jia, J.-F., Xue, Q.-K. and Shih, C.-K. (2004), *Phys. Rev. Lett.* **92**, 106104.

Johnson, K. E., Mirzamaani, M. and Doerner, M. F. (1995), *IEEE* **31**, 2721.

Johnson, M. T., Purcell, S. T., McGee, N. W. E., Coehorn, R., ann de Stegge, J. and Hoving, W. (1992), *Phys. Rev. Lett.* **68**, 2688.

Johnson, P. D. (1997), *Rep. Prog. Phys.* **60**, 1217.

Jones, B. A. and Hanna, C. B. (1993), *Phys. Rev. Lett.* **71**, 4253.

Joyce, B. A. (1985), *Rep. Prog. Phys.* **48**, 1637.

Jung, R., Koh, H., Lee, J. Y., You, D. G., Choi, W. and Kim, C. (2003), *J. Appl. Phys.* **94**, 4649.

Kane, E. O. (1964), *Phys. Rev. Lett.* **12**, 97.

Karis, O., Magnuson, M., Wiell, T., Weinelt, M., Wassdahl, N., Nilsson, A., Mårtensson, N., Holmström, E., Niklasson, A. M. N. and Eriksson, O. (2000), *Phys. Rev. B* **62**, R16239.

Karis, O., Magnuson, M., Wiell, T., Weinelt, M., Wassdahl, N., Nilsson, A., Mårtensson, N., Holmström, E., Niklasson, A. M. N., Eriksson, O. and Johansson, B. (2001), *Phys. Rev. B* **63**, 113401.

Kawakami, R. K., Rotenberg, E., Escorcia-Aparicio, J. E., Choi, H. J., Cummins, T. R., Tobin, J. G., Smith, N. V. and Qiu, Z. Q. (1998), *Phys. Rev. Lett.* **80**, 1754.

Kessler, J. (1985), *Polarized Electrons*, 2 edn, Springer, Berlin.

Kevan, S. D. and Eberhardt, W. (1992), *in* S. D. Kevan, ed., 'Angle-resolved photoemission, Theory and current applications', Vol. 74 of *Studies in surface science*, Elsevier, Amsterdam, p. 99.

Kevan, S. D., ed. (1992), *Angle-resolved photoemission, Theory and current applications*, Vol. 74 of *Studies in surface science*, Elsevier, Amsterdam.

Kirschner, J. and Feder, R. (1979), *Phys. Rev. Lett.* **42**, 1008.

Kläsges, R., Schmitz, D., Carbone, C., Eberhardt, W., Lang, P., Zeller, R. and Dedrichs, P. H. (1998), *Phys. Rev. B* **57**, R696.

Kolac, U., Donath, M., Ertl, K., Liebl, H. and Dose, V. (1988), *Rev. Sci. Instrum.* **59**, 1933.

Kosterlitz, J. M. and Thouless, D. J. (1978), Vol. VII B of *Progress in low-temperature physics*, North-Holland, North Holland, Amsterdam.

Kubby, J. A. and Greene, W. J. (1992), *Phys. Rev. Lett.* **68**, 329.

Kuch, W., Gilles, J., Kang, S. S., Imada, S., Suga, S. and Kirschner, J. (2000), *Phys. Rev. B* **62**, 3824.

Landolt, M. (1986), *Appl. Phys. A* **41**, 83.

Lang, J. K. and Baer, Y. (1979), *Rev. Sci. Instrum.* **50**, 221.

Lenard, P. (1900), *Ann. Phys.* **2**, 359.

Li, D., Pearson, J., Bader, S. D., Vescovo, E., Huang, D.-J., Johnson, P. D. and Heinrich, B. (1997), *Phys. Rev. Lett.* **78**, 1154.

Li, D., Pearson, J., Mattson, J., Bader, S. and Johnson, P. D. (1995), *Phys. Rev. B* **51**, 7195.

Li, D.-Q., Freitag, M., Pearson, J., Qiu, Z. Q. and Bader, S. D. (1994), *Phys. Rev. Lett.* **72**, 3112.

Li, H. and Tonner, B. P. (1990), *Surf. Sci.* **237**, 141.

Lindau, I. and Spicer, W. E. (1974), *J. Electr. Spectrosc. Relat. Phenom.* **3**, 409.

Lindner, J., Poulopoulos, P., Wilhelm, F., Farle, M. and Baberschke, K. (2000), *Phys. Rev. B* **62**, 10431.

Luh, D.-A., Miller, T., Paggel, J. J., Chou, M. Y. and Chiang, T.-C. (2001), *Science* **292**, 1131.

Luh, D.-A., Paggel, J. J., Miller, T. and Chiang, T.-C. (2000), *Phys. Rev. Lett.* **84**, 3410.

Ma, S.-K. (1976), *Modern theory of critical phenomena*, Benjamin, New York.

Ma, S. K. (1985), *Statistical mechanics*, World Scientific, Singapore, chapter 29, pp. 495–498.

Mankey, G. J., Subramanian, K., Stockbauer, R. L. and Kurtz, R. L. (1997), *Phys. Rev. Lett.* **78**, 1146.

Mankey, G. J., Willis, R. F. and Himpsel, F. J. (1993), *Phys. Rev. B* **48**, 10284.

Math, C. (2001), PhD thesis, Universität Bayreuth.

Mathon, J., Villeret, M., Muniz, R. B., d'Albuquerque e Castro, J. and Edwards, D. M. (1995), *Phys. Rev. Lett.* **74**, 3696.

Mathon, J., Villeret, M., Umerski, A., Muniz, R. B., d'Albuquerque e Castro, J. and Edwards, D. M. (1997), *Phys. Rev. B* **56**, 11797.

McRae, E. G. and Kane, M. L. (1981), *Surf. Sci.* **108**, 435.

Mermin, N. D. and Wagner, H. (1966), *Phys. Rev. Lett.* **17**, 1133.

Miguel, J. J. D., Cellbollada, A., Gallego, J. M., Ferrer, S., Mirando, R., Schneider, C. M., Bressler, P., Garbe, J., Bethke, K. and Kirschner, J. (1989), *Surf. Sci.* **211/212**, 732.

Miguel, J. J. D., Cellbollada, A., Gallego, J. M., Mirando, R., Schneider, C. M., Schuster, P. and Kirschner, J. (1991), *J. Magn. Magn. Matter* **93**, 1.

Miller, T., Samsavar, A., Franklin, G. E. and Chiang, T.-C. (1988), *Phys. Rev. Lett.* **61**, 1404.

Milun, M., Pervan, P. and Woodruff, D. P. (2002), *Rep. Prog. Phys.* **65**, 99.

Müller, S., Bayer, P., Reichel, C., Heinz, K., Feldmann, B., Zillgen, Z. and Wuttig, M. (1995), *Phys. Rev. Lett.* **74**, 765.

Müller, S., Schulz, B., Kostka, G., Farle, M., Heinz, K. and Baberschke, K. (1996), *Surf. Sci.* **364**, 235.

M.Tromp, R., Denier van der Gon, A. W., LeGoues, F. K. and Reuter, M. C. (1993), *Phys. Rev. Lett.* **71**, 3299.

Mugarza, A. (2002), PhD thesis, Universidad del País Vasco.

Mugarza, A., Ortega, J. E., Mascaraque, A., Michel, E. G., Altmann, K. N. and Himpsel, F. J. (2000), *Phys. Rev. B* **62**, 12672.

Neél, L. (1954), *J. Phys. Rad.* **15**, 225.

Nishizawa, T. and Ishida, K. (1983), *Bulk Alloy Phase Diagrams* **4**, 387.

Nünthel, R., Gleitsmann, T., Poulopoulos, P., Scherz, A., Lindner, J., Kosubek, E., Litwinski, C., Li, Z., Wende, H., Baberschke, K., Stolbov, S. and Rahman, T. (2003), *Surf. Sci.* **531**, 53.

Noakes, T. C. Q., Bailey, P. and van der Laan, G. (2003), *Phys. Rev. B* **67**, 153401.

Nolting, W. (1986), *Quantentheorie des Magnetismus (Quantum theory of magnetism)*, Vol. 2 of *Teubner Studienbücher*, Teubner, Stuttgart.

Nordström, L., Lang, P., Zeller, R. and Dederichs, P. H. (1995), *Europhys. Lett.* **29**, 395.

Nouvertné, F., May, U., Bamming, M., Rampe, A., Korte, U., Güntherodt, G., Pentcheva, R. and Scheffler, M. (1999*b*), *Phys. Rev. B* **60**, 14382.

O'Brien, W. L., Droubay, T. and Tonner, B. P. (1996), *Phys. Rev. B* **54**, 9297.

O'Brien, W. L. and Tonner, B. P. (1994), *Phys. Rev. B* **49**, 15370.

Okuno, S. N. (1995), *Phys. Rev. B* **51**, 6139.

Okuno, S. N. and Inomata, K. (1994), *Phys. Rev. Lett.* **72**, 1553.

Onsager, L. (1944), *Phys. Rev.* **65**, 117.

Ortega, J. E. and Himpsel, F. J. (1992), *Phys. Rev. Lett.* **69**, 844.

Ortega, J. E., Närmann, A., Altmann, K. N., O'Brien, W., Seo, D. J., Himpsel, F. J., Segovia, P., Mascaraque, A. and Michel, E. G. (1999), *J. Magn. Magn. Matter* **203**, 126.

Ortega, J., Himpsel, F. J., Mankey, G. J. and Willis, R. F. (1993), *Phys. Rev. B* **47**, 1540.

Osterwalder, J. (2006), Spin-polarized photoemission, *in* E. Beaurepaire, H. Bulou, F. Scheurer and J.-P. Kappler, eds, 'Magnetism: A synchrotron radiation approach', Vol. 697 of *Lecture Notes in Physics*, Springer, Berlin/Heidelberg, pp. 95–120.

Paggel, J. J., Luh, D.-A., Miller, T. and Chiang, T.-C. (2004), *Phys. Rev. Lett.* **92**, 186803.

Paggel, J. J., Wei, C. M., Chou, M. Y., Luh, D.-A., Miller, T. and Chiang, T.-C. (2002), *Phys. Rev. B* **66**, 233403.

Pampuch, C., Rader, O., Kläsges, R. and Carbone, C. (2001), *Phys. Rev. B* **63**, 153409.

Pappas, D. P. (1996), *J. Vac. Sci. Technol. B* **14**, 3203.

Parkin, S. S. P. (1993), *Phys. Rev. Lett.* **71**, 1641.

Parkin, S. S. P., Bhadra, R. and Roche, K. P. (1991), *Phys. Rev. Lett.* **66**, 2152.

Parkin, S. S. P., More, N. and Roche, K. P. (1990), *Phys. Rev. Lett.* **64**, 2304.

Pendry, J. B. (1976), *Surf. Sci.* **57**, 679.

Pendry, J. B. (1980), *Phys. Rev. Lett.* **45**, 1356.

Pendry, J. B. and Gurman, S. B. (1975), *Surf. Sci.* **49**, 87.

Pentcheva, R. and Scheffler, M. (2002), *Phys. Rev. B* **65**, 155418.

Pescia, D., Kerrkmann, D., Schumann, F. and Gudat, W. (1990), *Z. Phys. B* **78**, 475.

Pfandzelter, R., Igel, T. and Winter, H. (1996), *Phys. Rev. B* **54**, 4496.

Pierce, D. T. and Meier, F. (1976), *Phys. Rev. B* **13**, 5484.

Pizzini, S., Fontaine, A., Giorgetti, C., Dartyge, E., Bobo, J. F., Piecuch, M. and Baudelet, F. (1995), *Phys. Rev. Lett.* **74**, 1470.

Platow, W., Bovensiepen, U., Poulopoulos, P., Farle, M., Baberschke, K., Hammer, L., Walter, S., Müller, S. and Heinz, K. (1999), *Phys. Rev. B* **59**, 12641.

Plummer, E. W. and Eberhardt, W. (1982), *Adv. Chem. Phys.* **49**, 533.

Poulopoulos, P., Lindner, J., Farle, M. and Baberschke, K. (1999), *Surf. Sci.* **437**, 277.

Pourovskii, L. V., Skorodumova, N. V., Vekilov, Y. K., Johansson, B. and Abrikosov, I. A. (1999), *Surf. Sci.* **439**, 111.

Powell, C. J. (1988), *J. Electron Spectrosc. Rel. Phen.* **47**, 197.

Purcell, S. T., Folkerts, W., Johnson, M. T., McGee, N. W. E., Jager, K., ann de Stegge, J., Zeper, W. B., Hoving, W. and Grünberg, P. (1991), *Phys. Rev. Lett.* **67**, 903.

Purcell, S. T., Johnson, M. T., McGee, N. W. E., Coehoorn, R. and Hoving, W. (1992), *Phys. Rev. B* **45**, 13064.

Qiao, S., Kimura, A., Harasawa, A., Sawada, M., Chung, J. G. and Kakizaki, A. (1997), *Rev. Sci. Instrum.* **68**, 4390.

Qiu, Z. Q., Pearson, J. and Bader, S. D. (1992*b*), *Phys. Rev. B* **46**, 8659.

Qiu, Z. Q., Pearson, J., Berger, A. and Bader, S. D. (1992*a*), *Phys. Rev. Lett.* **68**, 1398.

Qiu, Z. Q. and Smith, N. V. (2002), *J. Phys.: Condens. Matter* **14**, R169.

Rader, O., Vescovo, E., Redinger, J., Blügel, S., Carbone, C., Eberhardt, W. and Gudat, W. (1994), *Phys. Rev. Lett.* **72**, 2247.

Ramsperger, U., Vaterlaus, A., Pfäffli, P., Maier, U. and Pescia, D. (1996), *Phys. Rev. B* **53**, 8001.

Renken, V., Yu, D. H. and Donath, M. (2007), *Surf. Sci.* . in press.

Röntgen, W. C. (1895), *Eine neue Art von Strahlen (On a new kind of rays)*, Verlag und Druck der Stahel'schen K. Hof- und Kunsthandlung, Würzburg.

Rossi, S. D., Tagliaferri, A. and Ciccacci, F. (1996), *J. Magn. Magn. Matter* **157-158**, 287.

Rotenberg, E., Wu, Y. Z., An, J. M., Hove, M. A. V., Canning, A., Wang, L. W. and Qiu, Z. Q. (2006), *Phys. Rev. B* **73**, 075426.

Salis, G., Kato, Y., Ensslin, K., Driscoll, D. C., Gossard, A. C. and Awschalom, D. D. (2001), *Nature (London)* **414**, 619.

Samant, M. G., Stöhr, J., Parkin, S. S. P., Held, G. A., Hermsmeier, B. D. and Herman, F. (1994), *Phys. Rev. Lett.* **72**, 1112.

Samson, J. A. R. (1967), *Techniques of vacuum ultraviolet spectroscopy*, John Wiley and Sons.

Schmid, A. K., Atlan, D., Itoh, H., Heinrich, B., Ichinokawa, T. and Kirschner, J. (1993), *Phys. Rev. B* **48**, 2855.

Schmid, A. K. and Kirschner, J. (1992), *Ultramicroscopy* **42-44**, 483.

Schmidt, A. B., Wiemhöfer, M., Pickel, M., Donath, M. and Weinelt, M. (2005), *Phys. Rev. Lett.* **95**, 107402.

Schmidt, A. and Schneider, T. (1992), *Z. Phys. B* **87**, 265.

Schneider, C. M., Bressler, P., Schuster, P., Kirschner, J., de Miguel, J. J. and Miranda, R. (1990), *Phys. Rev. Lett.* **64**, 10592.

Schneider, C. M., Schuster, P., Hammond, M., Ebert, H., Noffke, J. and Kirschner, J. (1991), *J. Phys.: Condens. Matter* **3**, 4349.

Schneider, R. (1985), Diplomarbeit. Universität Würzburg.

Schneider, R., Starke, K., Ertl, K., Donath, M., Dose, V., Graß, J. B. M. and Borstel, G. (1992), *J. Phys.: Condens. Matter* **4**, 4293.

Schulz, B. and Baberschke, K. (1994), *Phys. Rev. B* **50**, 13467.

Schwoebel, R. L. (1969), *J. Appl. Phys.* **40**, 614.

Segovia, P., Michel, E. G. and Ortega, J. E. (1996), *Phys. Rev. Lett.* **77**, 3455.

Shen, J., Giergiel, J. and Kirschner, J. (1995), *Phys. Rev. B* **52**, 8454.

Shen, J. and Kirschner, J. (2002), *Surf. Sci.* **500**, 300.

Shen, J., Lin, M.-T., Giergiel, J., Schmidthals, C., Schneider, M. Z. C. M. and Kirschner, J. (1996), *J. Magn. Magn. Matter* **156**, 104.

Shi, J. (2005), Magnetic switching in high-density MRAM, *in* B. Heinrich and J. A. C. Bland, eds, 'Ultrathin magnetic structures IV', Springer, Berlin, Heidelberg, chapter 7.

Shikin, A. M., Rader, O., Prudnikova, G. V., Adamchuk, V. K. and Gudat, W. (2002), *Phys. Rev. B* **65**, 075403.

Shockley, W. (1939), *Phys. Rev.* **56**, 317.

Siegmann, H. C. (1994), *SS* **307-309**, 1076.

Smith, N. V. (1985), *Phys. Rev. B* **32**, 3549.

Smith, N. V. (1988), *Rep. Prog. Phys.* **51**, 1227.

Smith, N. V., Brookes, N. B., Chiang, Y. and Johnson, P. D. (1994), *Phys. Rev. B* **49**, 332.

Speckmann, M., Oepen, H. P. and Ibach, H. (1995), *Phys. Rev. Lett.* **75**, 2035.

Spišák, D. and Hafner, J. (2000), *J. Phys.: Condens. Matter* **12**, L139.

Srivastava, P., Haak, N., Wende, H., Chauvistré, R. and Baberschke, K. (1997), *Phys. Rev. B* **56**, R4398.

Srivastava, P., Wilhelm, F., Ney, A., Farlew, M., Wende, H., Haak, N., Ceballos, G. and Baberschke, K. (1998), *Phys. Rev. B* **58**, 5701.

Stamm, C., Würsch, C., Egger, S. and Pescia, D. (1998), *J. Magn. Magn. Matter* **177-181**, 1279.

Starke, K., Ertl, K. and Dose, V. (1992*a*), *Phys. Rev. B* **46**, 9709.

Starke, K., Ertl, K. and Dose, V. (1992*b*), *Phys. Rev. B* **45**, 6154.

Stiles, M. D. (1993), *Phys. Rev. B* **48**, 7238.

Stoner, E. C. (1936), *Proc. Roy. Soc. A* **154**, 656.

Stoner, E. C. (1939), *Proc. Roy. Soc. A* **169**, 339.

Stranski, I. N. and Krastanov, L. (1938), 'Zur Theorie der orientierten Ausscheidung von Ionenkristallen aufeinander', Sitzungsbericht Akademie der Wissenschaften Wien, Math.-naturwiss. Kl. IIb 146.

Su, W. B., Chang, S. H., Jian, W. B., Chang, C. S., Chen, L. J. and Tsong, T. T. (2001), *Phys. Rev. Lett.* **86**, 5116.

Takahashi, M. (1962), *J. Appl. Phys.* **33**, 1101.

Tamm, I. (1932), *Phys. Z. Soviet Union* **1**, 733.

Tersoff, J. and Falicov, L. M. (1982), *Phys. Rev. B* **26**, 6186.

Tischer, M., Arvanitis, D., Yokoyama, T., Lederer, T., Tröger, L. and Baberschke, K. (1994), *Surf. Sci.* **307-309**, 1096.

Tischer, M., Hjortstam, O., Arvanitis, D., Hunter Dunn, J., May, F., Baberschke, K., Trygg, J., Wills, J. M., Johansson, B. and Eriksson, O. (1995), *Phys. Rev. Lett.* **75**, 1602.

Ulmer, K. (1959), *Phys. Rev. Lett.* **3**, 514.

Unguris, J., Celotta, R. J. and Pierce, D. T. (1991), *Phys. Rev. Lett.* **67**, 140.

Unguris, J., Celotta, R. J. and Pierce, D. T. (n.d.), 1992 March Meeting (Indianapolis, IN).

van Dijken, S., Vollmer, R., Poelsema, B. and Kirschner, J. (1999), *J. Magn. Magn. Matter* **210**, 316.

van Gelderen, P., Crampin, S. and Inglesfield, J. E. (1996), *Phys. Rev. B* **53**, 9115.

van Schilfgaarde, M. and Harrison, W. A. (1993), *Phys. Rev. Lett.* **71**, 3870.

Volmer, M. and Weber, A. (1926), *Z. Phys. Chem.* **119**, 277.

von der Linden, W., Dose, V., Memmel, N. and Fischer, R. (1998), *Surf. Sci.* **409**, 290.

Š. Pick and Dreyssé, H. (1992), *Phys. Rev. B* **46**, 5802.

Wang, D., Freeman, A. J. and Krakauer, H. (1982), *Phys. Rev. B* **26**, 1340.

Wang, D. S., Wu, R. and Freeman, A. J. (1994), *J. Magn. Magn. Matter* **129**, 237.

Wang, Y., Levy, P. M. and Fry, J. L. (1990), *Phys. Rev. Lett.* **65**, 2732.

Weaver, J. H. (1986), *Phys. Today* p. 24.

Weiss, P. and Foëx, G. (1926), *Le magnetisme*, Armand Colin, Paris.

Won, C., Wu, Y. Z., Kurahashi, N., Law, K. T., Zhao, H. W., Scholl, A., Doran, A. and Qiu, Z. Q. (2003), *Phys. Rev. B* **67**, 174425.

Würsch, G., Stamm, C., Egger, S., Pescia, D., Baltensperger, W. and Helman, J. S. (1997), *Nature* **389**, 937.

Wu, S. Z., Schumann, F. O., Mankey, G. J. and Willis, R. F. (1996), *J. Vac. Sci. Technol.* **14**, 3189.

Wu, Y. Z., Won, C., Rotenberg, E., Zhao, H. W., Xue, Q.-K., Kim, W., Owens, T. L., Smith, N. V. and Qiu, Z. Q. (2006), *Phys. Rev. B* **73**, 125333.

Yafet, Y., Kwo, J. and Gyorgy, E. M. (1986), *Phys. Rev. B* **33**, 6519.

Yang, Z. and Wu, R. (2001), *Phys. Rev. B* **63**, 064413.

Yato, Y., Myers, R. C., Gossard, A. C. and Awschalom, D. D. (2004), *Nature (London)* **427**, 50.

Yu, D. H. and Donath, M. (2003*a*), *Europhys. Lett.* **63**(5), 729.

Yu, D. H., Donath, M., Braun, J. and Rangelov, G. (2003*b*), *Phys. Rev. B* **68**, 155415.

Yu, D. H., Math, C., Maier, M., Escher, M., Rangelov, G. and Donath, M. (2007), *Surf. Sci.* . in press.

Zangwill, A. (1988), *Physics at surfaces*, Cambridge University Press, New York.

Zhang, Z., Niu, Q. and Shih, C.-K. (1998), *Phys. Rev. Lett.* **80**, 5381.

Zheng, M., Shen, J., Ohresser, P., Mohan, C. V., Klaua, M., Barthel, J. and Kirschner, J. (1999), *J. Appl. Phys.* **85**, 5060.

Zumbrägel, K. (2007), Diplomarbeit. Westfälische Wilhelms-Universität Münster.

Danksagung

An dieser Stelle möchte ich meine Dankbarkeit all denen gegenüber zum Ausdruck bringen, die mich während meines Aufenthalts in der Arbeitsgruppe *Oberflächenmagnetismus* unterstützt haben und zum Gelingen der vorliegenden Arbeit beigetragen haben.

Im Besonderen bedanken möchte ich mich bei

Prof. Dr. Markus Donath für die Aufnahme in seine Arbeitsgruppe, für die Ermöglichung sowie das fördernde Interesse am Fortgang der Untersuchungen sowie für die stete Diskussionsbereitschaft,

Dr. Dehong Yu für die Einführung in das Themengebiet *Quantentrogzustände* und das Vorstellen von PETRA und SABINE,

apl. Prof. Dr. Jürgen Braun für die Unterstützung durch die Theorie,

der Arbeitsgruppe *Oberflächenmagnetismus* mit allen Mitarbeitern auch vergangener Tage, insbesondere bei Tobias Allmers, Dr. Andreas Bachmann, Ilse Bekemeier, apl. Prof. Dr. Jürgen Braun, Michael Budke, Ing. grad. Jürgen Coellen, Dr. Juliet Slayton Correa, Prof. Dr. Markus Donath, Christian Eibl, Christian Eickhoff, Dr. Horst Fehmer, Julia Husham, Hristo Kolev, Max Theodor Kuchel, Peter Lendecke, Dipl.-Ing. Werner Mai, Frank Ostendorf, Martin Pickel, Johannes Pieper, Dr. Georgi Rangelov, Thomas Saerbeck, Dr. Akihiko Shigemoto, Hubert Wensing, Dr. Lothar Wiedmann, Martin Wiemhöfer, Kathrin Wulff, Dr. Dehong Yu und Karen Zumbrägel für die stete Hilfsbereitschaft und viele anregende Diskussionen nicht nur bei den Doktorandenseminaren,

Hubert Wensing sowie Werner David und der Feinmechanischen Werkstatt für die Unterstützung hinsichtlich jeglicher Art von technischen und mechanischen Angelegenheiten,

Dipl.-Ing. Werner Mai sowie Daniel Troche und der Elektronikwerkstatt für die Unterstützung hinsichtlich jeglicher Art von elektronischen Angelegenheiten.

Ein ganz besonders herzlicher Dank gilt meiner Familie, im Besonderen Valerie und Siv Marie, für die stetige Unterstützung und zahlreiche Ermutigungen während meiner Doktorandenzeit.